BRNO UNIVERSITY OF TECHNOLOGY

VYSOKÉ UČENÍ TECHNICKÉ V BRNĚ

FACULTY OF MECHANICAL ENGINEERING

FAKULTA STROJNÍHO INŽENÝRSTVÍ

INSTITUTE OF PHYSICAL ENGINEERING

ÚSTAV FYZIKÁLNÍHO INŽENÝRSTVÍ

FABRICATION, OPTIMIZATION AND IN-SITU CHARACTERIZATION OF THERMALLY TUNABLE VANADIUM DIOXIDE NANOSTRUCTURES

VÝROBA, OPTIMALIZACE A IN-SITU CHARAKTERIZACE TEPLOTNĚ LADITELNÝCH NANOSTRUKTUR OXIDU VANADIČITÉHO

MASTER'S THESIS

DIPLOMOVÁ PRÁCE

AUTHOR

AUTOR PRÁCE

Bc. Jan Krpenský

SUPERVISOR

VEDOUCÍ PRÁCE

Ing. Andrea Konečná, Ph.D.

BRNO 2021

BRNO UNIVERSITY OF TECHNOLOGY
FACULTY OF MECHANICAL ENGINEERING

Assignment Master's Thesis

Institut:	Institute of Physical Engineering
Student:	**Bc. Jan Krpenský**
Degree programm:	Physical Engineering and Nanotechnology
Branch:	no specialisation
Supervisor:	**Ing. Andrea Konečná, Ph.D.**
Academic year:	2021/22

As provided for by the Act No. 111/98 Coll. on higher education institutions and the BUT Study and Examination Regulations, the director of the Institute hereby assigns the following topic of Master's Thesis:

Fabrication, optimization and in–situ characterization of thermally tunable vanadium dioxide nanostructures

Brief Description:

Vanadium dioxide (VO2) is an example of a strongly correlated material that exhibits temperature–induced metal–insulator phase transition (MIT). Electrical and optical properties of VO2 start changing significantly due to MIT closely above 340 K, making this material a promising candidate for various applications in fast optical switching, energy storage or novel optical elements. Most of these applications rely on the emergence of two types of optical modes in VO2 nanostructures in distinct phases. However, spectral and spatial characteristics of the modes and their switching are closely related to the exact local character of the MIT and its dependence on sample inhomogeneities and impurities.

Although MIT's main mechanisms, dynamics and spatial dependence in bulk VO2 are relatively well understood, a direct link between local optical response and the MIT close to domain boundaries, atomic–scale defects or interfaces in VO2 nanostructures is yet to be explored and established. In this thesis, VO2 nanostructures will be fabricated and studied experimentally in a scanning transmission electron microscope. Spatial inhomogeneities of the nanostructures will be characterized by high–resolution imaging, electron diffraction, electron energy–loss spectroscopy and energy–dispersive X–ray spectroscopy with in–situ heating. The correlation of all these signals should provide novel insights into the influence of the quality of VO2 nanostructures on their optical and electrical properties.

Master's Thesis goals:

1) Review dependence of optical properties of vanadium dioxide on temperature. Study possible experimental methods for fabricating VO2 nanostructures (thin films, nanoparticles) and characterisation techniques.
2) Verify the methods for fabricating VO2 samples suitable for transmission electron microscopy. Try to optimise the quality of the fabricated samples in terms of resulting optical properties.
3) Try to prepare samples on specialised chips enabling in–situ control of sample temperature in an electron microscope.
4) Characterize fabricated samples with the help of an operator of a transmission electron microscope. Try to perform high–resolution imaging, electron diffraction, energy–dispersive X–ray spectroscopy and in particular, measure optical properties of the VO2 nanostructures by electron energy–loss spectroscopy.

Recommended bibliography:

LIGMAJER, F., et al. Epitaxial VO2 Nanostructures: A Route to Large-Scale, Switchable Dielectric Metasurfaces. ACS Photonics, 5 (2018), 2561-2567.

WAN, C., et al. On the Optical Properties of Thin-Film Vanadium Dioxide from the Visible to the Far Infrared. Ann. Phys., 531 (2019), 1900188.

KEPIČ, P., et al. Optically Tunable Mie Resonance VO2 Nanoantennas for Metasurfaces in the Visible. ACS Photonics, 8 (2021), 1048-1057.

Deadline for submission Master's Thesis is given by the Schedule of the Academic year 2021/22

In Brno,

L. S.

prof. RNDr. Tomáš Šikola, CSc.
Director of the Institute

doc. Ing. Jaroslav Katolický, Ph.D.
FME dean

Abstract
Vanadium dioxide (VO_2) has attracted increasing attention over the past decades due to its metal–insulator phase transition at temperature around 68 °C. This phase change is accompanied by lattice change from monoclinic (dielectric) to tetragonal (metal), lattice shrinking in the metallic state, and stark difference in the infrared transmittance between both phases. However, fabrication of VO_2 thin films can be challenging due to other possible stoichiometric configurations, such as VO, V_2O_3, or V_2O_5. Many fabrication techniques have been used in recent years, where optimized fabrication process produces V_xO_y in the desired stoichiometry of VO_2. In this Thesis, a summary of three deposition techniques suitable for the deposition of VO_2 thin films is made and the process of creating thin samples (lamellae) suitable for study in the transmission electron microscopy (TEM) via focused ion beam (FIB) is described. Utilizing TEM with in-situ heating for characterization of VO_2 samples produces valuable information on the microstructure of VO_2 both below and above the transition temperature. In addition, electron energy-loss spectroscopy gives precious insight into the changing of different stoichiometries of VO_2 in correlation to the thickness of the examined sample, near the sample edge in particular.

Keywords
Vanadium dioxide, FIB, lamella, TEM, EELS

Abstrakt
Oxid vanadičitý (VO_2) přilákal v posledních desetiletích zvýšenou pozornost kvůli svému fázovému přechodu kov–izolant na teplotě okolo 68 °C. Tento fázový přechod je provázen změnou krystalové mříže z monoklinické (dielektrikum) na tetragonální (kov), smrštěním krystalové mříže v kovové fázi a výrazným rozdílem mezi transmisivitou v infračervené oblasti mezi oběma fázemi. Avšak výroba VO_2 může být náročná kvůli jiným možným stochiometrickým konfiguracím jako je VO, V_2O_3 nebo V_2O_5. V posledních letech bylo použito mnoho výrobních technik, u kterých optimalizace výrobního procesu produkuje V_xO_y v požadované VO_2 stochiometrii. V této práci je uvedeno shrnutí tří technik vhodných pro depozici tenkých vrstev VO_2 a je popsán proces výroby tenkých vzorků (lamel), které jsou vhodné pro studium v transmisním elektronovém mikroskopu (TEM), pomocí fokusovaného iontového svazku (FIB). Použití TEM se zahříváním uvnitř komory pro charakterizaci VO_2 vzorků produkuje cenné informace o mikrostruktuře VO_2 pod i nad teplotou přechodu. Navíc dává spektroskopie energiových ztrát elektronů cenný vhled do změn různých stochiometrií VO_2 v souvislosti s tloušťkou zkoumaného vzorku, zejména blízko hrany vzorku.

Klíčová slova
Oxid vanadičitý, FIB, lamela, TEM, EELS

KRPENSKÝ, J.*Fabrication, optimization and in-situ characterization of thermally tunable vanadium dioxide nanostructures.* Brno, 2022. 69 p. Master's Thesis. Brno University of Technology, Faculty of Mechanical Engineering. Supervisor Ing. Andrea Konečná, Ph.D.

I declare that I have written my Master's Thesis on the theme of *Fabrication, optimization and in–situ characterization of thermally tunable vanadium dioxide nanostructures* independently, under the guidance of the supervisor Ing. Andrea Konečná, Ph.D., and using the sources quoted in the list of literature at the end of the Thesis.

Bc. Jan Krpenský

First and foremost, I am extremely grateful to my supervisor Ing. Andrea Konečná, Ph.D. for her mentoring and continuous support not only on the topics related to this Thesis.

My deep appreciation goes to Ing. Michal Horák, Ph.D. for his willingness and patience during the TEM measurements, his valuable advice on the TEM sample preparation, and fruitful discussions considering the obtained data.

I address my acknowledgement to Ing. Mgr. Peter Kepič for providing me a suitable sample for the fabrication of lamellae that were essential for this Thesis. I would also like to recognize the assistance of Ing. Katarína Rovenská considering some of the sample fabrication.

I gratefully acknowledge Ing. Mgr. Tomáš Šamořil, Ph.D. for his mentoring on the operation of FIB, which deepened my understanding of the technique and ultimately made this Thesis possible due to the experience I acquired throughout the years.

Final acknowledgement goes to my family for their immense encouragement and support throughout my whole life.

Bc. Jan Krpenský

Financial support from the ThermoFisher Scientific is gratefully acknowledged.

CzechNanoLab project LM2018110 funded by MEYS CR is gratefully acknowledged for the financial support of the measurements/sample fabrication at CEITEC Nano Research Infrastructure.

Contents

Introduction

Altering the properties of propagating light using nanostructures of subwavelength dimensions has become a key research in the emerging field of metasurfaces and metamaterials [1]. Metasurfaces have seen development in utilizing dielectrics instead of noble metals [2] and notably materials with tunable optical properties [3]. Depending on the desired application, these metamaterials can be abruptly switched or gradually tuned by applying external stimuli: electrical, optical, or thermal.

The latter class of materials is represented by vanadium dioxide (VO_2) and germanium antimony telluride (GST), which can both undergo a reversible phase transition between the insulating phase at low temperatures, and the conductive phase at high temperatures.

Among those two materials, VO_2 stands out because it exhibits fast metal–insulator transition (MIT) that is situated near room temperature ($\approx 68\,^{\circ}\mathrm{C}$), and because it can withstand millions of switching cycles without degradation [4]. However, the fabrication of VO_2 is quite challenging since the phase transition properties may vary from abrupt to gradual depending on VO_2 film quality, thickness, grain size, and strain [5, 6, 7].

To better understand the structure of VO_2 samples and the inner processes of the MIT, transmission electron microscopy (TEM) has been used. High-resolution imaging, diffraction, and energy-dispersive X-ray spectroscopy (EDXS) can be used for the study of VO_2 sample structure. Among others, electron energy-loss spectroscopy (EELS) proved to be invaluable technique for discerning the chemical composition of thin VO_2 samples.

Chapter 1 starts with the introduction of VO_2 as a tunable material, and the nature of its phase change is investigated at the atomic level. Several other VO_2 polymorphs are mentioned along with their characteristics. We then describe the optical and electrical properties that are inherently connected with the phase change of VO_2. Lastly, ellipsometric measurements of the main sample used within this Thesis are shown to demonstrate its required property of undergoing a phase change.

Chapter 2 is devoted to the fabrication of VO_2 samples. The first part deals with the description of deposition of VO_2 thin films, where three individual techniques are discussed in more detail: Pulsed laser deposition (PLD), electron beam evaporation, and ion beam sputtering deposition (IBSD). The second part of this Chapter is dedicated to the description of the focused ion beam (FIB) and its utilization for the fabrication of thin samples – lamellae – that are suitable for the characterization in a transmission electron microscope (TEM). The third part summarizes all the results from the fabrication of the three types of samples used within this Thesis – VO_2 powder on a holley C grid, VO_2 lamella on a TEM Cu grid, and VO_2 lamella on a TEM heating chip.

Chapter 3 is dedicated to transmission electron microscopy (TEM). After the introduction of basic working principles of the microscope and energy-dispersive X-ray spectroscopy (EDXS), we proceed with a description of the main part of the characterization of our samples – electron energy-loss spectroscopy (EELS). We describe its application for the measurements of VO_2 in the literature, mainly its core-loss part that contains information on the absorption edges characteristic for each element. The third part again summarizes all the results from the TEM characterization of the three types of samples used within this Thesis. After the investigation of our samples by EDXS and high-resolution imaging, the last section is devoted to EELS measurements, which is the culmination of this Thesis.

1 Vanadium dioxide

The discovery of vanadium dioxide (VO_2) in 1959 [8] commenced its extensive study by scientific community owing to its metal–insulator transition (MIT) that is accompanied by a change of its crystallographic structure. During the MIT, the material exhibits a change in electrical conductivity, optical absorption, and dielectric function. Moreover, the MIT occurs at a relatively low temperature ($T \approx 68\,°C$ [9]) that is conveniently accessible. In addition, the MIT can be driven not only thermally [10], but also electrically [11], optically [12], or via strain [13]. These properties made VO_2 a material of intense focus for both research-driven curiosity of materials scientists as well as application possibility interest of device engineers.

There is a great variety of compounds with different V_xO_y stoichiometry, such as VO, V_2O_3, V_2O_5, V_3O_5, V_4O_7, V_5O_9, etc [14]. Many of them exhibit sharp changes in optical, electrical, thermal, and magnetic properties. Due to this variety, fabrication of a compound with certain stoichiometry can prove challenging, which will be discussed in the next Chapter 2. Out of all the possible compounds, VO_2 stands out because of its low transition temperature.

VO_2 is a material with extensive potential applications thanks to its unique physical properties. In recent years, advancement in its fabrication and property modulation has smoothed the way for its application in many fields such as thermal sensing, thermochromics, electronics, and multiple response mechanics [15].

This Chapter will be dedicated to more in-depth description of the physics and origin of the VO_2 phase transition. Crystallographic structure in both phases as well as changing optical and electrical properties will be described.

1.1 Crystallographic structure

During the MIT, VO_2 undergoes a lattice change from insulating monoclinic (M_1) phase (at low temperature) to metallic rutile (R) phase (at high temperature), which can be seen in Figure 1.1 [16]. In the picture, the metallic (R) phase is gray and monoclinic (M1) phase is green.

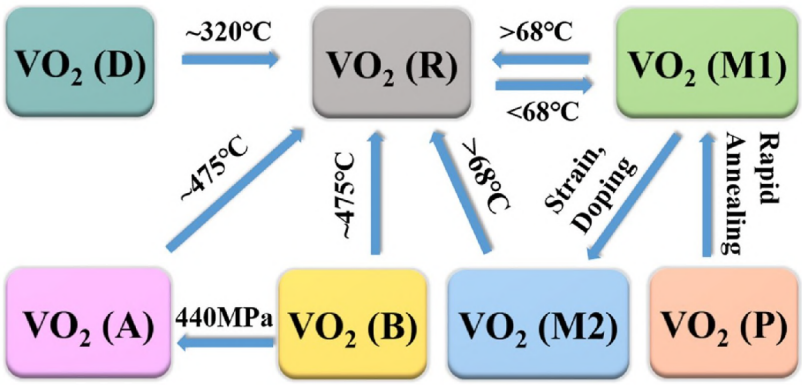

Figure 1.1: Diagram of phase transformations between different phases of VO_2. Adapted from [16].

However, at present there are several other phases of VO_2 that are also illustrated in Figure 1.1. These phases can transform into each other when certain conditions are met, which is illustrated by arrows connecting the phases. Among these phases, VO_2 (M1), VO_2 (M2), VO_2 (R), VO_2 (A), and VO_2 (B) have the most common crystal structure – the structural unit is the VO6 octahedron (vanadium atom in the center with six oxygen atoms surrounding it).

Most of the current reasearch and applications are based on the MIT of VO_2 (M) – both VO_2 (M1) and (M2) [17]. VO_2 (R) is the high-temperature rutile phase of VO_2 [18]. In the Thesis, these two phases will be investigated, since they are the most commonly used phases due to their reversible near-room temperature. Furthermore, VO_2 (A) is another phase with MIT behaviour at $T \approx 162\,°C$ [19]. VO_2 (B) has a layer structure that is suitable for electrode and thermal sensitive materials of batteries [20]. VO_2 (C) is a little different, because its structure consists of VO_5 square pyramids [21]. Then, VO_2 (D) exhibits magnetic properties and can be changed to VO_2 (M) at $\approx 320\,°C$ [22]. Lastly, a relatively new phase VO_2 (P) was demonstrated that it can be transformed into VO_2 (M1) by rapid annealing [23].

Figure 1.2 shows the lattice structure of VO_2 below and above the MIT temperature [24]. The crystallographic structure of the high-temperature metallic phase VO_2 (R) is shown on the right: Two unit cells each containing 2 vanadium and 4 oxygen atoms. The arrangement of atoms in this phase is rutile – V atoms form a tetragonal lattice and are surrounded by O octahedra.

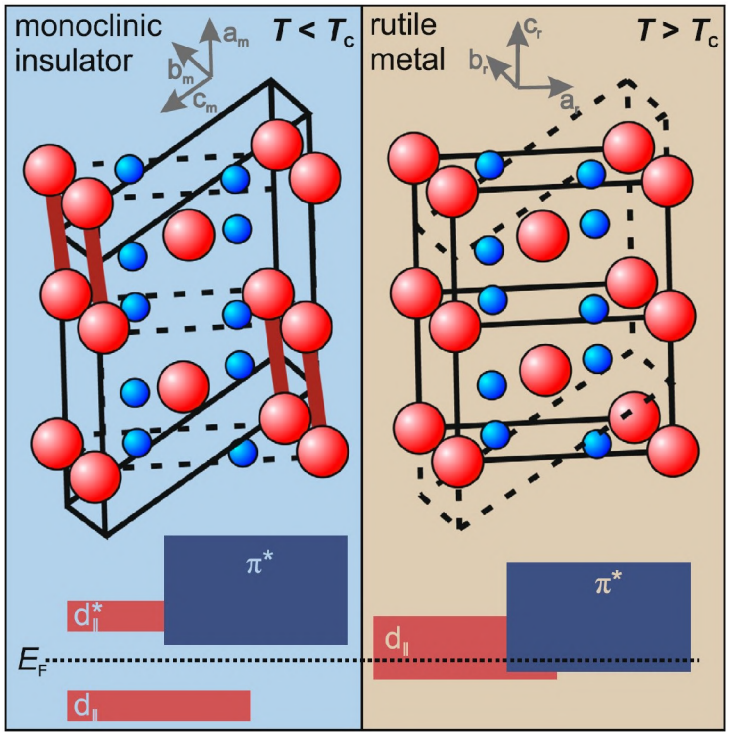

Figure 1.2: Comparison of the monoclinic (M1) insulating phase (left) and the tetragonal (rutile) metallic phase (right) of VO_2. **Top:** Crystallographic structures, unit cells are indicated by the solid lines. Red spheres represent vanadium, blue spheres represent oxygen. **Bottom:** Schematic representation of the VO_2 electronic band structure near the Fermi level. Adapted from [24]

When the temperature decreases below the MIT temperature, the V atoms dimerise and the dimers tilt from the rutile c_r axis. The crystallographic structure of the low-temperature insulating phase of VO_2 (M1) is shown on the left: The O octahedra are only slightly disturbed, but the V atoms are significantly moved. This structural change lowers the symmetry and doubles the unit cell – the monoclinic unit cell contains 4 vanadium and 8 oxygen atoms. The change of crystallographic structure is accompanied by $\approx 0.045\,\%$ change of volume.

VO_2 (M) has following unit cell parameters: $a = 0.575\,\text{nm}$, $b = 0.452\,\text{nm}$, $c = 0.538\,\text{nm}$, $\beta = 122.6°$. In the picture, the longer vertical distance between the two V atoms (red spheres) is 0.312 nm and the shorter spacing (bold red line) is 0.265 nm. On the other side, VO_2 (R) has following unit cell parameters: $a = b = 0.455\,\text{nm}$, $c = 0.286\,\text{nm}$, with the spacing between V atoms 0.285 nm [25].

1.2 Physical properties

There are several changes of physical properties during the MIT between the dielectric VO_2 (M1) and metallic VO_2 (R) phases: electrical, optical, and thermal.

An illustrative resistivity hysteresis of VO_2 is shown in Figure 1.3. A small thermal hysteresis is present between the heating and cooling process as the phase-transition points do not coincide with each other. This sharp transition from insulator to metal makes VO_2 widely used in ultrafast switches.

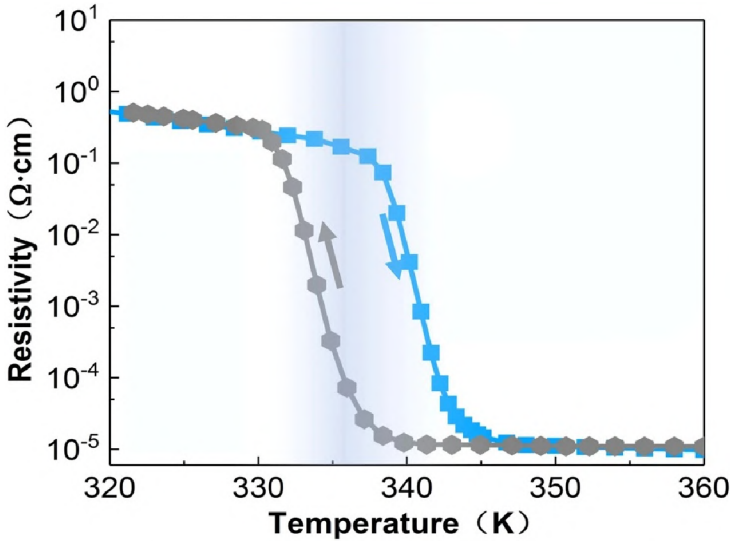

Figure 1.3: An illustrative resistivity hysteresis of VO_2 as a function of temperature. Adapted from [25].

Furthermore, many thermal properties of the MIT have been reported [26, 27]. In 2010, it was shown that the thermal conductivity in the metallic phase increases by 60 % [28]. Additionally, doped VO_2 exhibits an abrupt increase around the MIT, which is promising for future applications in thermal switching.

The optical properties of VO_2 during the MIT include a dramatic change in the IR region [29, 30]. At temperatures below the MIT temperature (insulating phase), V atoms pair and open an energy gap of 0.6 eV permitting high IR transmission. At temperatures above the MIT temperature (metallic phase), overlap between the Fermi level and the

V $3d$ band eliminate the band gap and as a result, the material is highly reflective or opaque in the near-infrared (NIR) region. The ability of VO_2 to modulate the NIR transparency makes it a promising material for a possible application in next-generation smart windows [31].

Optical properties of VO_2 thin films can be conveniently measured by ellipsometry. Figure 1.4 shows the reflectance measurement of the main sample used later within this Thesis – VO_2 thin film with thickness 550 nm on Si substrate prepared in an e-beam evaporator by Ing. Peter Kepič. The sample was measured at 30 °C and 90 °C. There is an evident difference in the real part n of the refractive index in the wavelength region between $\approx$ 600 nm and $\approx$ 2000 nm. Imaginary part k (absorption coefficient) of the refractive index is almost the same below $\approx$ 600 nm in both phases. However, after that the absorption of the insulating phase significantly decreases. In contrast, the metallic phase in this region becomes a strongly absorbing material.

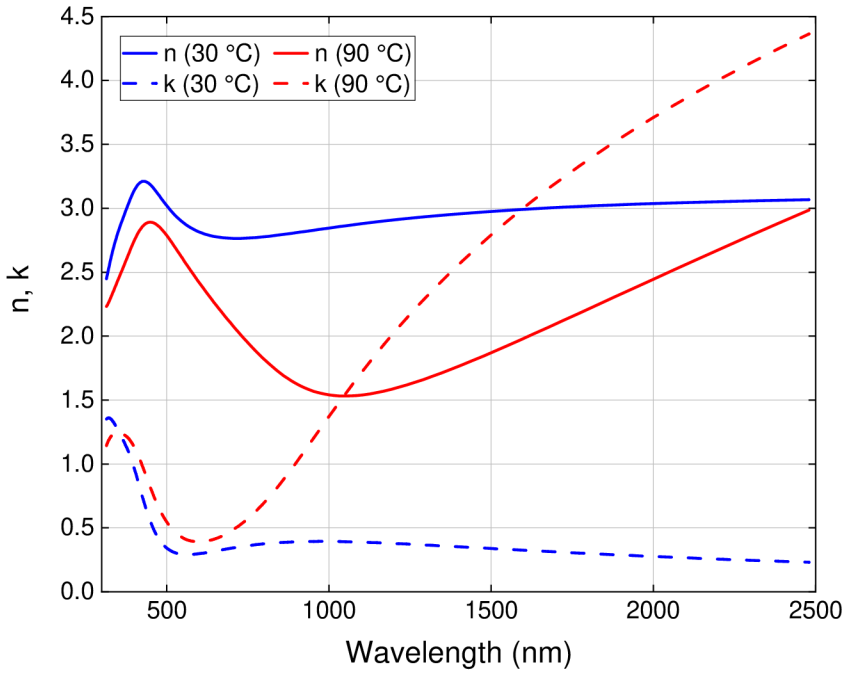

Figure 1.4: Ellipsometric measurement of the main sample used within this Thesis. Real (n) and imaginary (k) parts of the complex refractive index in insulating (blue curves) and metallic (red curves) phases.

2 Fabrication methods

The main goal of this Master's thesis is the fabrication of VO_2 samples suitable for transmission electron microscopy (TEM). First, in Section 2.1 is the review of fabrication methods used for the preparation of VO_2 thin films – their general description, advantages and disadvantages for the fabrication of VO_2 thin films, and their utilization within the scope of this Thesis. Then, in Section 2.2 we describe the fabrication of TEM samples from VO_2 thin films using the focused ion beam (FIB). Section 2.3 summarizes all the experimental results of the VO_2 TEM sample fabrication.

Except for the Kaufman ion beam sputtering deposition (IBSD) device, all the other equipment used in this Thesis is located at the Central European Institute of Technology (CEITEC) in one of its core facilities, the CEITEC Nano Research Infrastructure, which began full operation in 2016 and is the largest cleanroom nanocentre in the Czech Republic [32]. CEITEC Nano is made up of three main cleanroom parts:

- The *nanofabrication* laboratory (class 100[1] cleanroom), an area of 356 m^2.
- The *nanocharacterization* laboratory (class 100 000[2] cleanroom), an area of 1 337 m^2.
- The *structural analysis* laboratory (class 100 000 cleanroom), an area of 300 m^2.

2.1 Thin film deposition

Thin films of VO_2 can be obtained by various fabrication methods: pulsed laser deposition (PLD) [33, 34], evaporation [35, 36], ion beam sputtering deposition (IBSD) [37, 38], magnetron sputtering [39, 40], atomic layer deposition (ALD) [41, 42], molecular beam epitaxy (MBE) [43, 44], chemical vapor deposition (CVD) [45, 46], and chemical solution deposition (CSD) also known as sol-gel method [47, 48]. In our work, we used the first three methods mentioned above for the preparation of VO_2 thin films – PLD, evaporation, and IBSD – which will be discussed further in more detail.

First, we delve into a discussion about the PLD technique. PLD turned out to be one of the most promising methods suitable for fabricating thin films of VO_2 mainly due to the so-called stoichiometric (congruent) transfer, where material is transferred from the target to the substrate without a change in its composition (i.e., we obtain VO_2 thin film on the substrate out of the VO_2 target). However, this is not the case with both evaporation and IBSD, therefore obtaining VO_2 thin film with these methods is more challenging.

Although stoichiometric transfer is an advantage, there are other factors in each fabrication technique that must be optimized to obtain a VO_2 thin film that is undergoing a phase transition discussed in Section 1.1. Moreover, the fabrication of VO_2 thin films is in all cases a two-step process: the deposition itself and the subsequent post-annealing, which takes place in a vacuum furnace. There are a few parameters of annealing that must be optimized: temperature, oxygen flow, annealing time, base pressure[3], heating rate, and cool-down rate [49].

[1] A definition of the class 100 cleanroom: has less than 100 particles of 0.5 µm or bigger within a cubic foot of air (which is equivalent to ISO 5).

[2] A definition of the class 100 000 cleanroom: has less than 100 000 particles of 0.5 µm or bigger within a cubic foot of air (which is equivalent to ISO 8).

[3] Conversion of conventional pressure units: 1 mbar = 100 Pa; 1 Torr ≈ 133.322 Pa; 1 mbar ≈ 0.75 Torr.

Given these complications with the optimization of the fabrication of VO_2 thin films with each technique, we used a sample fabricated by evaporation by Ing. Peter Kepič during the work on his Master's thesis [49]. He optimized the whole process of evaporation of VO_2 and subsequent post-annealing so that the VO_2 thin films exhibited the desired phase transition. One such sample was used to fabricate both lamellae for further transmission electron microscopy (TEM) characterization.

Optimization of PLD and IBSD has been done by other Author's colleagues as well. However, work on the optimization was not concluded during this Thesis. Therefore, samples obtained by these methods could not be included in TEM characterization.

2.1.1 Pulsed laser deposition (PLD)

Pulsed laser deposition was developed shortly after the invention of a pulsed ruby laser source in the 1960s and was first used as a physical vapor deposition (PVD) technique for dielectric and semiconductor thin films in 1965 [50]. After decades of development and incorporation of new materials, PLD has become one of the most promising techniques for the fabrication of oxide films and other complex materials [51]. Figure 2.1 **(a)** shows a PLD device located in the nanofabrication laboratory (class 100 cleanrooms) at CEITEC Nano in Brno [52].

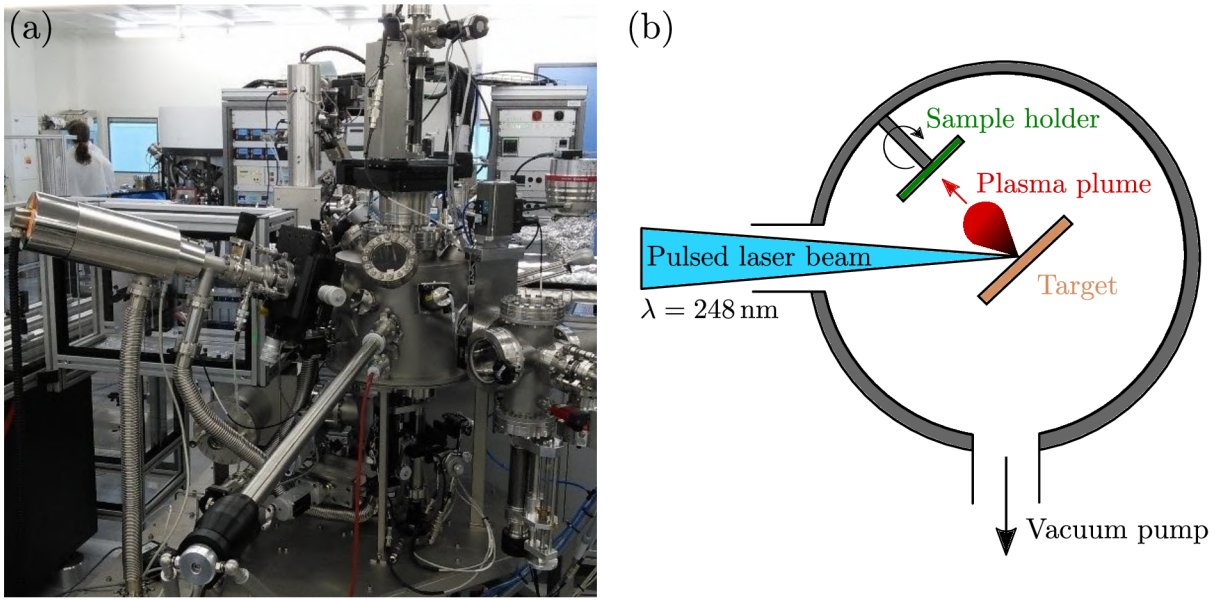

Figure 2.1: **(a)** PLD device at CEITEC equipped with a UV laser $\lambda = 248\,\text{nm}$. Adapted from [52]. **(b)** A schematic of a typical PLD experimental arrangement. Uniform ablation can be achieved by rastering and rotation of the target. Adapted from [53].

The first use of the PLD for VO_2 deposition was reported in 1993 by Borek et al. [54]. In the paper, they presented results from using the KrF pulsed excimer laser ($\lambda = 248\,\text{nm}$, pulse duration $\tau = 15\,\text{ns}$), which was used to ablate a metallic vanadium target in an ultra-high vacuum (UHV) chamber partially filled with Ar and O_2 (10:1) atmosphere. The pressure was kept at $p = 0.1 - 0.2\,\text{Torr}$ ($\approx 13.33 - 26.66\,\text{Pa}$), and the sapphire substrate was heated to $\approx 500\,°\text{C}$. Among these deposition properties, the partial oxygen pressure turned out to be the most critical variable in achieving pure VO_2. The last step was annealing for 1 h at the same temperature and pressure as the deposition to ensure that

the oxygen in the film was uniform and therefore preventing formation of other mixed oxides.

Shortly after, it was shown that it is possible to deposit VO_2 at high temperature but without annealing [55], and a few years later that it can even be achieved at room temperature [56].

In recent studies that focused on the fabrication of VO_2 thin films by PLD, various suitable substrates such as Si/SiO_2 [57], Al_2O_3 (sapphire) [58, 59], fused silica [60], and TiO_2 [61] were used. To achieve high quality VO_2 thin films, parameters such as laser energy, distance between the substrate and the target, gas pressure, deposition, and annealing temperature had to be adjusted.

Ablation process

Figure 2.1 **(b)** shows a schematic diagram of a typical PLD configuration. Although PLD is conceptually and experimentally simple, the laser–target interaction (ablation process) is quite complex; it is illustrated in Figure 2.2.

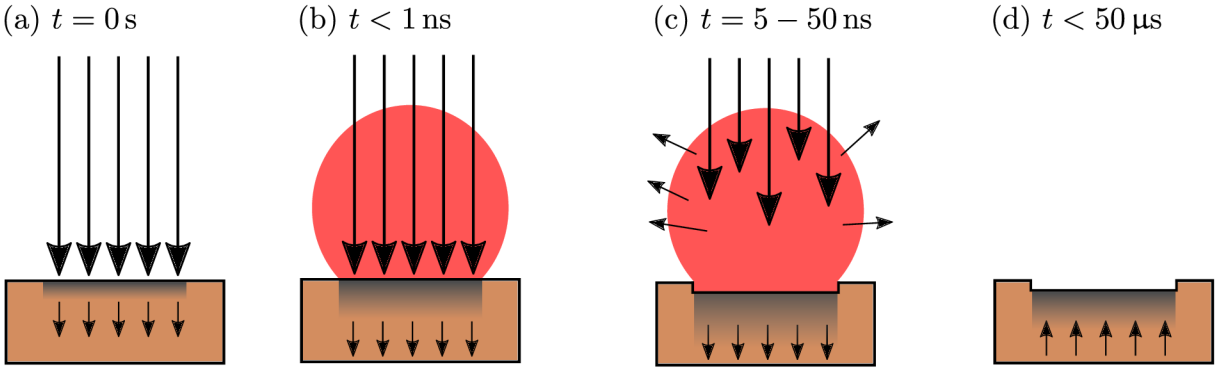

Figure 2.2: A schematic illustrating key elements of the pulsed laser ablation of the target. **(a)** Initial absorption of the laser radiation (long arrows), melting of the target material (shaded area). Short arrows indicate motion of the solid–liquid interface. **(b)** Melting continues, formation of a material vapor (red area). **(c)** Absorption of the laser radiation by the plasma plume (plasma shielding). The plasma plume then moves away from the target and hits the sample surface [$t = 4\,\mu\mathrm{s}$] [62]. **(d)** Re-solidification of the exposed area of the target and a crater formation. Adapted from [63, 64].

The PLD process runs in a chamber with high vacuum (HV) typically better than $p = 10^{-6}\,\mathrm{mbar}$ ($= 10^{-4}\,\mathrm{Pa}$), where a high-power pulsed laser beam with pulse duration $\tau = 10 - 50\,\mathrm{ns}$ and energy density $E_\mathrm{d} = 1 - 10\ \mathrm{J \cdot cm^{-2}}$ is focused on the target surface typically at an angle of 45°. The surface is rapidly heated, breakdown and ablation occur, and a dense plasma plume is formed. Plasma with a temperature of up to 5 000 K consists of neutral atoms, molecules, energetic electrons and ions in both the ground and excited states. When the plasma plume is formed, it absorbs the remaining part of the incident nanosecond laser pulse, which heats the plasma. The plasma now protects the target material from further ablation – this effect is called plasma shielding. To avoid repeated ablation from the same spot, the target is usually rotated or rastered.

The atoms and ions expand perpendicularly to the target surface and symmetrically around the surface normal. They are then deposited on the sample, where they nucleate during every pulse. The sample is located typically 5–10 cm from the target and can be

equipped with a sample heater. The resulting homogeneity of the film depends on the type of substrate, its temperature, the kinetic energies, and/or rates of various particles ablated from the target. Thus, after optimization of these fundamental parameters, polycrystalline or epitaxial single-crystal films can be grown.

The most widely used lasers for PLD nowadays are ultraviolet (UV) lasers, e.g., XeCl ($\lambda = 308\,\text{nm}$), KrF ($\lambda = 248\,\text{nm}$), ArF ($\lambda = 193\,\text{nm}$), and F_2 ($\lambda = 157\,\text{nm}$). However, lasers with longer wavelengths in the near infrared and visible, e.g., Nd:YAG laser ($\lambda = 532\,\text{nm}$, $\lambda = 1064\,\text{nm}$), and mid-infrared, e.g., CO_2 laser ($\lambda = 10.6\,\mu\text{m}$) can also be used [63].

Characteristics of PLD

One of the most notable characteristics of PLD is the so-called stoichiometric (congruent) transfer, which means that – given the correct energy density of the laser – films on the substrate have the same composition as the target material. It is a direct consequence of the highly nonthermal target erosion by a laser-generated plasma. This is what separates PLD from other methods such as sputtering and thermal evaporation. In both sputtering and thermal evaporation, the congruent transfer is not guaranteed due to a nonidentical sputtering rates and evaporation temperatures of different materials, respectively.

The growth of multilayered epitaxial heterostructures can be achieved with PLD by using separate targets in a multitarget "carousel" for quick exchange of the targets. By calibrating the deposition rate per laser pulse, the growth of each layer can be precisely controlled. Achieving faster growth rates can be done simply by increasing the laser pulse rate, while using very low deposition rates can control the growth of single atomic layers.

Another major advantage of this technique lies in the capability for reactive deposition in ambient gases, since no electron beams or hot filaments are needed in the chamber. Multicomponent materials that were previously difficult to fabricate (ferroelectric, ferrite, and biocompatible oxide ceramic materials) can now be grown with PLD in the form of high-quality thin films.

However, PLD also has some drawbacks, as is the case with every fabrication technique:

- Energy distribution within the plasma plume limits the deposition area to a few cm^2, which makes it unsuitable for large-scale film preparation.
- The target material under the plasma plume is still affected by the plasma heat, resulting in the ejection of macroscopic particulates called "laser droplets" created by the mechanism called "subsurface heating" [65].

2.1.2 Evaporation

Another commonly used PVD technique is evaporative deposition. The evaporation process is conceptually very simple: a high-purity material placed in a crucible is heated, melts, evaporates, and is deposited onto the sample. The entire process is carried out in a high vacuum chamber with pressure $p = 10^{-7}\,\text{mbar}$ ($= 10^{-5}\,\text{Pa}$) and the crucible must be of a material that can withstand high temperatures: typically boron nitride (BN), graphite (C), and aluminium oxide (Al_2O_3). Although sublimation source is also possible as an evaporation source, the crucible source is needed for evaporating materials in quantities of a few grams and more [66]. There are three types of evaporators that incorporate crucible sources: *resistive*, *inductive*, and *electron beam* heating systems [67].

Resistively heated system is the simplest type. Nevertheless, its major complication is the evaporation and outgassing from the filament wire used for resistive heating, since it must be heated to at least the same temperature as the material to be evaporated from the crucible. This does not pose a problem for the evaporation of materials with relatively low melting point such as aluminium ($T_{\text{melt}} = 660\,^{\circ}\text{C}$ [68]). However, there is often no suitable heating element for the deposition of refractory metals[4] ($T_{\text{melt}} > 2\,000\,^{\circ}\text{C}$ [68]).

Inductive heating system solves the aforementioned problem with evaporation and outgassing of the filament wire by using a coil for heating the crucible via Joule heating. The loss of material from the coil itself can be achieved by water cooling of the coil to keep its temperature below 100 °C. This inductive type of evaporator source can achieve high enough temperatures to evaporate refractory metals. However, although the coil can be cooled down, the contamination of to-be-deposited material from the crucible itself still remains a vital problem.

Electron beam (e-beam) evaporation sources avoid this problem by heating only the material inside the crucible, while the crucible itself can be cooled down. This e-beam source is schematically illustrated in Figure 2.3 **(b)**. A high-energy beam of electrons is ejected from an electron gun, which is located under the crucible to minimize deposition of the filament material (typically tungsten) onto the substrate. A bending magnet creates a strong magnetic field that bends the electron beam through 270° into the crucible. The beam can then be rastered across the material to melt different areas on its surface. Due to the directionality of the vapor, rotation of the sample holder is usually used during deposition to maintain the same film thickness throughout the sample. This plays an important role mainly for evaporation during the nanofabrication process, where off-axis deposition during evaporation can cause the formation of differently shaped structures [70].

Electron beam evaporation of VO_2 thin films from a VO_2 powder target has been reported with working pressure $p = 10^{-4}\,\text{Torr}$ ($\approx 1.3 \times 10^{-2}\,\text{Pa}$), constant deposition rate of 0.3 Å/s, and post-annealing [36]. Figure 2.3 **(a)** shows an e-beam evaporator located in the nanofabrication laboratory (class 100 cleanrooms) at CEITEC Nano in Brno [71]. In this evaporator, a VO_2 target was used for the deposition. The pressure during the deposition was kept at $p = 3.3 \times 10^{-5}\,\text{mbar}$ ($= 3.3 \times 10^{-3}\,\text{Pa}$) for the deposition rate 0.8 Å/s, which is suitable for the fabrication of thicker VO_2 layers with thicknesses of a few hundred nm (e.g., 500 nm).

Characteristics of evaporation

One of the main advantages of electron beam evaporation is the ability to achieve high deposition rates (a few Å/s) compared to other PVD methods [73]. However, very high rates can result in a worse control over material quality. Another advantage is that several different target materials can be inserted into the vacuum chamber and utilized by using a multiple-crucible carousel. This feature is useful in a variety of lift-off masking techniques for the deposition of multiple layers of different materials without breaking the vacuum between individual depositions.

[4]Refractory metals are a class of materials that share the common properties: very high melting temperature, mechanical properties (e.g., high hardness and strength), and high wear and corrosion resistance. The most common definition of refractory metals with a melting point $T_{\text{melt}} > 2\,000\,^{\circ}\text{C}$ includes 5 metals: niobium, molybdenum, tantalum, tungsten, and rhenium. Broader definition includes also 8 other metals with $T_{\text{melt}} > 1\,850\,^{\circ}\text{C}$: vanadium, hafnium, titanium, zirconium, ruthenium, osmium, rhodium, and iridium [69].

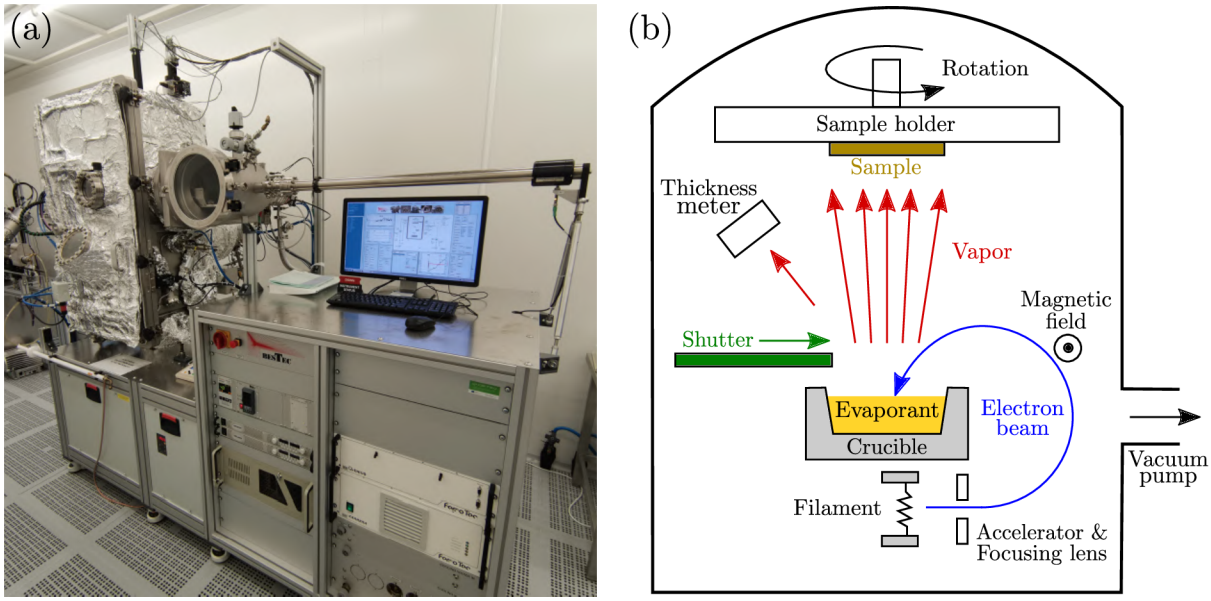

Figure 2.3: **(a)** Electron beam evaporator BESTEC at CEITEC. **(b)** A schematic of an electron beam (e-beam) evaporator. The electron beam (blue arrow) is first accelerated and then bent 270° by magnetic field into a crucible, which is filled with the target material (evaporant). The evaporated material (red arrows) is then deposited onto our sample, which is usually rotated during the deposition. Adapted from [49, 72].

On the other hand, evaporation as a deposition technique suffers from two major limitations [74]. The first is that the thermally evaporated metal atoms condense at a much colder sample surface. The result is that a thin film is deposited; however, it is subject to issues related to wetting, nucleation, cluster formation, and agglomeration, which can yield inadequate film properties. The second constraint is the previously mentioned congruent transfer, which is in the case of evaporation not guaranteed due to the different evaporation temperatures of evaporated materials. In other words, since the evaporation rate of two (or more) components of the material in the same crucible can be very different, the material component with lower melting point will evaporate first, leaving the other components behind. The only solution to this problem is to have two adjacent crucibles, one for each material. This technique is commonly known as co-evaporation [75].

2.1.3 Ion beam sputtering deposition (IBSD)

Sputtering deposition is another PVD technique and is widely used for thin film deposition in many industries, e.g., metallization on semiconductor materials, reflective coatings on compact discs (CDs), and hard coatings on tools and engine parts [76]. Sputtering incorporates several types of sputtering systems that are used in practice: direct current (DC) sputtering, radio frequency (RF) sputtering, magnetron sputtering, and ion beam sputtering [77].

Third PVD technique that will be discussed in this text is ion beam sputtering deposition (IBSD), which is a non-thermal vaporization technique used for the deposition of thin films. The IBSD process involves the bombardment of a solid surface of a target with energetic ions, schematically illustrated in Figure 2.4 **(b)**. The target is made of the desired material that needs to be deposited on the substrate. Energetic ions of an inert

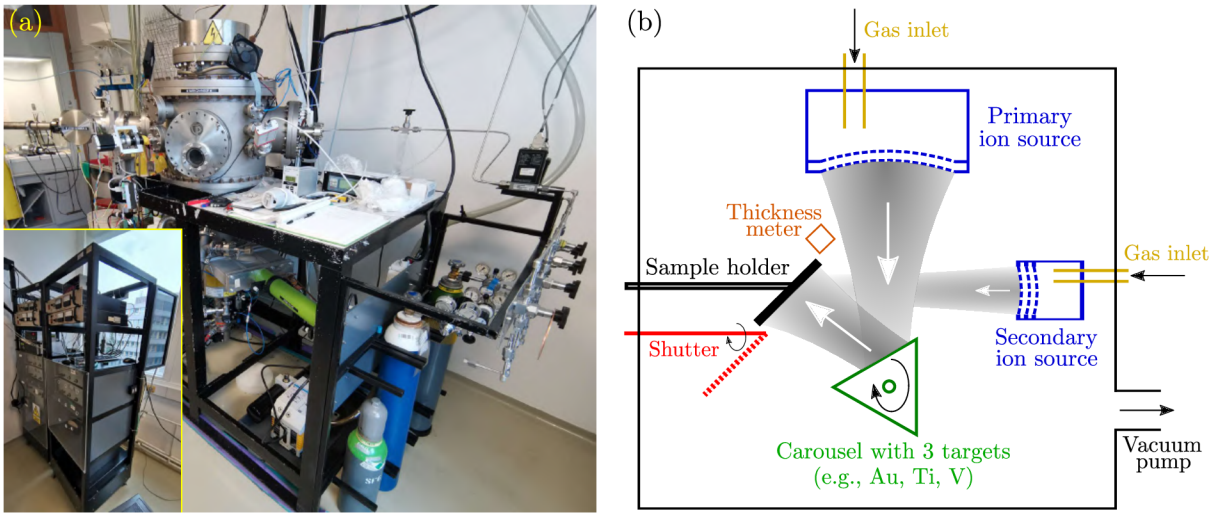

Figure 2.4: **(a)** Homemade IBSD/IBAD deposition device "Kaufman". Inset shows the periphery with voltage sources. **(b)** A schematic of ion beam sputtering chamber, where energetic Ar^+ ions coming from the primary ion source hit the target made from material we want to deposit. This material is then sputtered from the target surface and is deposited onto the sample. Adapted from [78].

gas scatter surface atoms of the target backward onto the substrate, where the sputtered particles condense and a thin layer is formed.

This technique can also be used for the deposition of VO_2 thin films, where varying amounts of oxygen during the deposition play an important role, as was shown in the work of Chain [79]. In the paper, a pure vanadium target was bombarded by a beam containing a mixture of argon and oxygen ions, which turned out to have a strong influence on the growth characteristics and optical properties of the resulting film. The substrate temperature during the deposition was 505 °C and working pressure was $p = 3 \times 10^{-4}$ Torr ($\approx 4 \times 10^{-2}$ Pa). The result is as follows: oxygen content in the range of 15 % – 25 % in the beam produced switchable VO_2 thin film, whereas oxygen content in the range of 30 % – 50 % was identified as V_2O_5. Since the substrate was at high temperature during the deposition, no post-annealing was necessary to achieve the switchable VO_2 thin film.

Figure 2.4 **(a)** shows a homemade ion beam sputtering device called "Kaufman", which is located in the cleanrooms class 100 000 at the Institute of Physical Engineering at the Brno University of Technology [80]. An important part of this device is a Kaufman ion source [81]. Electrons are emitted from a cathode as a result of thermal emission and then drawn to a positive anode. Along the way they collide with atoms of the inert gas which leads to the ionization of these atoms. The electrons are affected by magnetic field resulting in a helical path, therefore increasing the likelihood of collisions with atoms of the inert gas, in our case Ar^+ ions.

We can also use a secondary ion source for the so-called ion beam assisted deposition (IBAD) [82]. The ions emitted by this source have lower energy and are emitted directly on the substrate. Using IBAD (secondary source) in conjunction with IBSD (primary source) can modify a number of characteristics and properties of the thin film such as adhesion, grain size and morphology, optical properties, hardness and ductility, and modification of residual stresses [83].

The deposition process takes place in a high vacuum chamber with working pressure $p = 1.4 \times 10^{-5}$ mbar ($= 1.4 \times 10^{-3}$ Pa), oxygen flow rate 5.5 sccm, and the deposition

rate of vanadium 0.1 Å/s. The deposition rate is lower than in the case of evaporation (0.8 Å/s), therefore the fabrication of thicker layers takes substantially longer time.

Characteristics of IBSD

One of the advantages of sputtering methods in general is a quick fabrication of heterostructures, which can be achieved by simple exchange of target materials by rotation of a target holder. Various high-purity target materials can be used, such as gold, titanium, aluminium, and, among many others, vanadium. Specifically, IBSD has some advantages over other PVD techniques [84]:

- Low working pressure, typically lower than $p = 10^{-4}$ mbar ($= 10^{-2}$ Pa).
- Spatial separation of the ion beam source, target, and substrate. Therefore, the geometrical and ion beam parameters can be varied, resulting in different energy distributions of the particles that form the thin film.
- As a consequence of spatial separation, the interaction of plasma, target, and substrate is avoided, which is not the case in magnetron sputtering (e.g., yielding arcing [85]).

Technological disadvantages of IBSD compared to evaporation and magnetron sputtering include:

- Much lower deposition rate (in our case the deposition rate of vanadium is 0.1 Å/s compared to 0.8 Å/s for evaporation).
- Ion beam sources including the periphery components are more complex, which limits industrial use due to the higher cost.
- The previously discussed congruent transfer of compound target material is not guaranteed due to the different sputtering rates of the individual components of the material, which is also known as preferential sputtering [86]. Similarly to evaporation (where the problem was a different evaporation temperature), this can be resolved by the sputtering of multiple targets, a technique known as co-sputtering. Additionally, oxygen deficiency is observed when growing oxide thin films, which can be compensated by providing oxygen as a background gas, i.e., depositing in an ambient pressure containing a partial pressure of the reactive gas [73].

2.2 Focused ion beam (FIB)

Focused ion beam (FIB) microscopes were mainly developed during the late 1970s and early 1980s and quickly became irreplaceable tools for localized milling (etching), surface modification, and deposition and imaging of materials [87]. This was possible due to the increase in source brightness, which was a consequence of the invention of the liquid metal ion source (LMIS) [88].

A typical LMIS comprises a tungsten (W) needle attached to a reservoir that holds the metal source material. The emission occurs as follows: source material is heated, wets the W needle, an electric field applied to the tip shapes the material into a "Taylor cone", and when the cone tip is small enough, the extraction voltage pulls the atoms of the material from the tip. Several metallic elements or alloy sources can be used as the source material. However, gallium (Ga) is nowadays the most widely used due to its low melting point ($T_{melt} = 29.8\,°C$), low surface free energy, and other properties combined

with its emission characteristics, which allows high angular intensity with a small energy spread [89].

FIB technology was initially widely used in the semiconductor industry for repairing masks, repairing and editing integrated circuits, and preparing the transmission electron microscopy (TEM) specimens; later, its usage expanded to much broader range of scientific and technological disciplines [90]. However, despite their potential in other areas, many FIB systems are nowadays largely used to prepare cross-section sample lamellae for transmission electron microscopy (TEM) [91, 92].

In the scope of this Master's thesis, we worked with the dual beam microscope Tescan LYRA3, which combines FIB and SEM. Focused ion beam column is equipped with Ga LMIS source. The microscope is located in the nanocharacterization laboratory (class 100 000 cleanrooms) at CEITEC Nano and is shown in Figure 2.5 **(a)** [93]. In Figure 2.5 **(b)** is the infrared (IR) view of the device chamber. This chamber view is present during the measurements as a visual aid to help avoid collisions of the stage with the objectives or detectors. In this chamber with vacuum pressure $p < 9 \times 10^{-3}$, Pa, the electron beam hits the sample perpendicular to its surface when the stage is at 0° tilt. When working with FIB, the stage is usually rotated by 55° (shown in the image) so that the ion beam hits the sample perpendicular to its surface. The SEM/FIB intersection is at the working distance (WD) 9 mm. The 55° tilt is also convenient because the gas injection system (GIS) can be inserted without hitting the sample surface.

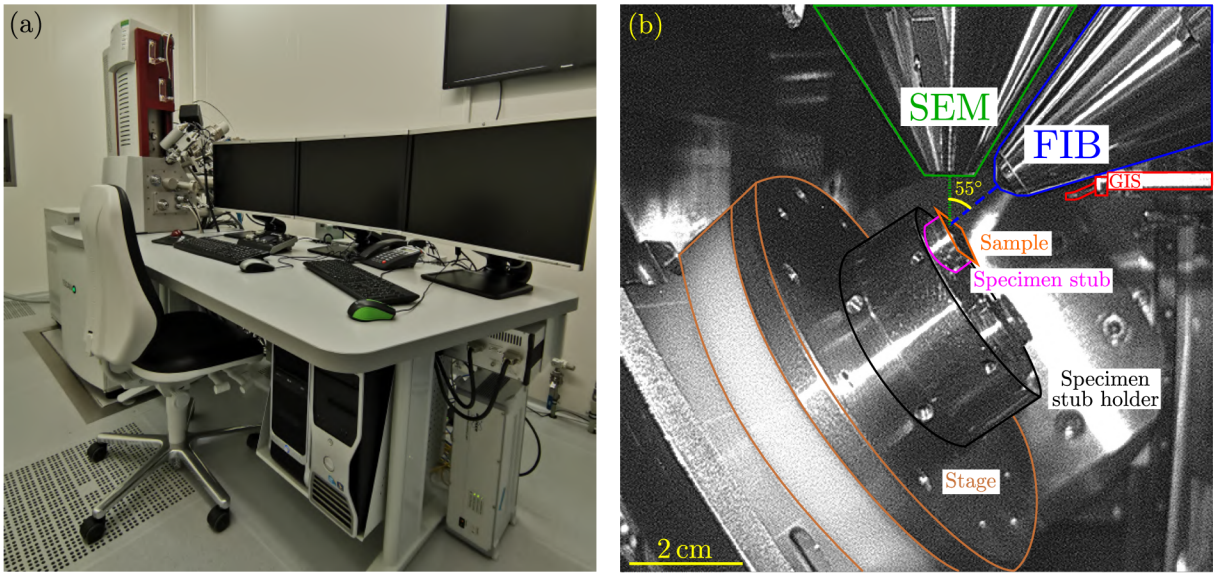

Figure 2.5: **(a)** Dual-beam SEM-FIB microscope Tescan LYRA3 at CEITEC. **(b)** Device chamber with outlined main parts of the microscope. GIS is shown in a "parking" position; in a "working" position it is around 0.5 mm away from the sample surface.

We can use SEM for imaging of both secondary electrons (SE) and backscattered electrons (BSE), while an energy dispersive X-ray (EDX) detector for chemical and elemental analysis is also present. Nevertheless, for the lamellae preparation, GIS with inlets for 5 precursors is essential for deposition and etching of materials: insulator (SiO_x), water, fluorine, platinum, tungsten. Within this thesis, we used only the Pt precursor. GIS enables us, for example, to attach the lamella to the nanomanipulator and freely move it to a different position. Another essential parts of the microscope are two (left and right) nanomanipulators (tungsten probes). They are not visible in Figure 2.5 **(b)**, but the left

nanomanipulator would descend close to the sample from behind the SEM column, the right nanomanipulator then from the other side.

The device is equipped with a specimen stage that can rotate, tilt, and move in xyz directions, which is crucial for the fabrication of lamellae. More detailed information on the fabrication of lamellae in general will be described below, while the description of the fabrication of VO_2 lamellae used for the TEM characterization will be discussed in Section 2.3.

Characteristics of FIB

When discussing the advantages of FIB, one could compare it to a similar top-down nanofabrication technique – electron beam lithography (EBL) [94]. EBL is a nanolithography technique used for patterning mesoscopic structures or systems with high resolution in feature size, where sub-10 nm resolution has been reported [95]. However, FIB can be used for direct sample patterning and therefore does not require the lithography process as EBL does. Moreover, the EBL is used for planar samples whereas the main advantage of FIB is its usage in other non-planar fabrication processes, such as the lamellae preparation used in this Master's thesis, or, for example, custom adjustments of probes for scanning near-filed optical microscopy (SNOM) used in the author's Bachelor's thesis [96].

More suitable and illustrative would be the comparison of FIB to an SEM. The main difference are the projectiles used in both techniques – electrons in SEM and ions in FIB – and the vast difference between their masses[5]. Larger mass of ions is the reason for their fabrication attribute, however, it is also their biggest disadvantage – ion beam will sputter and damage the region of interest on the sample even at low beam currents, which poses a problem when taking the image. This led to the development of nowadays commonly used dual beam SEM-FIB systems. In these instruments, FIB is primarily (but not exclusively, as will be discussed during the lamella fabrication) used for sputtering rather than imaging. The FIB can be used for imaging, but one must bear in mind that doing so will damage the sample, so the use of a lower current is recommended.

The main disadvantage of FIB is caused by the nature of the milling process – ion collisions can lead to ion implantation and cause amorphization of the material. In semiconductor materials, the thickness of the amorphous layer is roughly proportional to the Ga ion implantation range, which in turn is proportional to the energy of the Ga ions and also depends on the angle of incidence [97]. For example, the reduction of the amorphous layer in Si with decreasing Ga energy at glancing angles has been reported as follows: for 30 keV, 5 keV, and 2 keV, the damage was $\approx$ 22 nm, $\approx$ 2.5 nm, and $\approx$ 1 nm, respectively [98]. Therefore, preparation of TEM lamellae with a reduced amorphous layer is achieved by final polishing with ions of very low energy.

2.2.1 TEM lamella fabrication

FIB as a nanofabrication tool played an integral role in the sample fabrication process within this Thesis. It was utilized for the fabrication of thin samples – lamellae[6] – suit-

[5] $m_{\mathrm{Ga}} = 1.158^{-25}$ kg; $m_{\mathrm{e}} = 9.109^{-31}$ kg

[6] Plural of lamella, which means a thin layer, a membrane, or a plate of tissue. Its origin dates to the late 17th century and comes from Latin. It is a diminutive of a word *lamina*, which means *thin plate* [99].

able for analysis in the transmission electron microscope (TEM). The standard lamella fabrication process will be described in the following text.

First, we need to find the region of interest on our sample, where we want to make the lamella from. The stage needs to be tilted (to 55°) during the fabrication so that the FIB column is perpendicular to the surface of the sample, therefore the SEM images are taken from the point of view of 55° with respect to the surface normal. Using the gas injection system (GIS), we deposit two protective layers of Pt on the surface of our sample: first a thin layer ($< 100\,\text{nm}$) using focused electron beam induced deposition (FEBID), and then a thicker layer ($1 - 2\,\mu\text{m}$) using focused ion beam induced deposition (FIBID). This results in a Pt block, which is approximately $1.5 \times 10\,\mu\text{m}^2$ with a height of $\approx 2\,\mu\text{m}$. This Pt block is shown in Figure 2.6 **(a)**, where both Pt layers are indistinguishable from each other. FEBID is used first to avoid the implantation of ions into the surface of our to-be lamella, whereas the majority of the protective layer is deposited using FIBID, because of its higher deposition rate and therefore faster deposition of thicker layers.

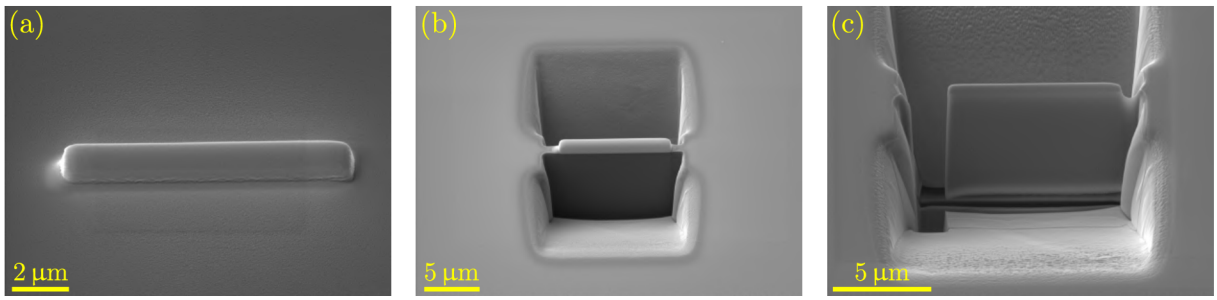

Figure 2.6: Lamella fabrication process (part 1 out of 3). **(a)** FEBID and FIBID protective Pt layer deposition on top of our region of interest. **(b)** Rough milling to create a deep trench around the lamella. **(c)** Rough polishing and undercut. Lamella is now connected with the sample only by its right side. SEM images courtesy of Ing. Eva Kolíbalová, Ph.D.

We then proceed with a rough milling of the surface on both sides of the Pt protective layer. It is called rough milling, because a very high ion beam current ($> 5\,\text{nA}$) is used to speed up the process. We create a stair-like shape shown in Figure 2.6 **(b)** with its depth increasing with the position to the protective Pt layer. The depth of the trench near the layer is approximately $5\,\mu\text{m}$. It is advised to position the milling pattern at least $1\,\mu\text{m}$ away from the edges of Pt layer, since the high current beam tends to be less accurate and we therefore avoid the damage or destruction of our region of interest. The trench should be large enough to later perform a safe lift-out of the lamella without hitting the walls of the sample.

In the third step, we proceed with rough polishing and undercut of the lamella. For the rough polishing (rough, because there will be another polishing with a lower current in the last fabrication step), we use the FIB current of $\approx 0.8\,\text{nA}$ to remove the remaining material next to the protective layer, which is left after the rough milling in the previous step. This way, we thin down the lamella more or less to the thickness of the protective layer of Pt, which is $1.5\,\mu\text{m}$. However, a lamella that is too thin ($< 1\,\mu\text{m}$) is difficult to manipulate in further steps. We then tilt the stage (to 7°) so that we can cut the lamella to free it from below and from one side. The result, which can be seen in Figure 2.6 **(c)**, is that the lamella is held to the rest of the sample only by one side (on the right) and is free elsewhere.

The next step in the lamella fabrication procedure is critical and very often leads to the destruction of the lamella. In order to move the lamella, we need to attach it to a (left) nanomanipulator, which is a tungsten probe with a tip radius 0.5 µm [100]. The first major complication is the movement of the nanomanipulator close to the lamella. This can be very tricky, because an operator has to watch its movement with both SEM and FIB in order to safely navigate the nanomanipulator tip to the tilted surface. By using not only SEM but also FIB we get the image from different angles and therefore are able to view the movement of the nanomanipulator in 3D. This is illustrated in Figure 2.7 **(a)**, **(b)**. The SEM image of our lamella shown in **(a)** and the FIB image shown in **(b)** were taken at the same time. The tip of the nanomanipulator is clearly visible at a different angle at the left side in both images.

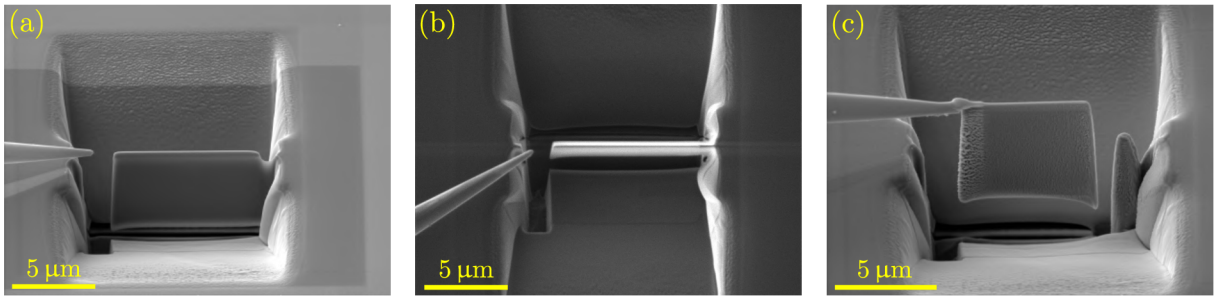

Figure 2.7: Lamella fabrication process (part 2 out of 3). A nanomanipulator approach close to the lamella in SEM **(a)** and FIB **(b)** image. **(c)** Attachment of the nanomanipulator tip and lamella release. SEM and FIB images courtesy of Ing. Eva Kolíbalová, Ph.D.

During this procedure, the FIB is used for imaging at low currents to avoid damage to the sample (or rather the protective layer, since we image the lamella with FIB from above). Then, the GIS nozzle is inserted to the vicinity of the lamella, nanomanipulator is slowly and carefully moved so that it (almost) touches the lamella, and a block of Pt is deposited to weld the nanomanipulator tip with the lamella. Finally, the lamella is freed by cutting the remaining right side that still attaches it to the rest of the sample. The tip with the lamella is then very carefully moved to the left and slightly higher to place it in the center of the trench, as illustrated in Figure 2.7 **(c)**. This is to ensure that it is truly free (bottom right corner sometimes still holds the lamella due to the insufficient cut) and that it does not accidentally hit the wall when moving it away from the trench. Only at this point can the GIS nozzle be retracted (due to vibrations), and the lamella is then free to move around the chamber attached to the nanomanipulator.

Conventionally, the lamellae are attached to a Cu lift-out grid, which is used for their characterization in the TEM. Such lift-out grid placed inside a groove in an SEM specimen stub is shown in Figure 2.8 **(a)**. Figure 2.8 **(b)** then shown a detail of an area with four columns labelled A–D. The lamellae are usually placed on these columns in marked positions near the top of the columns. As a consequence of handling the holder with the tweezers, placing the lamellae in the periphery positions is not recommended. Figure 2.8 **(c)** shows two possible placements of the lamellae on the Cu grid – at the side (bottom schematic) or inside the "V" top of the column (top schematic). In this work we used only the side mounting position shown in the bottom picture.

The nanomanipulator with the attached lamella is brought close to the Cu grid and the GIS nozzle is inserted, as is shown in Figure 2.9 **(a)**. This procedure is fairly safe compared to the previous lift-out step. In Figure 2.9 **(b)** a careful approach of the tip

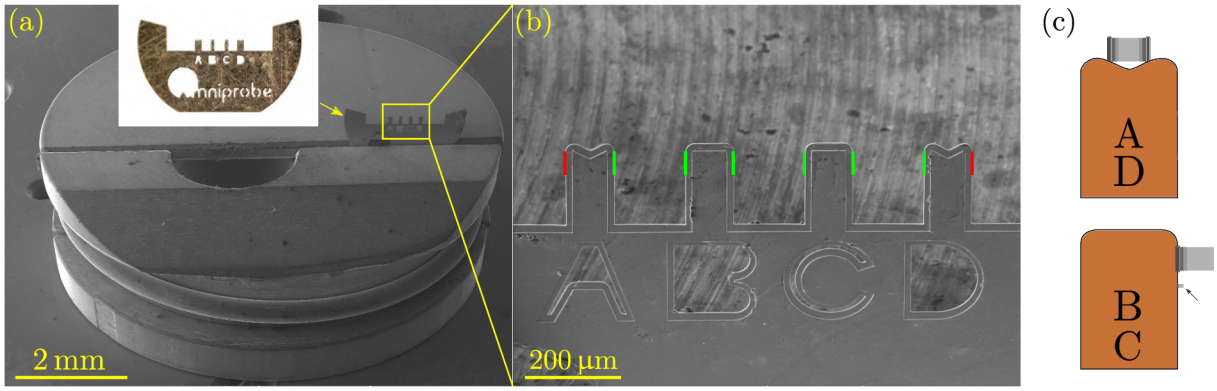

Figure 2.8: **(a)** Standard Cu lift-out grid for TEM lamellae placed inside a groove in an SEM specimen stub. Inset shows the Cu grid from Omniprobe, adapted from [101]. **(b)** Detail of the Cu lift-out grid showing four labeled columns with marked "safe" (green) and "unsafe" (red) side mounting positions. SEM images courtesy of Ing. Eva Kolíbalová, Ph.D. **(c)** A schematic of the two main strategies of lamella attachment to the Cu lift-out grid for TEM. Note that the lamellae sizes have been significantly increased – the real-size lamella with typical dimensions $7 \times 5\,\mu m^2$ is shown for comparison and marked with an arrow.

with the lamella close to the Cu grid is shown. A contact is not necessary; a gap of a few hundred nanometers is satisfactory. The lamella is attached to the grid with Pt by GIS, and the nanomanipulator is detached by cutting it with FIB. The successful transfer is shown in Figure 2.9 **(c)**.

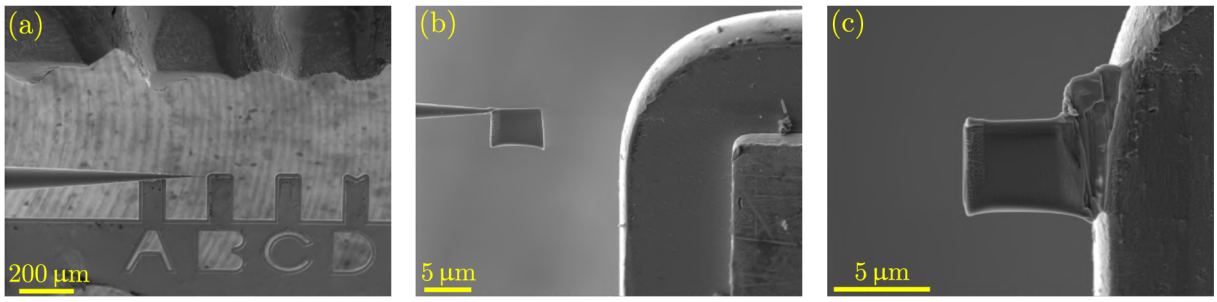

Figure 2.9: Lamella fabrication process (part 3 out of 3). **(a)** Transfer of the nanomanipulator with the lamella to the Cu grid. Part of the GIS nozzle is visible at the top of the image. **(b)** Careful approach close to the Cu grid. **(c)** Attachment of the lamella to the Cu grid and a nanomanipulator release. SEM images courtesy of Ing. Eva Kolíbalová, Ph.D.

When the lamella is attached to the grid, we proceed with the final steps of the lamella fabrication process, which consist of thinning and polishing the lamella for TEM characterization. First, we thin down the lamella to the thickness $\approx 100\,nm$ by using lower ion beam current ($\approx 80\,pA$). Then, we use lower ion beam voltage (5 kV instead of the usual 30 kV) and lower current ($\approx 40\,pA$) on a slightly tilted lamella to polish its surface and thin it further down to $< 100\,nm$. The slight tilt is needed for a better shape of the lamella; otherwise, it would be thinner at the top and thicker at the bottom. Subsequent polishing at low ion beam voltage minimizes the amorphous layer caused by the high-energy beam and decreases the depth of gallium implantation. As discussed previously, the depth of the damaged area in nanometers is approximately the same as the energy of the ion beam in keV (i.e., 30 keV ion beam causes 30 nm of gallium implantation

and amorphization). Therefore, 5 keV and 2 keV ion beams are usually used for the final polishing of the lamella. After this final step, the lamella is ready for the characterization in the TEM.

2.3 Results

This Section contains the experimental results of the VO_2 sample fabrication, which is the main focus of this Master's thesis. It is divided into 3 parts:

1. Sample fabrication from a purchased VO_2 powder
2. Preparation of a standard lamella for a TEM Cu grid.
3. Preparation of a lamella for a TEM heating chip.

These parts are in chronological order and with later parts increases the difficulty of the sample fabrication. However, the later parts also give us the most coveted information from the TEM characterization, which will be discussed for all samples in the next Chapter in the Section 3.3.

2.3.1 VO_2 powder

The first sample that was fabricated for the TEM was made of a VO_2 powder with the purity of 99.5 % [102]. Approximately one gram of the powder was mixed with deionized (DI) water directly in a new Eppendorf tube® to avoid contamination from using a general-use glass beaker. It was then put in an ultrasound bath for 5 minutes, at 25 °C, and frequency 37 kHz. The resulting solution is shown as an inset in Figure 2.10 **(a)**. A drop of the solution was pipetted onto a TEM grid called the holley carbon (C) grid [103].

The holley C grid has holes with diameters up to a few micrometers and is therefore suitable for imaging of samples without any material background (as would be the case with a continuous film). The downside is that the smaller particles fall through and only some bigger particles remain on top of the grid. Figure 2.10 **(a)** shows the holey C grid without the VO_2 powder in an optical microscope. The membrane is separated into many fields with a distinct letter "A" in the middle for a better orientation on the grid. Figure 2.10 **(b)** shows an overview of the same grid taken with an SEM Verios 460L located in the nanocharacterization laboratory (class 100 000 cleanrooms) at CEITEC Nano [104]. In the overview, the brighter fields contain a very high density of VO_2 powder pieces and are not suitable for the TEM characterization, while the darker fields are more suitable because they contain only a small portion of VO_2 powder pieces.

For the TEM characterization, we focused our attention on the darker fields. There we could find a few of the scattered VO_2 powder pieces that were:

- Partially lying across an empty space of the grid
- Thin enough for TEM characterization.

One such field with dimensions $65 \times 65\,\mu m^2$ is highlighted and shown in more detail in Figure 2.10 **(c)**. Here we can see the structure of the holley C grid (grey web) with holes (dark spaces) and scattered VO_2 powder pieces of various sizes and shapes (brighter parts on top of the grey web).

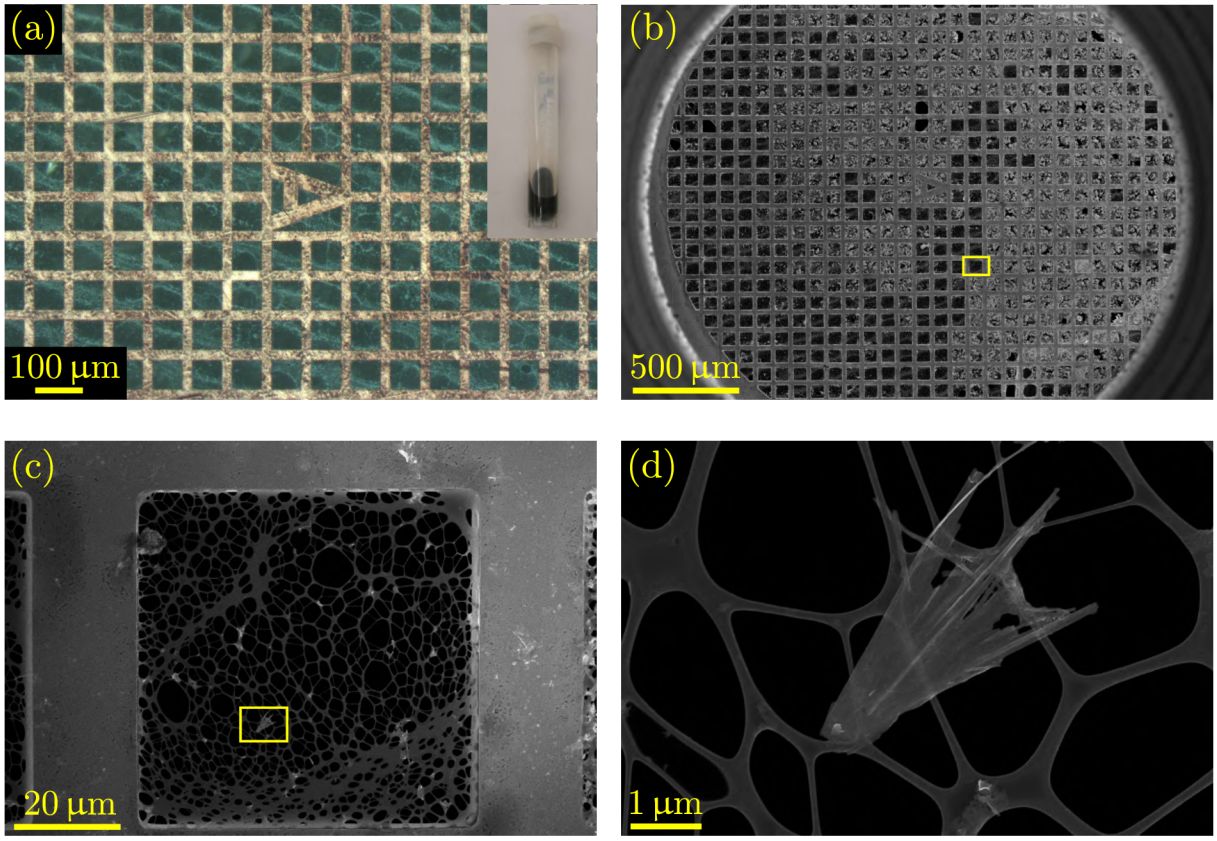

Figure 2.10: VO_2 powder (purity 99,5 %) on holley C grid. **(a)** Image from an optical microscope of a clean holley C grid. Inset shows the mixture of VO_2 powder with DI water in an Eppendorf tube®. **(b)** SEM image of the holley C grid with VO_2 powder particles on top. Brighter fields contain higher density of VO_2 powder particles than darker fields. **(c)** An exemplary grid field with VO_2 powder pieces. **(d)** Selected "paw" structure for further TEM characterization.

One of such powder pieces was highlighted and is shown in more detail in Figure 2.10 **(d)**. This powder piece – a "paw"[7] structure – is suitable for further TEM characterization, because it is thin and a major part of it is located above the hole in the holley C grid.

2.3.2 VO_2 thin film – lamella on a TEM Cu grid

Fabrication of the lamella on a TEM Cu grid follows the process of the TEM lamella fabrication thoroughly described in Section 2.2.1. The lamella was fabricated from a VO_2 thin film of thickness $\approx 550\,\text{nm}$. The sample was prepared by Ing. Peter Kepič by evaporation, which was described in Section 2.1.2.

Figure 2.11 **(a)** shows an SEM image of the resulting lamella on the TEM Cu grid, where the boundaries of its components are highlighted. The composition of the lamella is then schematically illustrated in Figure 2.11 **(b)**. Here, individual thinning steps are indicated with white vertical lines that are also partially visible in **(a)**. Grey area 1 (far

[7]Note that the combination of powder pieces is completely haphazard. Therefore, any resemblance to real entity, living or dead, is purely coincidental. However, an evident anisodactyl toe arrangement (three toes in front and the *hallux* pointing back – here without the hind toe) combined with palmate webbing (only anterior toes joined by webbing) is a common foot type characteristic for ducks, geese, swans, gulls, terns, and other aquatic birds [105].

right) has the thickness of the original lamella after lift-out (≈ 2 µm) and is too thick for TEM characterization. Therefore, we proceeded with subsequent thinning steps to obtain lamella with thickness below 100 nm. First substantial thinning resulted in area 2 with thickness ≈ 200 nm. Second thinning gave us the lamella with thickness ≈ 120 nm (adjacent area 3 as well as its second part on the far left). Only after the last thinning we obtained area 4 with the desired thickness ≈ 80 nm.

When using an electron beam with low voltage (5 kV or 3 kV), we can get a qualitative assessment of its thickness due to the transparency of the lamella: the darker parts are thicker, meanwhile the brighter parts indicate lower thickness. However, thickness is measured in the cross section (viewed from above). Nevertheless, it is not possible to precisely measure the thicknesses of the thinned parts of the lamella. For that reason, the aforementioned thicknesses are only a rough estimate.

In the SEM image, there are clearly visible dark spots in the VO_2 thin film. After imaging in TEM, these dark spots turned out to be cavities. This gave us valuable information that the VO_2 film prepared by evaporation is rather a porous material than a uniform one.

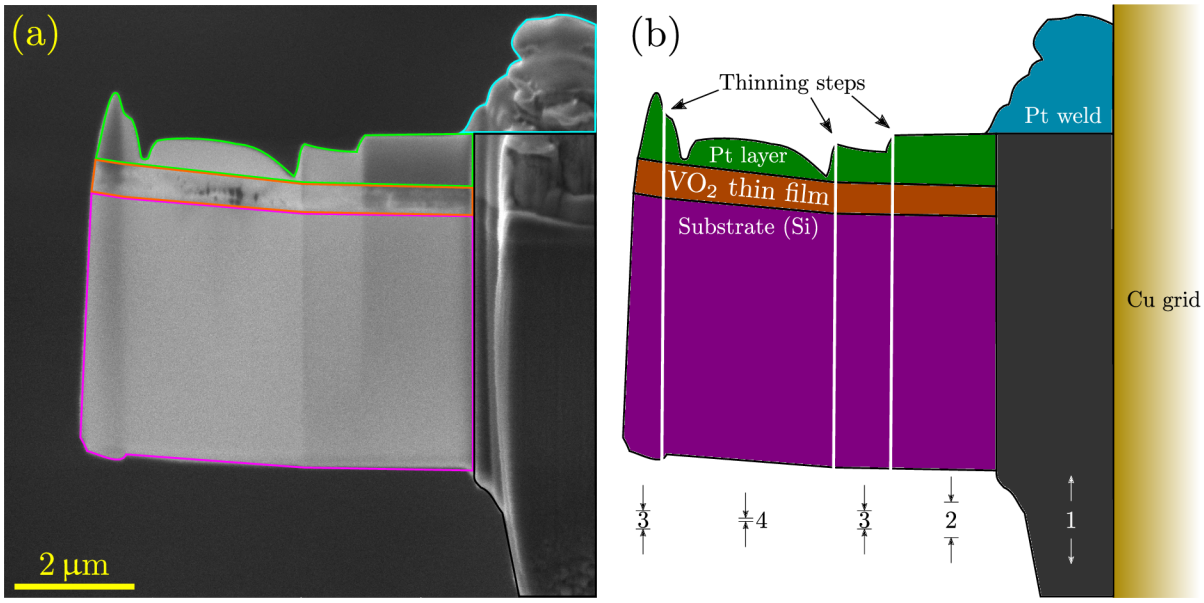

Figure 2.11: Lamella on a TEM Cu grid. **(a)** SEM image of the lamella with highlighted boundaries of its components. **(b)** Schematically illustrated composition of the lamella. Numbered illustrations under the lamella represent the thicknesses of the individual parts of the lamella: (1) thickness of the lamella after lift-out without thinning (≈ 2 µm), (2) first thinning step (≈ 200 nm), (3) second thinning step (≈ 120 nm), (4) last thinning step, very thin lamella suitable for the TEM imaging and characterization (≈ 80 nm).

2.3.3 VO_2 thin film – lamella on a TEM heating chip

For the preparation of this lamella, we used the same sample[8] as for the preparation of the lamella on a TEM Cu grid described above. The main difference between these two lamellae is the type of the TEM characterization platform where they are placed – Cu grid

[8]The sample dimensions are $8 \times 8\,\mathrm{mm}^2$ and the area needed for one lamella lift-out is approximately only $25 \times 25\,\mu\mathrm{m}^2$.

or heating chip. Cu grid is convenient, because the attachment and preparation of lamella is relatively simple. However, it allows us to measure only at room temperature[9]. Since one of the most interesting features of VO_2 is its phase change around 68 °C, we used a heating chip that enables us to set a precise temperature during the TEM measurements by running calibrated current through metallic contacts causing Joule heating of SiC block.

The heating chip we used was a Fusion Thermal E-chip with a continuous silicon nitride (Si_3N_4) coating from Protochips Fusion Select series [106]. The SEM image of this heating chip is shown in Figure 2.12 **(a)**. The precise control over the temperature (up to 1 200 °C) can be achieved only between the contacts in a so called active area, which is shown in detail in Figure 2.12 **(b)**. Figure 2.12 **(c)** shows a detail of the active area with 9 holes with a diameter of 8 µm in an array 3×3.

The experiment was designed in such a way that we would place a lamella over one of the holes. Since the active area was coated with a silicon nitride layer[10], the first thing we did was remove this coating from one of the holes with FIB. The reason for doing this was to remove any unnecessary background signal during the TEM measurements so that we could measure the VO_2 directly against vacuum. For this task, we chose the bottom right hole. Then we used GIS to deposit a wall made of Pt that was placed 2 µm to the right from the hole. This Pt wall is shown as an inset in Figure 2.12 **(c)** and is $10 \times 3\,\mu m^2$ with height 10 µm. The immensely useful implication from the fabrication of this wall will be evident in the coming text.

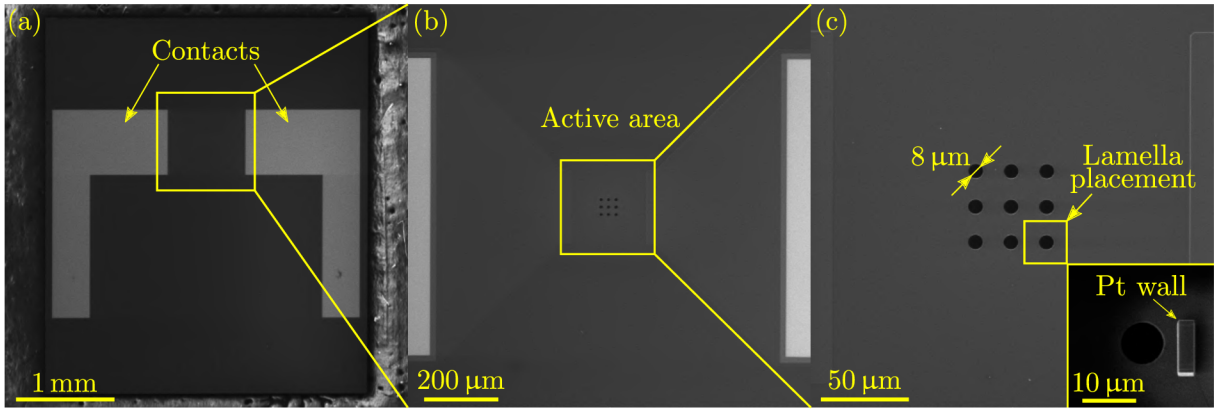

Figure 2.12: **(a)** SEM image of the heating chip. **(b)** Detail of the area between the contacts, where we can set a precise temperature – active area. **(c)** Detail of the active area with 9 holes with 8 µm diameter. We used the bottom right hole for the placement of the lamella. Inset shows the Pt wall next to the bottom right hole, which is $10 \times 3\,\mu m^2$ with height ≈ 10 µm.

Preparation of the lamella for the heating chip is vastly different from the preparation of the lamella meant to be placed on a Cu grid. The following differences are schematically illustrated in Figures 2.13 **(a)** and **(b)**, where **(a)** shows the lamella for a Cu grid and **(b)** shows the lamella for a heating chip.

[9] A cryogenic TEM sample holder does theoretically allow heating of the sample up to 100 °C, but the heat transfer to the lamella is uncertain and the temperature of the lamella can not be precisely measured. Therefore, achieving the phase change of VO_2 at 68 °C is not guaranteed.

[10] The coating over the holes is not visible in this picture.

1. The first difference is in its size. Typical dimensions of a lamella for a Cu grid is 7×5 µm, but the hole in the heating chip is 8 µm. The height of the lamella (5 µm) is not that important (the VO_2 layer is ≈ 550 nm), but we need to increase its width from the 7 µm to ensure it does not fall into the hole. The final width of the lamella was 12 µm. This brings us complication number one: The bigger the lamella, the longer time it takes to create it with FIB.
2. The second difference is in its shape. We decided to make the lamella in the shape of a letter "U", where the thin part of the lamella meant for TEM characterization is enclosed with a robust frame. This frame will be important during the attachment to the heating chip to ensure that the thin part in which we are interested remains intact. Complication number two: With increasing size and weight of the lamella, the connection between the tip of the nanomanipulator and the Pt protective layer on top of the lamella experiences bigger strain and is easier for the lamella to fall from the tip.
3. The third difference is in the fabrication of the thin area for TEM characterization. In the case of the lamella for a Cu grid, we prepared a 2 µm thick lamella, transferred it *as is* to the Cu grid, and then we thinned the *whole* lamella down (top to bottom). Here, the "U" frame layout forced us to mill to only a certain depth to ensure that the bottom frame still remains thick enough to support both sides of the frame. Complication number three: It is hard to predict the depth of milling at different ion beam currents, that are needed for thinning down the lamella at different thinning stages (see Section 2.2.1).

The final lamella prepared with these differences is shown in Figure 2.13 **(c)**. Figure 2.13 **(d)** shows a top view of the lamella with highlighted thinning steps 1–4, where 1 is the thickest (≈ 400 nm) and 4 is the thinnest (≈ 150 nm). We proceeded with the lift-out of the lamella, where we used more Pt to weld the lamella to the nanomanipulator to ensure a solid connection, which was needed during the following manipulation.

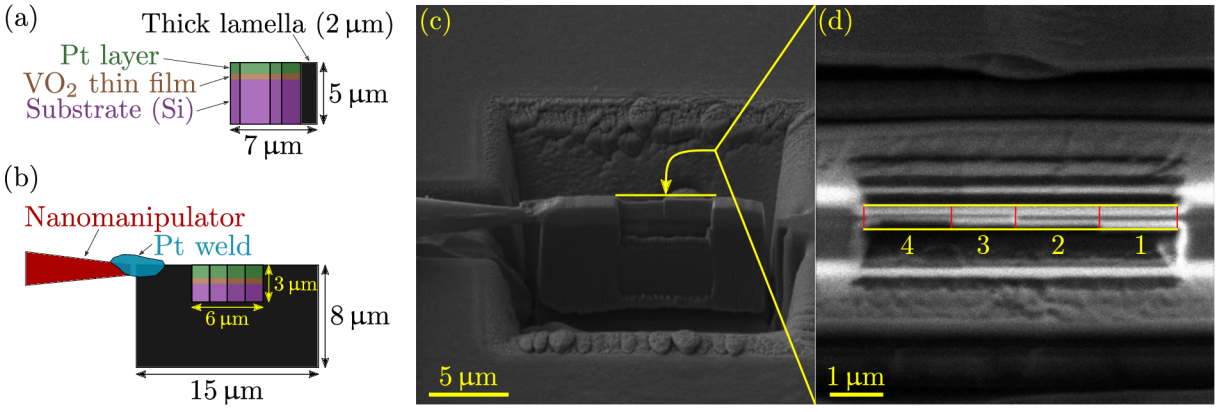

Figure 2.13: **(a)** Schematic of the lamella for a Cu grid. **(b)** Schematic of the lamella for a heating chip. **(c)** Lift-out of the final lamella after thinning. **(d)** Top-view detail of the thinned part of the lamella with highlighted thinning steps 1–4 from thicker (≈ 400 nm) to thinner (≈ 150 nm).

Apart from the three differences in the lamella preparation mentioned earlier, there was another significant complication during the lamella transfer to the heating chip: we needed the lamella to be tilted to a different angle than it was after the fabrication. This complication was not present during the lamella transfer to the Cu grid: After fabrication,

the lamella was at 35° and we attached it to the Cu grid that was also tilted to 35°. Therefore, since we needed a different tilt of the lamella and the nanomanipulator can not be rotated, we had to use a workaround solution that is schematically illustrated in Figure 2.14.

In this arrangement, we used a Cu grid as an intermediary step before putting the lamella on the heating chip. Figure 2.14 **(a)** shows the microscope arrangement after lamella fabrication, where the electrons come from the top (90°), and since the relative angle between SEM and FIB is 55°[11], the ions come at an angle 35°. We then attached the lamella to the nanomanipulator, moved it to a Cu grid that was at 90° tilt, and detached the nanomanipulator. This is shown in Figure 2.14 **(b)**. Then, we tilted the Cu grid to 40° along with the lamella, so that the lamella was now at −15°, which is shown in Figure 2.14 **(c)**. Then again, we attached the lamella to the nanomanipulator, detached it from the Cu grid, and moved it to a heating chip that was tilted to −30°. This is shown in Figure 2.14 **(d)**.

With this cumbersome transfer approach, we were able to achieve a relative angle 15° between the lamella and the heating chip. The reason why we could not just tilt the heating chip to 35° to align with the lamella was that in such a position, we would be unable to insert the GIS nozzle – see the microscope chamber view in Figure 2.5 **(b)**. Therefore, attachment of the lamella to the heating chip would not be possible at all. Moreover, the tilt of the heating chip −30° (instead of more suitable −15°) was chosen for a similar reason: a less dangerous approach with GIS to the region of interest on the heating chip.

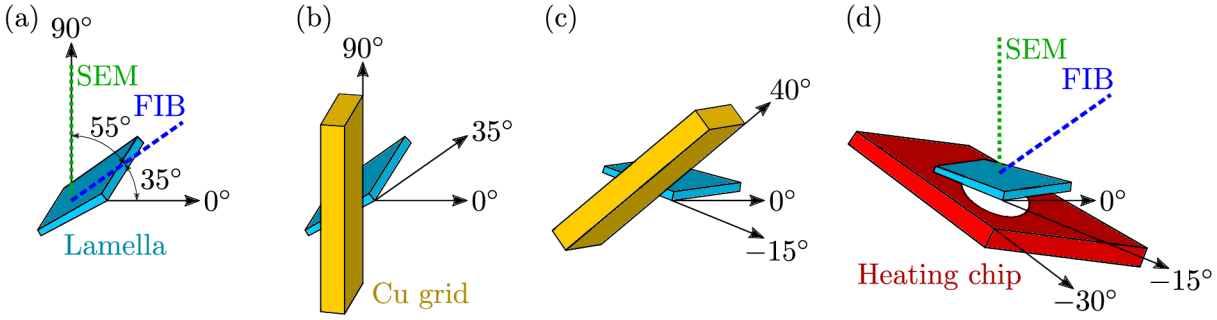

Figure 2.14: Lamella transfer from the sample to the heating chip. **(a)** Lamella fabrication at 35°. **(b)** Lamella at 35° attached to the Cu grid at 90°. **(c)** Cu grid rotated to 40°, lamella is now at −15°. **(d)** Lamella at −15° attached to the heating chip at −30°. The relative angle between the lamella and the heating chip is 15°.

The placement of the lamella on the heating chip turned out to be yet another significant complication: Given all of the preceding fabrication steps and transfer procedures that took hours of consistent work, the attachment of the lamella to the heating chip was the most critical step in this process.

The use of FIB at low currents for imaging during the movement of the nanomanipulator to observe its movement in 3D was discussed in Section 2.2.1 and shown in Figure 2.7 **(b)**. Here, the situation is similar: We use FIB imaging to estimate the dis-

[11] When we described the lamella fabrication process in Section 2.2.1, we explained that the *stage* was tilted to 55° and therefore FIB was perpendicular to the sample surface. This notation was in agreement with the microscope software. However, here we will describe the tilt of the lamella (not the stage) with respect to the horizontal 0°. Therefore, the *lamella* was at 35° tilt during the fabrication process.

tance between the lamella on the nanomanipulator and the surface of the heating chip. This is shown in Figure 2.15, where we approach the bottom right hole with a Pt wall on the right side that was prepared previously. Images **(a)** (SEM) and **(b)** (FIB) were taken at the same time. We can use the SEM image to navigate to the correct position in x and y on the heating chip, however, we need the FIB image to estimate the z distance. To illustrate this, images **(c)** (SEM) and **(d)** (FIB) are again taken at the same time. Here, we adjusted the xy position in the SEM image and could tell how close we are to the heating chip thanks to the FIB image.

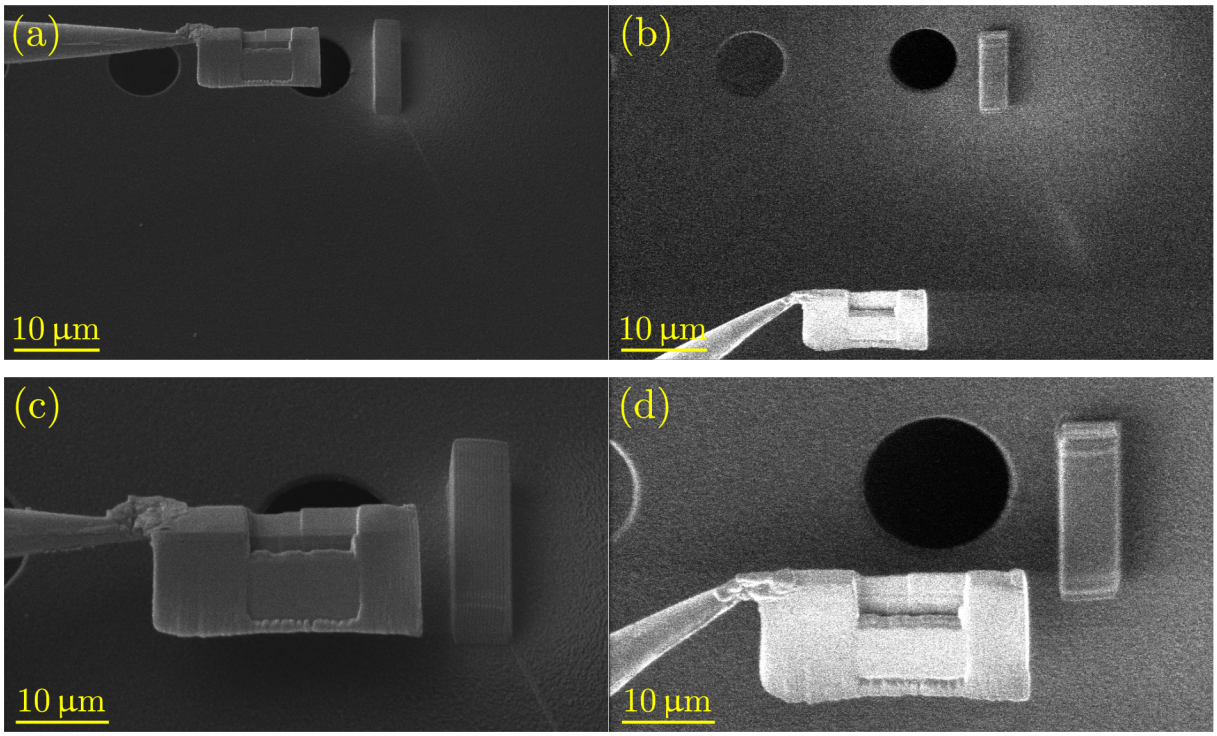

Figure 2.15: Lamella approach to the heating chip. SEM **(a)** and FIB **(b)** images taken at the same time. After some xy adjustments, SEM **(c)** and FIB **(d)** images are taken again at the same time. Note that in these pictures, the silicon nitride (Si_3N_4) coating on the left hole is clearly visible.

Estimating the distance between the lamella and the heating chip with the FIB image is not precise. We risk hitting the surface during the movement very close to the surface. If that were to happen, the Pt weld between the lamella and the nanomanipulator would break and the lamella would be lost[12]. To counter this problem, we used the previously fabricated Pt wall (height $\approx 10\,\mu m$) to attach the lamella to it in a similar way we attached the lamella to the Cu grid from the side. This attachment can be seen in Figure 2.16 **(a)**. After the connection was secured, we detached the nanomanipulator and also attached the left side of the lamella to the heating chip. The lamella attached to the heating chip is shown in Figure 2.16 **(b)**. It is an SEM image with the surface of the heating chip perpendicular to FIB (this means that the surface normal is tilted to 35°) to show a 3D view of the result. Figure 2.16 **(c)** then shows also an SEM image, but now the surface of

[12]Contrary to common sense, the lamella would not "fall down" on the heating chip – because of the low mass of the lamella, the gravity in the microworld is not that strong. The lamella would rather be "blown away" due to different charges of the lamella and the heating chip. Unfortunately, this behavior has been observed on the predecessors of the lamella discussed here.

the heating chip is perpendicular to SEM (surface normal is tilted to 90°). In this image, we can see that the VO_2 thin film is actually above the hole, exactly like we planned.

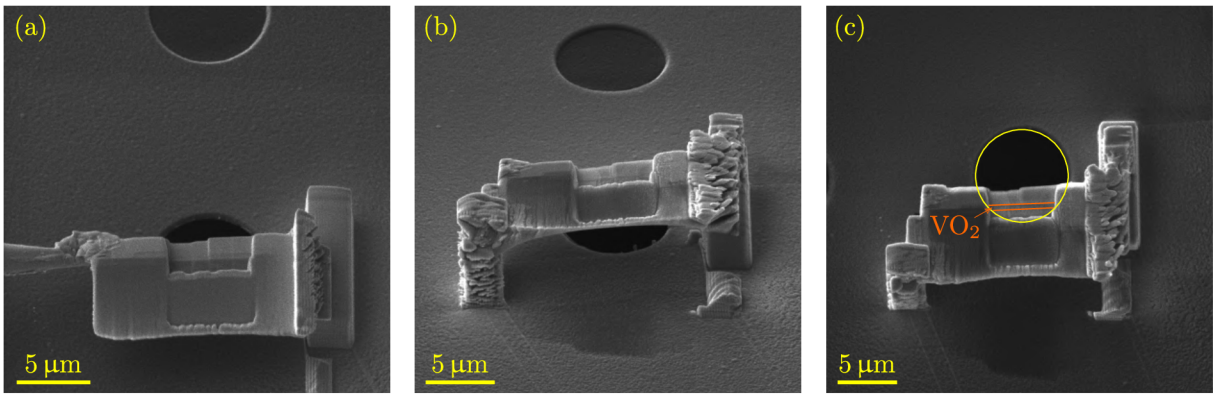

Figure 2.16: SEM images of the lamella placement above the hole in the heating chip. **(a)** Welding lamella to the Pt block. **(b)** Lamella on the heating chip (stage tilt 55°). **(c)** Lamella on the heating chip (stage tilt 0°, perpendicular to SEM). The VO_2 layer is above the hole.

Before the lamella on the heating chip was prepared for TEM characterization, we needed to proceed with one last fabrication step: removal of the Pt protective layer and thinning of the VO_2 thin film. Figure 2.17 **(a)** shows a detail of the thin area above the hole. We removed the top Pt protective layer with FIB from the thinner left part and created a rectangle-shaped hole down to a VO_2 thin film, which is shown in Figure 2.17 **(b)**. Then we tilted the lamella to 35° (facing FIB) and we proceeded with imaging at low voltage (5 kV) and low current (40 pA). Although it is just imaging, the sample still takes damage from FIB. Therefore, we continued imaging for approximately 25 seconds until we successfully thinned the VO_2 layer down, which is shown in Figure 2.17 **(c)**. The thinned part we focused on during subsequent measurements is marked with an arrow. After this final step, the goal of putting a lamella on a TEM heating chip was successfully achieved, and we could proceed with its characterization in a transmission electron microscope.

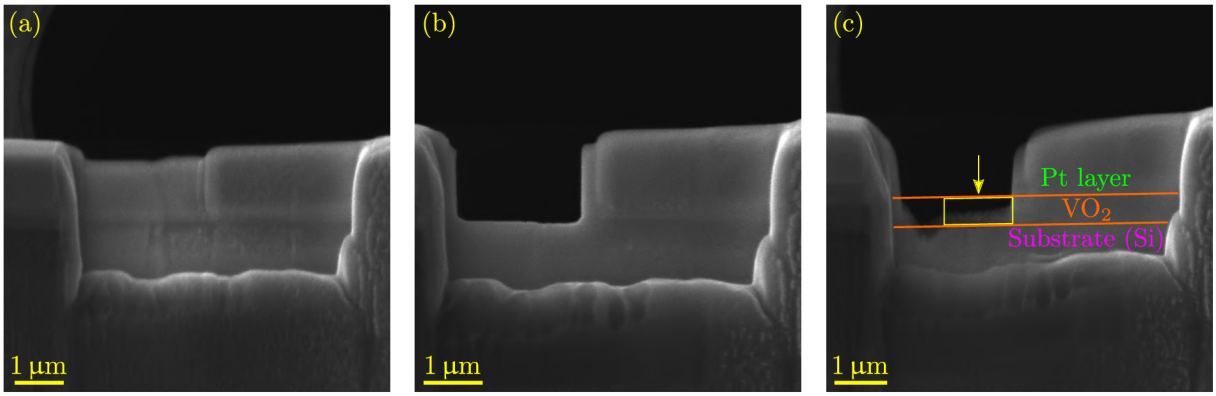

Figure 2.17: **(a)** Detail of the thin area above the hole. **(b)** Removal of the Pt protective layer from a thinner part of the lamella. **(c)** Low voltage thinning of the VO_2 layer. An arrow marks the region of interest during the subsequent measurements.

3 Transmission electron microscopy

This chapter is dedicated to the characterization of the fabricated samples described in the previous Chapter in Section 2.3. The microscope used for the characterization is located in the structural analysis laboratory (class 100 000 cleanrooms) at CEITEC Nano and is shown in Figure 3.1 **(a)** [107]. All measurements were made by an operator of the microscope Ing. Michal Horák, Ph.D., but analysed within the scope of this Thesis.

A schematic illustration in Figure 3.1 **(b)** shows the interaction of an electron beam with a sample. During the fabrication of our samples in the previous Chapter in Section 2.3 we used secondary electrons for imaging in SEM, while backscattered electrons could be detected and used for imaging as well.

Electrons that are transmitted through the sample are important for another type of electron microscope, the transmission electron microscope (TEM). In these microscopes, the *elastically* scattered electrons create a dark-field (DF) image, and the *unscattered* electrons create a bright-field (BF) image. Furthermore, *inelastically* scattered electrons can be used to analyse the optical and chemical properties of samples by using electron energy-loss spectroscopy (EELS).

For the characterization of our samples we also used high-energy photons (X-rays) emitted from the sample after electron beam irradiation. Such signal can be used to obtain a basic chemical analysis using the energy-dispersive X-ray spectroscopy (EDXS[1]) [108].

We will start this Chapter by describing the two working modes of the microscope – TEM and STEM (Section 3.1). Then, we will describe measurements by electron energy-loss spectroscopy (EELS) and how both low-loss EELS and core-loss EELS can be used to investigate VO_2 (Section 3.2). After that, the rest of this Chapter will be dedicated to the description of the results of our measurements (Section 3.3).

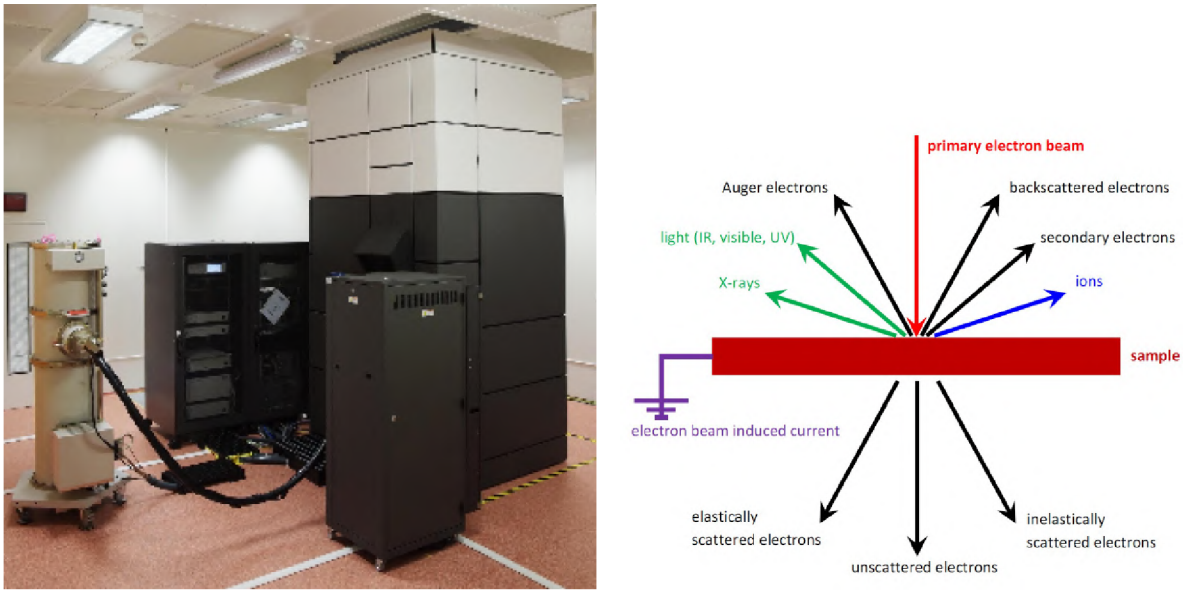

Figure 3.1: **(a)** Transmission electron microscope Titan at CEITEC, adapted from [107]. **(b)** Scheme illustrating the interaction of high-energy electron beam with thin sample, adapted from [109].

[1] Other abbreviations commonly used for this technique in the scientific community are EDX and EDS.

3.1 Modes of operation – TEM, STEM

A modern transmission electron microscope (TEM) can be typically operated in two modes: a transmission mode (TEM) and a scanning transmission mode (STEM). In the case of TEM, the sample is illuminated by a parallel electron beam (plane wave). In STEM, it is illuminated by a focused electron beam that is scanned point by point across the sample. A simplified sketch of both modes is illustrated in Figure 3.2.

For the creation of an image in TEM we can use either all transmitted electrons, or filter out inelastically scattered electrons (by inserting an objective aperture) to create a bright-field (BF) image with higher contrast. The third possibility is to detect only inelastically scattered electrons to form a dark-field (DF) image.

Imaging with STEM can be done by using three detectors: A bright-field (BF) detector collects unscattered electrons, an annular dark-field (ADF) detector collects mostly elastically scattered electrons, and a high-angle annular dark-field (HAADF) detector collects electrons inelastically scattered at higher angles. HAADF imaging is highly sensitive to variations in the atomic number (Z) of atoms in the sample and is therefore also called Z-contrast imaging.

For more detailed information on TEM in general, I refer to the book *Transmission electron microscopy* by D. B. Williams and C. B. Carter (2009) [108].

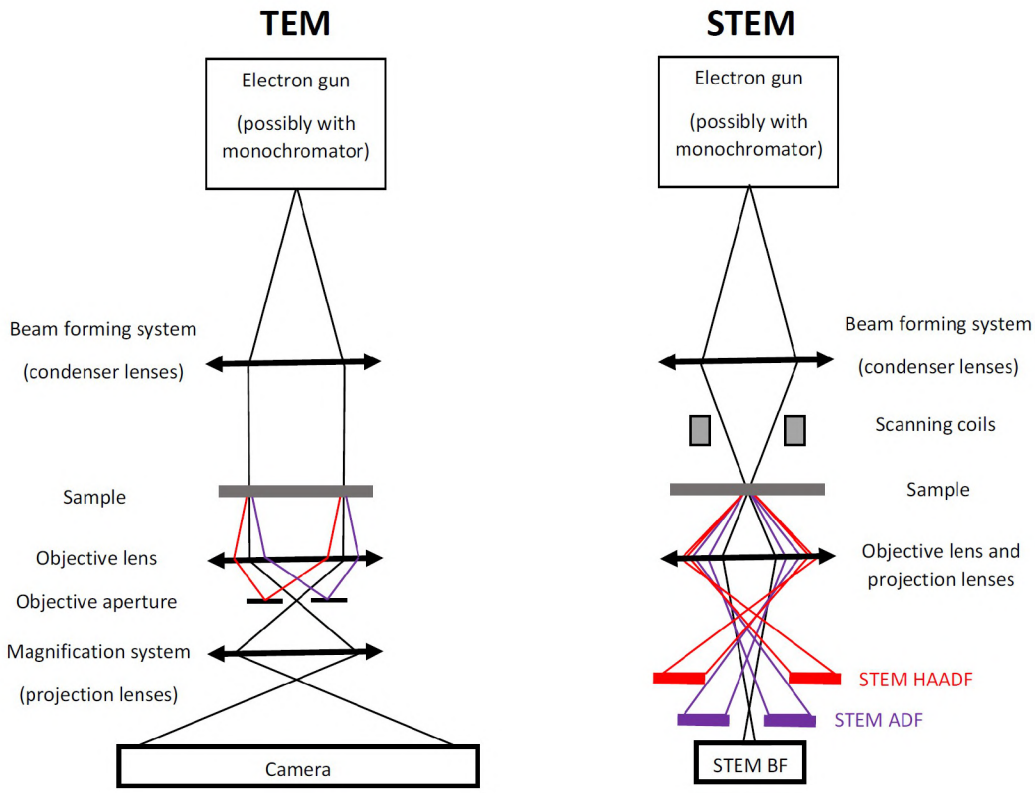

Figure 3.2: A simplified schematic sketch of TEM and STEM modes of a transmission electron microscope. In TEM, the sample is illuminated by a parallel electron beam and the elastically scattered electrons can be filtered out by an objective aperture. In STEM, the illumination is done by a focused electron beam that scans the sample point by point and three detectors are used to collect the electrons at different angles. Adapted from [109].

3.2 Electron energy-loss spectroscopy (EELS)

In electron energy-loss spectroscopy (EELS), the transmitted electron beam is collected by a high-resolution electron spectrometer, which separates the electrons based on their energy. The resulting electron energy-loss spectrum shows the number of electrons (intensity) as a function of the decrease of their kinetic energy (energy loss). The peaks in the spectrum represent a fine structure that reflects the crystallographic or energy band structure of the specimen [110]. However, for EELS measurement, very thin samples (below 100 nm) are needed in order to obtain information about the internal structure of the sample.

The main feature of an EEL spectrum is the zero-loss peak (ZLP) that consist of electrons transmitted through the sample without measurable energy loss. This includes both elastically scattered electrons and unscattered electrons. Typically, the signal of inelastically scattered electrons is superimposed onto the tail of the ZLP. Therefore, removal of the ZLP from the EEL spectra is very important and various methods producing reliable results have been developed [111].

EELS has been used to characterize composition and properties of materials in TEM since 1944 [112] and the first EELS attachment to an SEM (in transmission mode) was reported in 2003 [113]. EELS is nowadays widely used for applications in both TEM [110] and SEM [114].

There are two characteristic parts of an EEL spectrum: The low-loss part and the core-loss part, where the division between them was arbitrarily established at $\approx 50\,\mathrm{eV}$ [115]. For more detailed information on EEL spectra in general, I refer to the book *Electron energy-loss spectroscopy in the electron microscope* by R. F. Egerton (2011) [110].

3.2.1 Low-loss EELS

The low-loss part of an EEL spectrum can contain information on volume and surface plasmons, interband and intraband transitions, localized surface plasmon modes, radiation losses (Cherenkov radiation[2]), and phonons [110].

At the time of writing this Thesis, simulations of low-loss EEL spectra of VO_2 thin films were done in the Bachelor's Thesis of Jiří Kabát, a student at the Author's University. Figure 3.3 shows EEL spectra for varying thickness of the VO_2 thin film below **(a)** and above **(b)** the metal-to-insulator (MIT) transition temperature. With increasing thickness increases the electron energy-loss probability. This could be the result of higher absorption and more effective excitation of optical modes.

In the dielectric phase **(a)**, the intensity of the peak corresponding to the excitation of phonon polaritons at energies below 100 meV increases with the sample thickness. Similarly, the intensity of the peak at 1.8 eV corresponding to material absorption also increases with thickness, and its profile becomes more pronounced.

In the metallic phase **(b)**, the peak corresponding to the excitation of volume and surface plasmons shifts toward higher energies (around 1.22 eV) for thicker films and its intensity again increases with sample thickness.

[2]Named after Soviet physicist Pavel Cherenkov who first reported it in 1934 [116]. Photons of light are emitted when a charged particle passes through a dielectric medium (liquid or solid) at a speed greater than the velocity of light in that medium. A classic example would be the characteristic blue glow of a nuclear reactor.

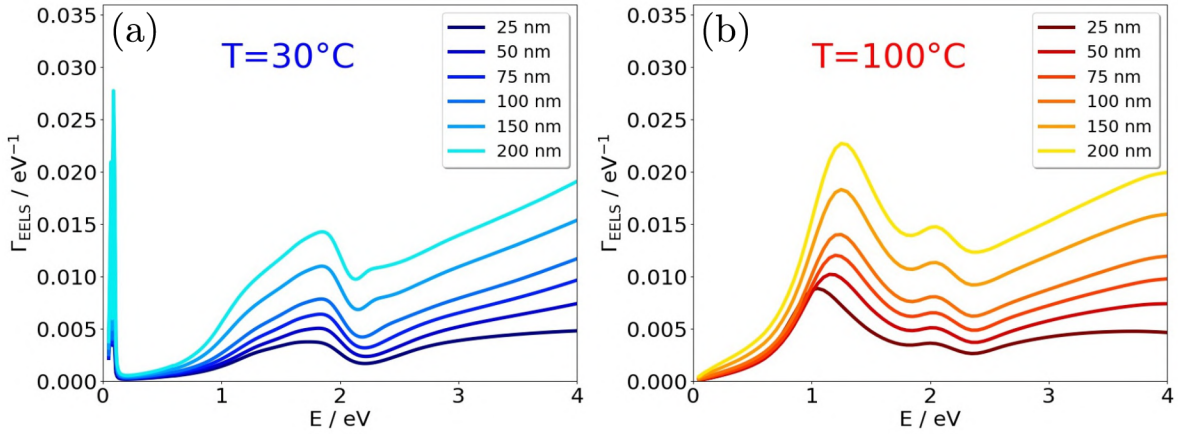

Figure 3.3: Low-loss EEL spectra for VO_2 thin film in dielectric **(a)** and metallic **(b)** phases. The varying parameter is the thickness of the thin film. The zero-loss peak (at 0 eV) is not included in these graphs. Adapted from [117].

3.2.2 Core-loss EELS

The core-loss part of an EEL spectrum contains information on the material edges – the specific absorption edges of each chemical element. The peaks in the spectrum hold information on both qualitative (their position) and quantitative (their intensity) chemical analysis. Moreover, the core-loss part allows the study of the oxidation states and chemical bonding of the sample. However, an accurate subtraction of a background that arises from the excitation of electrons of lower binding energies is needed for correct interpretation of the core-loss fine structure and elemental analysis [110].

A typical core-loss EEL spectrum of VO_2 is shown in Figure 3.4. Two major peaks correspond to vanadium edges: On the left is a V-L_3 peak, and on the right is a V-L_2 peak. On the right side of the vanadium peaks is the oxygen peak corresponding to the O-K edge. A characteristic pre-peak in O-K edge (marked with an arrow) was shown to change in intensity for different stoichiometries of VO_2 [118].

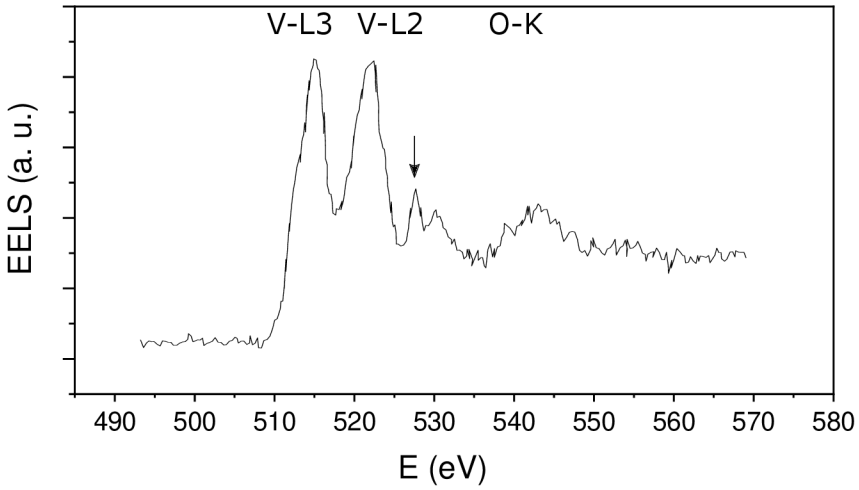

Figure 3.4: A typical core-loss EEL spectrum of VO_2. Arrow marks a characteristic pre-peak for differentiating between V_xO_y stoichiometries. Data taken from [119].

A change in VO_2 stoichiometry of a thin region at both the surface and interface was reported in 2014 by Xiaoyan Li et al. [119]. In the paper, they measured VO_2 thin films

grown on SiO_x/Si substrate, characterized it by EELS, and found transitional regions 2–3 nm thick, where the vanadium valence changes from VO in the outermost parts, to V_2O_3 further from the surface/interface, to VO_2 in bulk. This is schematically illustrated in a chemical profile of a thin film in Figure 3.5.

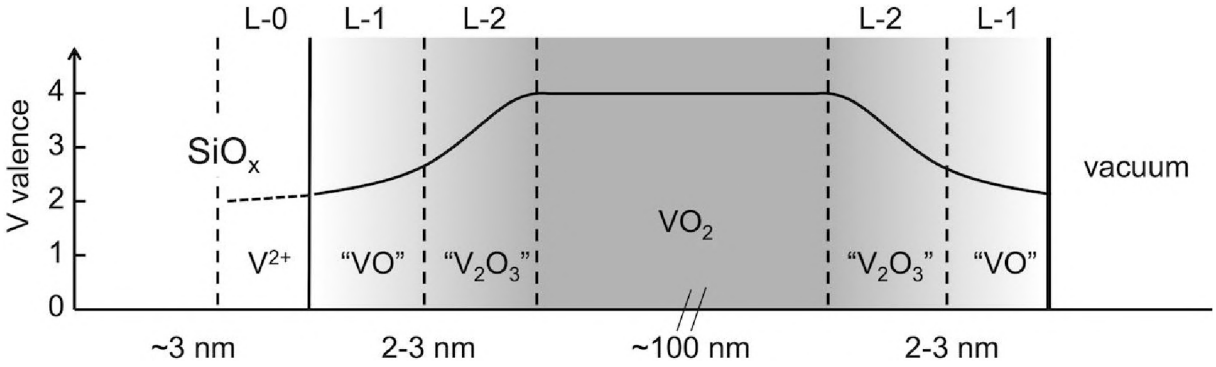

Figure 3.5: Chemistry scheme for the VO_2 thin film on SiO_x/Si. Adapted from [119].

Their results of the surface measurement (material–vacuum) are relevant for our experiments. Figure 3.6 shows EEL spectrum imaging across the surface, where three distinct areas corresponding to different V_xO_y stoichiometries are measured. The increase in intensity of the O-K pre-peak (marked with red triangles) is an indicator of the changing stoichiometry. The second important discovery is a shift of the first V-L_3 peak towards higher energies. The shift gradually increases from VO, to V_2O_3, to VO_2. Furthermore, a clear "shoulder" (marked with a blue triangle) is visible on the V-L_3 peak for the VO_2 phase. Our measured data will be compared to these results in the Section 3.3.4.

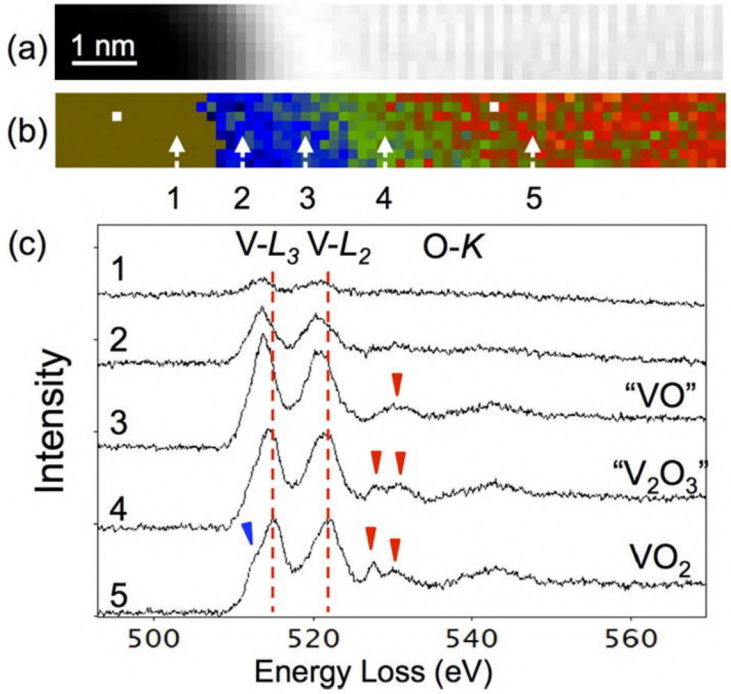

Figure 3.6: EEL spectrum imaging across the surface. **(a)** HAADF image of the surface area. **(b)** EELS energy shift maps for the position of the V-L_3 peak. The peak position of VO_2 is set as standard. **(c)** EEL spectra positions marked in the energy shift maps. Adapted from [119].

3.3 Results

The rest of this chapter is dedicated to the characterization of the fabricated samples in a transmission electron microscope. The fabrication of these samples was described in the previous Chapter in Section 2.3. During this characterization, we focused mainly on high-resolution (HR) imaging and electron energy-loss spectroscopy (EELS). Supplementary information on the components of the samples was obtained by energy-dispersive X-ray spectroscopy (EDXS). The acceleration voltage during the TEM measurements was 300 kV. This Section is again divided into 3 parts where we characterize the 3 fabricated samples:

1. VO_2 powder (EDXS, HR imaging).
2. Lamella on a TEM Cu grid (EDXS, HR imaging).
3. Lamella on a TEM heating chip (HR imaging, EELS).

3.3.1 VO_2 powder

The fabrication of this sample was described in Section 2.3.1. For the characterization of the powder pieces, we focused mainly on the previously discussed "paw" structure.

EDXS

The "paw" structure is shown in an HAADF image in Figure 3.7 **(a)**. Figure 3.7 **(b)** shows the HAADF image combined with an EDXS image, which gives us information about the chemical composition. We can see that the "paw" structure is made of a combination of V (yellow) and O (red) and lies on the webbing made of C (green). These pictures were taken at the beginning of our measurements.

The other two images in Figure 3.7 also show a HAADF image **(c)** and a HAADF image combined with an EDXS image **(d)**. The main[3] difference between the upper and lower pair of images is that the lower images were taken towards the end of our measurements. We can clearly see that the "paw" structure has been damaged during high-resolution imaging. The most damaged areas are marked with arrows, where we can see not only C contamination in the EDXS image, but also a bending of the middle tip (or finger) in the HAADF image. From this we concluded that exhaustive imaging with electrons is devastating for our VO_2 samples.

HR imaging

Figure 3.8 **(a)** shows a bright-field image of the "paw" structure with the highlighted area shown in detail in Figure 3.8 **(b)**. We then took a high-resolution image of the highlighted area, which is shown in Figure 3.8 **(c)**. Here, we chose an exemplary area of the HR image that is shown in detail in Figure 3.9 **(a)**. We then proceeded with fast fourier transform (FFT) of the selected image area which is shown in Figure 3.9 **(b)**. A magnified FFT image with a few marked spots corresponding to discrete spatial frequencies in k-space[4]

[3]The other difference would be a different contrast in the HAADF image **(c)** and a slightly worse resolution of the EDXS image **(d)** due to different acquisition conditions.

[4]Fourier transform of the spatial function of a real-space lattice is represented by spatial frequencies or wavevectors of plane waves of a reciprocal lattice and visualized in a reciprocal space, also called k-space.

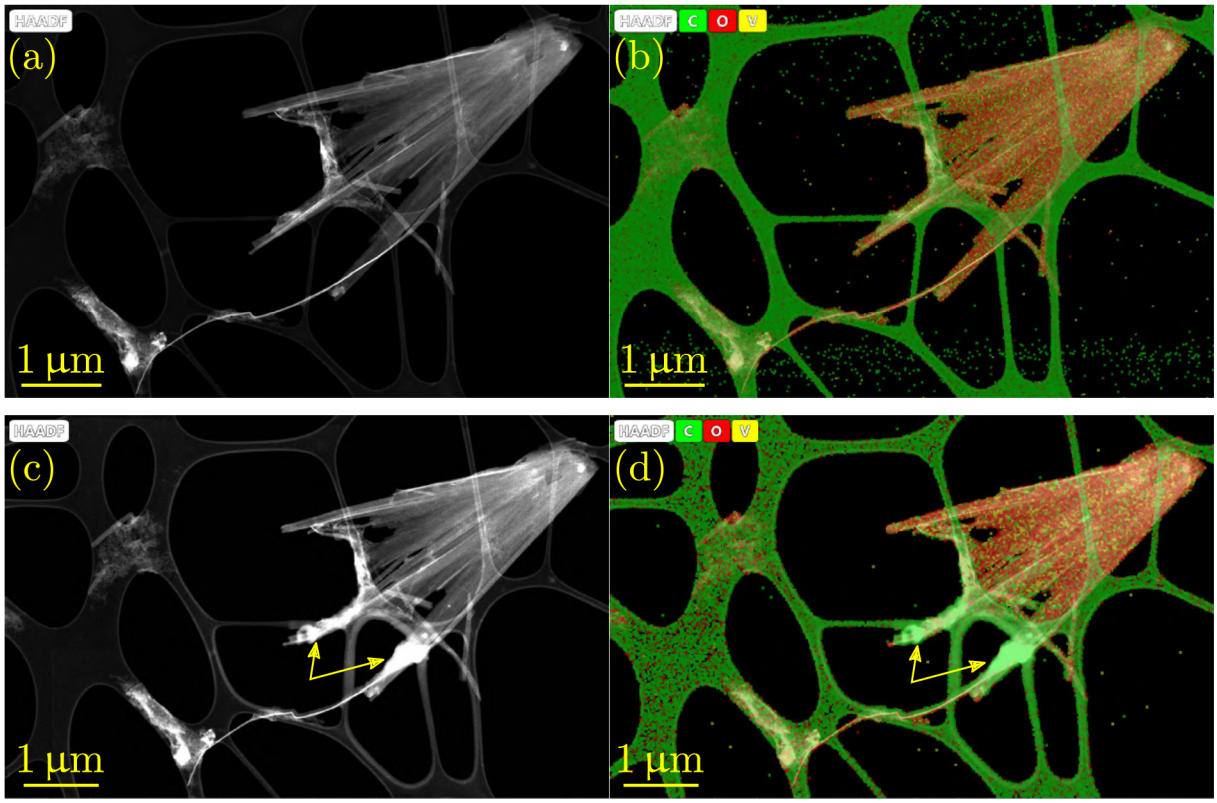

Figure 3.7: Examined "paw" structure. **(a)** HAADF and **(b)** EDXS images before measurements. **(c)** HAADF and **(d)** EDXS images after measurements. The damaged areas are marked with arrows.

is then shown in Figure 3.9 **(c)**. From these positions in k-space we calculated some of the distances between atoms in real space in the specified area: 1.38 Å, 1.58 Å, 1.93 Å, 2.49 Å, 2.79 Å, 3.36 Å, 3.59 Å, 5.57 Å. Further analysis of these acquired distances was not conducted due to the lack of a simulation of the crystal and a diffraction pattern.

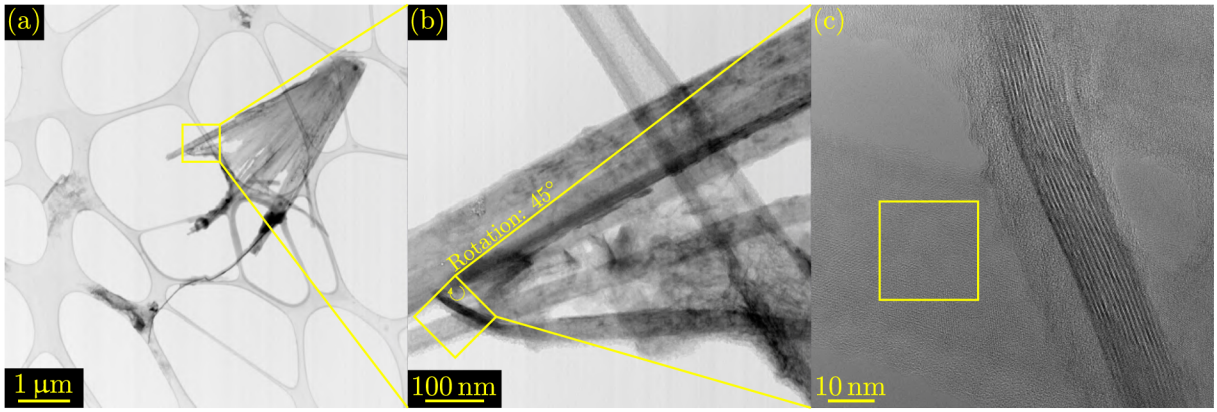

Figure 3.8: **(a)** BF image of the "paw" structure. **(b)** Detail of the top "finger". **(c)** High-resolution image (rotated by 45°) with highlighted position for the following FFT analysis.

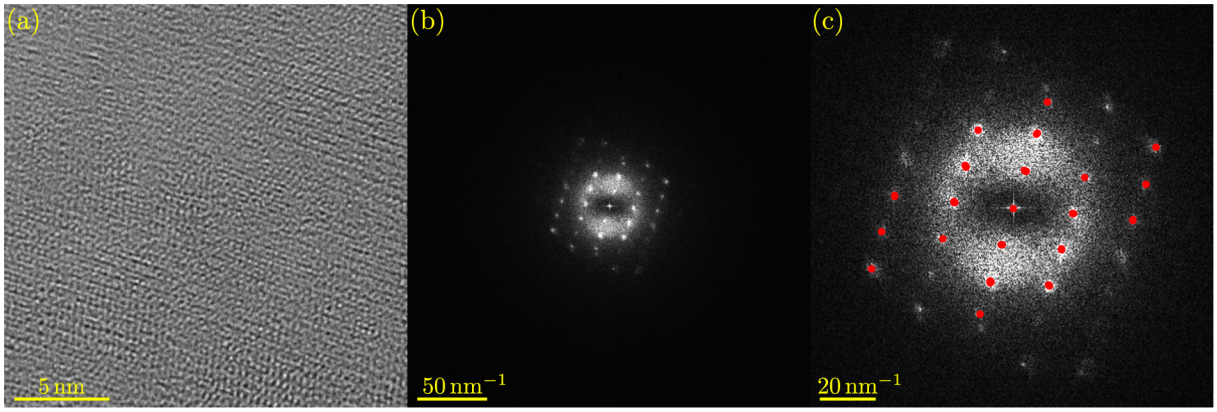

Figure 3.9: **(a)** Detail of the area highlighted in Figure 3.8 (c). **(b)** FFT of the whole area. **(c)** A magnified FFT image with a few marked spots corresponding to discrete spatial frequencies (red dots) in k-space.

3.3.2 VO_2 thin film – lamella on a TEM Cu grid

The fabrication of the lamella on a Cu grid was described in Section 2.3.2. The overview image of the lamella in the transmission electron microscope is shown in Figure 3.10 **(a)**. In comparison with the SEM image during its fabrication, the lamella during TEM characterization was upside down, i.e., rotated by 180°.

EDXS

Figure 3.10 **(b)** shows a HAADF image of the detail of the VO_2 layer, where it is apparent that the VO_2 layer obtained by evaporation is a porous rather than uniform material. Figure 3.10 **(c)** then shows the same image combined with an EDXS measurement. In this image, we can confirm that the lamella is upside down: Si substrate (purple) is at the top and the protective layer made of Pt (light blue) mixed with C (green) and Ga (dark blue) is at the bottom. The middle layer is composed of V (yellow) and O (red).

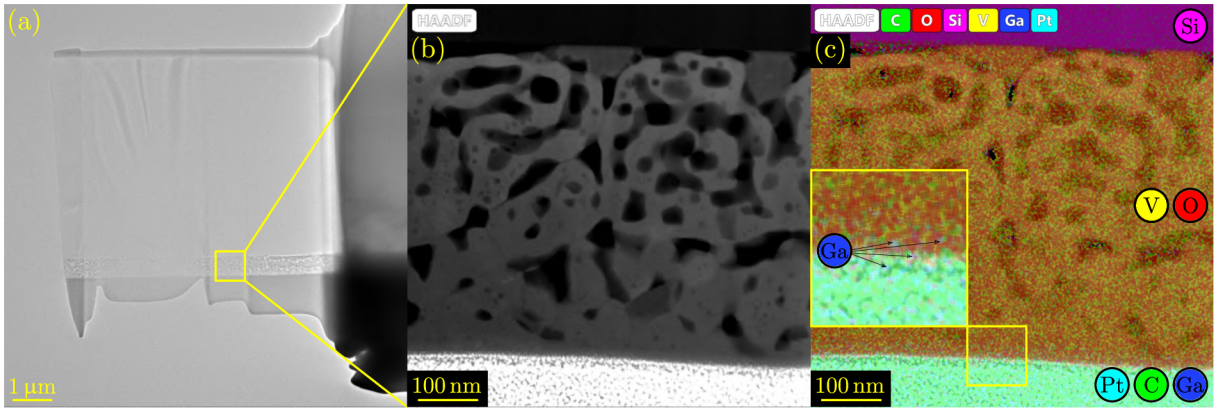

Figure 3.10: **(a)** Lamella on a Cu grid in TEM. **(b)** HAADF image of the highlighted detail of the VO_2 layer, where its porous character is apparent. **(c)** HAADF image combined with the EDXS image of the lamella components. Inset shows Ga implantation in the VO_2 layer at the interface between the VO_2 layer and the protective layer.

The presence of carbon in the composition of the protective layer may be a little unexpected, but can be explained if we look closely at the precursor for the deposition of Pt:

It is an organometallic precursor gas $MeCpPt^{IV}(Me)_3$ called trimethyl(methylcyclopentadienyl)platinum(IV) with linear formula $C_5H_4CH_3Pt(CH_3)_3$ [120]. This precursor has been used for FIBID since the early 1990s and gives the resulting film comprising Pt with a contamination of C, Ga, and a very small amount of O [121, 122]. We are interested in the atomic concentration of the deposited material in the dual-beam microscope LYRA3 that was used for the preparation of samples in this Thesis. The atomic concentration was measured by Ing. Tomáš Šamořil, Ph.D. in his Doctoral Thesis for ion beam energy 30 keV and current 400 pA as follows: $28.6 \pm 0.7\,\%$ Pt, $52.8 \pm 7.0\,\%$ C, $17.2 \pm 0,4\,\%$ Ga, $1.3 \pm 0,4\,\%$ O [123]. Therefore, roughly half of the deposited protective layer is made of C, and only a little more than quarter is made of the desired Pt – hence the prevailing green/light blue color of the protective layer in Figure 3.10 **(c)**.

In addition to Ga being present in the protective layer, it is also occasionally scattered throughout the sample surface as a consequence of fabrication of the lamella with Ga ions, even though the final polishing was done at low voltage to minimize this phenomena. Furthermore, during the fabrication of this lamella, we did not make a thin FEBID layer (with electrons) on the surface of the VO_2 thin film before creating a thick protective FIBID layer (with ions). As a result, Ga was implanted a few nanometers into the VO_2 thin film and it can therefore be spotted at the interface between the lower protective layer and the middle VO_2 layer, which is to some extent visible in the inset of Figure 3.10 **(c)**. This slight imperfection was later corrected during the fabrication of the lamella for a TEM heating chip, where we used a thin FEBID layer before creating a thick FIBID layer to avoid Ga implantation into the VO_2 thin film.

HR imaging

After the initial characterization of the chemical components of the lamella, we proceeded with the high-resolution imaging of the thinnest part of the lamella. Similar to the case with the "paw" structure, this extensive imaging caused damage to the VO_2 layer, which can be seen as darker areas in Figure 3.11 **(a)**. One such high-resolution image of a VO_2 "bridge" between two holes is shown in detail in Figure 3.11 **(b)**. We then advanced to the characterization of the highlighted area that is shown in detail in Figure 3.11 **(c)**. FFT of this area is shown in Figure 3.12 **(a)**, where two distinct spots corresponding to discrete spatial frequencies are marked. Then we used these two spots (along with the central spot) in Figure 3.12 **(b)** to perform the inverse FFT. This produces a noise-filtered image shown in Figure 3.12 **(c)**. The fringe pattern corresponds to the striped pattern visible in Figure 3.11 **(c)**. From this image, we were able to obtain the distance between atoms in this area as 2.02 Å.

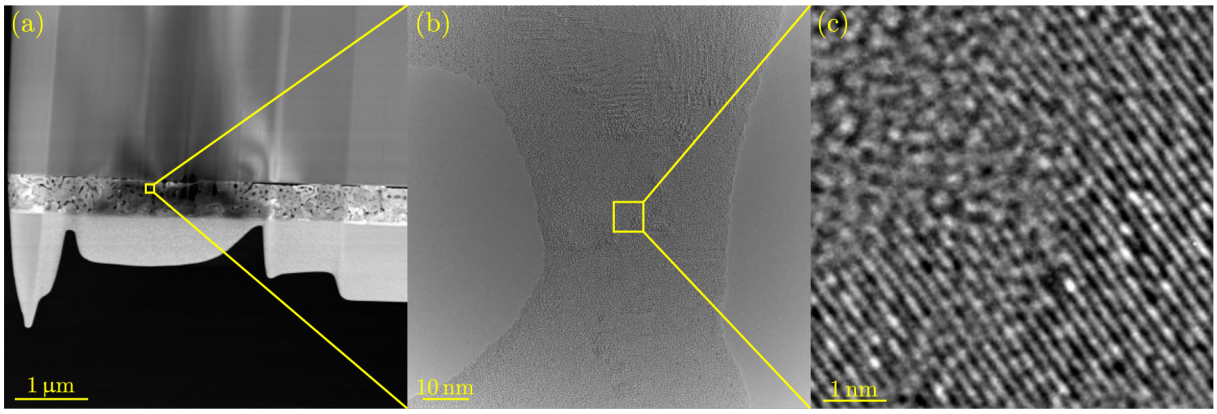

Figure 3.11: **(a)** HAADF image of the lamella in TEM with visible contamination after multiple high-resolution imaging (darker areas). **(b)** HR image of the VO_2 "bridge" between two holes in the VO_2 layer. **(c)** Detail of the HR image used for the following FFT analysis.

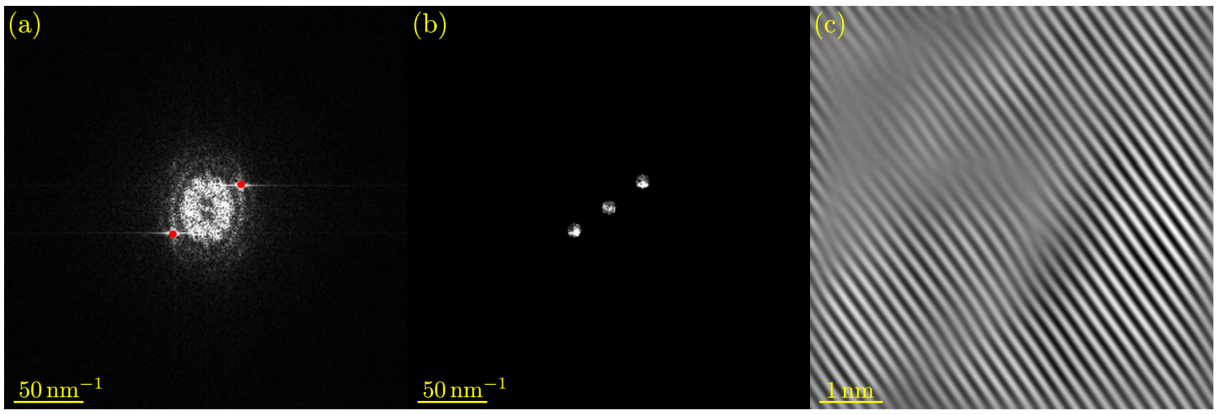

Figure 3.12: **(a)** FFT of the detail of the high-resolution image with marked spots corresponding to discrete spatial frequencies (red dots) in k-space. **(b)** Two spots with the central spot selected for the inverse FFT calculation. **(c)** Image of the inverse FFT with fringes corresponding to the implied stripes in the real-space HR image.

3.3.3 VO_2 thin film – lamella on a TEM heating chip

The fabrication of the lamella on a heating chip was described in Section 2.3.3. The SEM image taken *before* removal of Pt layer and thinning is shown in Figure 3.13 **(a)**. The TEM image in Figure 3.13 **(b)**, which was also taken *before* removal of the Pt layer and further thinning clearly shows the individual layers of the lamella. This also includes the FEBID and FIBID protective layers, which were otherwise hardly distinguishable in the SEM image. The thickness of the evaporated VO_2 thin film can also be verified from this picture to be approximately 550 nm. The lamella in the TEM is rotated by $-90°$ relative to the SEM image (i.e., the substrate is on the right side). This rotation will be present during all of the following characterization in the TEM.

TEM image of the lamella *after* removal of the protective layer and thinning is shown in Figure 3.14 **(a)**. When we performed thinning of the VO_2 layer we decreased its initial thickness in most areas to approximately $200 - 250$ nm. In the lower part of the image the VO_2 layer was removed completely. This area also happens to be the thinnest part

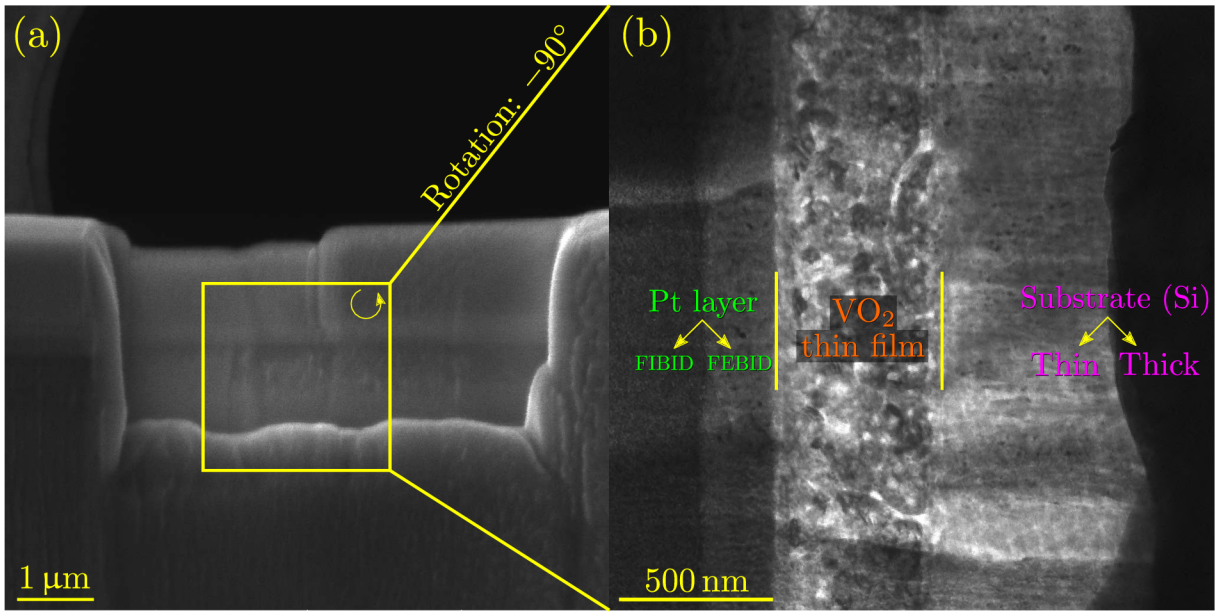

Figure 3.13: Lamella before removal of the Pt layer and before further thinning. **(a)** SEM image. **(b)** TEM image of the detail rotated by −90°. VO_2 layer is in the middle, thin and thick parts of the substrate are on the ride side, and thin FEBID layer with thick FIBID layer are on the left side.

of the lamella that we made in the fabrication process during the initial thinning before the lift-out from the sample and placement on the heating chip (see Figure 2.13).

HR imaging

Figure 3.14 **(b)** shows a HAADF image of the highlighted area. Figure 3.14 **(c)** then shows a high-resolution image of the highlighted "gulf" area. This HR image is a combination of two HR images taken separately, each with a different focus. We used the selected "mountain" area A and "beach" are B for the following FFT analysis. These two specific areas were chosen for a distinct feature of area A discussed in the following text, and the fact that area B is much thinner than area A, thus their comparison with the regions that naturally occur along the coastline with the "sea" here being vacuum.

A magnified image of the "mountain" area A is shown in Figure 3.15 **(a)**. Here a distinct alignment of the surface atoms in the "V" shape with hexagonal ordering of the atoms is noticeable. Figure 3.15 **(b)** shows FFT of the area with marked spots corresponding to discrete spatial frequencies that were used to calculate the inverse FFT shown in Figure 3.15 **(c)**. From the inverse FFT image we obtained some of the distances between atoms in area A: 0.96 Å, 1.24 Å, 1.54 Å, 1.93 Å, 2.73 Å, 2.92 Å, 3.32 Å, 3.85 Å, 4.71 Å, 6.52 Å.

A magnified image of the "beach" area B is shown in Figure 3.16 **(a)**. This area is interesting for its very low thickness. As a matter of fact, the hole to the right side of the detail was initially not present – it suddenly appeared after some of the previous HR imaging. Similarly to the previous approach, Figure 3.16 **(b)** shows the FFT of the area with marked spots corresponding to discrete spatial frequencies that were used to calculate the inverse FFT shown in Figure 3.16 **(c)**. From the inverse FFT image we obtained the following distances between atoms of area B: 1.41 Å, 1.44 Å, 2.27 Å, 2.44 Å.

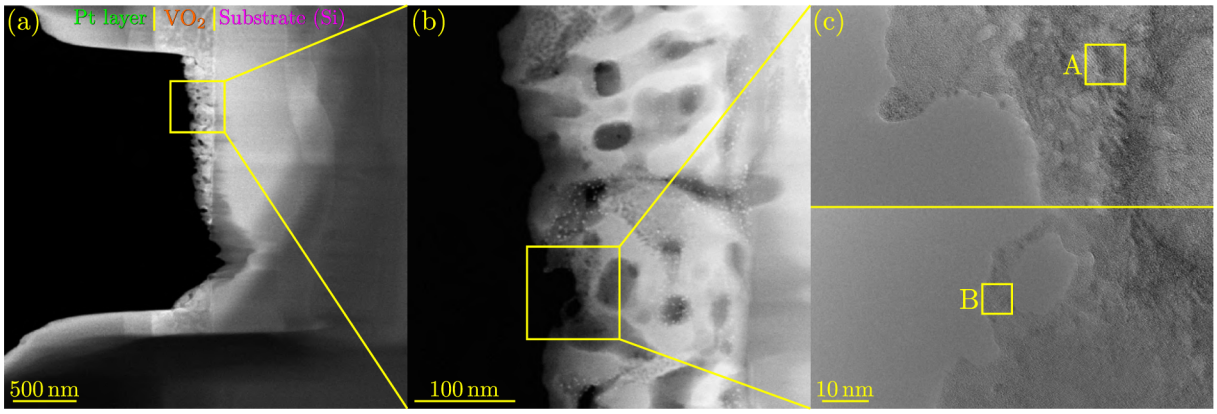

Figure 3.14: **(a)** ADF image of the lamella after thinning. Thickness of the VO_2 layer was decreased, while on the lower part the VO_2 was removed completely. **(b)** HAADF image of the detail. **(c)** High-resolution image of the detail. The image is a combination of 2 individual images of the same area each with different focus.

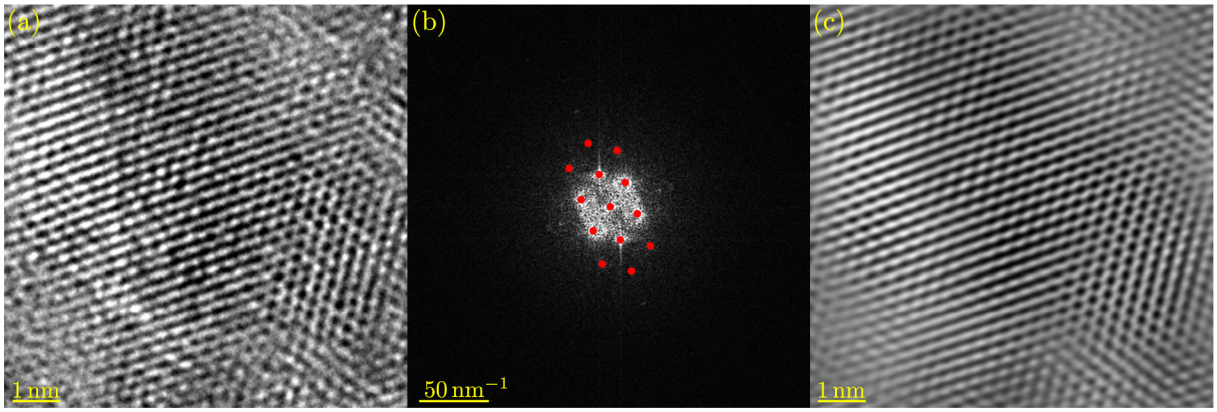

Figure 3.15: **(a)** Detail of the highlighted "mountain" area A. **(b)** FFT of the area with marked spots corresponding to discrete spatial frequencies (red dots) in k-space. **(c)** Inverse FFT created from the marked spots.

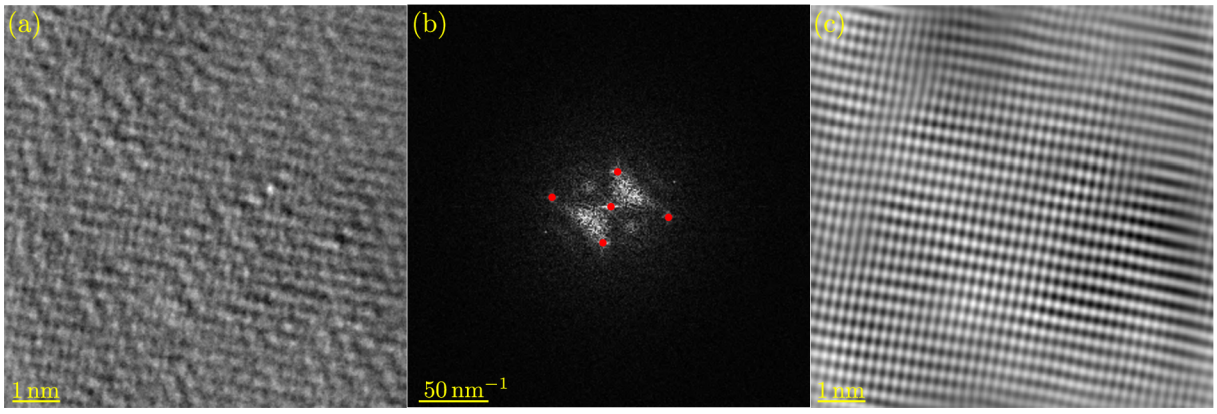

Figure 3.16: **(a)** Detail of the highlighted "beach" area B. **(b)** FFT of the area with marked spots corresponding to discrete spatial frequencies (red dots) in k-space. **(c)** Inverse FFT created from the marked spots.

3.3.4 Electron energy-loss spectroscopy (EELS)

The most important part of the TEM sample characterization was measurement of the electron energy-loss spectroscopy (EELS). All of the EELS measurements were performed on the third sample: lamella on a TEM heating chip. To avoid areas that were used previously for high-resolution imaging, we chose 3 different Areas and acquired spectral line scans (1D) or mapping (2D) in different energy regions (core-loss vs. low-loss) and at different sample temperatures:

1. Area ① (Line scan: Core-loss at 25 °C & 150 °C).
2. Area ② (Line scan: Core-loss at 25 °C, Low-loss at 25 °C & 150 °C).
3. Area ③ (2D scan: Core-loss at 25 °C & 150 °C).

The most explanatory is Area ①, where we measured core-loss EELS as a line scan at different temperatures and compared our data to the data found in a literature. Areas ② and ③ provide additional information on the modification of core-loss EEL spectra under different conditions. Apart from core-loss EELS, we measured also low-loss EELS in the Area ②.

The reason for measuring EELS at different temperatures was to observe a variation of EEL spectra of VO_2 in different phases and analyze stoichiometry, as was described in the first Chapter 1. Measuring EELS at room temperature ($\approx 25\,°C$) was technically not problematic. However, heating the sample above the metal–insulator transition (MIT) temperature ($\approx 68\,°C$) was challenging, hence the employment of the heating chip. Nevertheless, heat transfer between the active area of the heating chip and the VO_2 thin film in the lamella was unpredictable. Therefore, we decided to set the temperature of the active area to 150 °C to ensure we measure VO_2 above the MIT temperature.

EELS – Area ①

The acceleration voltage during the EELS measurements in this Area was 300 kV and we performed only core-loss EELS measurements, that were described in the Section 3.2.2. Location of the Area ① on the sample is shown in Figure 3.17 **(a)** with the detail of the Area in Figure 3.17 **(b)**. Here we performed 2 line scans from the thinner (left) to the thicker (right) part. In the image, colors of the line scans correspond to measurements at different temperatures: red line scan was done at 150 °C, whereas blue line scan was acquired at 25 °C.

Due to the damage of the scanned areas previously encountered on both the "paw" structure and the lamella on a Cu grid, we did not perform these two line scans in the same position one after the other. Instead, we shifted them a few nanometers apart to obtain the data from an unaffected sample, while at the same time being close enough so that the data could be comparable. First, we measured the red line scan at 150 °C and then the blue line scan at 25 °C. Each line scan represents one hundred EELS measurements, where each measurement takes some "dwell" time and there are therefore many counts in each measured spectrum.

The intensity profiles of the two line scans are plotted in Figure 3.17 **(c)**. The numbers on the x axis correspond to individual EELS measurements along the line scans from the thin part of the area on the left (# 1) to the thicker part on the right (# 100). The intensity increases with the position further to the bulk. Two distinct features are noticeable due to the nonuniformity of the sample under each line scan:

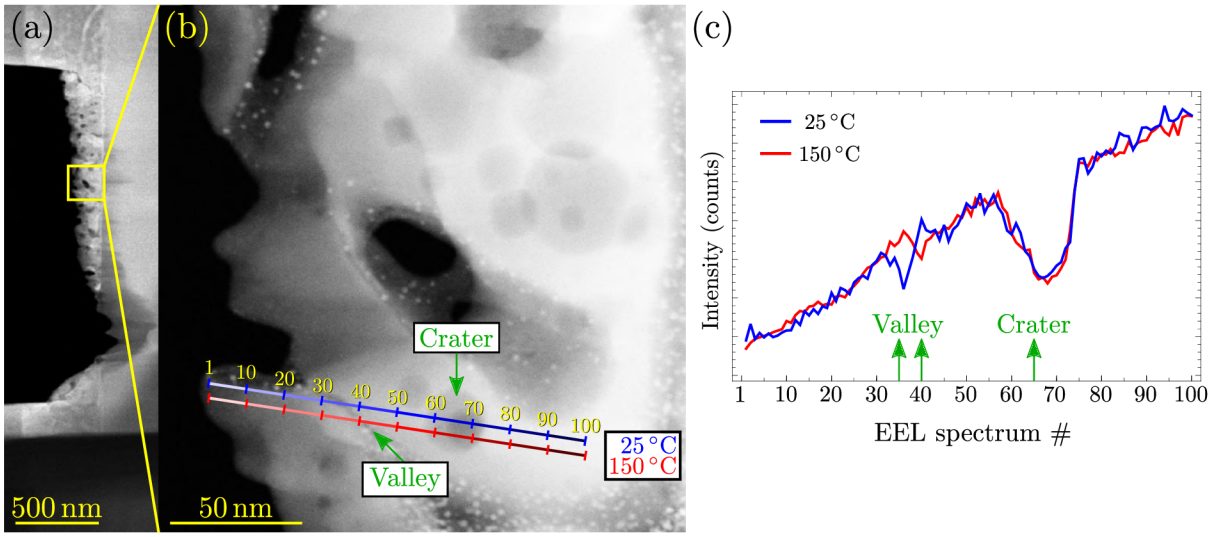

Figure 3.17: **(a)** Cropped ADF image of the lamella. **(b)** HAADF image of the detail. Colored lines correspond to line spectrum images at 150 °C (red line), and 25 °C (blue line). Each line scan represents 100 EELS measurements. Green arrows mark the two concavities. **(c)** Intensity profile of the line scans. The x axis represents the EELS measurement number from thinner (left) to thicker (right) part of the area. Green arrows mark approximate positions of the two concavities.

- First, a smaller drop in intensity around the scans # 35 (for blue line) and # 40 (for red line) that corresponds to a "valley" that can be seen in the image as a darker path that crosses the two line scans (marked with a green arrow).
- Second, a larger drop in intensity around scans # 65 that corresponds to a "crater" that can be seen in the picture as a darker round area (also marked with a green arrow).

For now, we will focus only on the blue line scan at 25 °C. Since each line scan comprises 100 EEL spectra, we averaged the first 10 spectra (i.e., from # 1 to # 10) to obtain 1 spectrum with higher signal-to-noise ratio characteristic to that area. We then did the same for the other spectra (i.e., from # 11 to # 20, from # 21 to # 30 and so on) to obtain altogether 10 characteristic EEL spectra representing each area of the line scan.

We plotted the corresponding characteristic spectra in a 2D waterfall graph shown in Figure 3.18. The data extracted from the paper by Xiaoyan Li et al. [119] previously described in the Section 3.2.2 were used to determine the stoichiometry of each EEL spectrum. To do that, we used the least squares method to fit the spectra of VO, V_2O_3, and VO_2 from the paper to our measured data. The method was set up to fit the O-K edge (highlighted green area in the graph), since that is what discerns each of the stoichiometry from another. We can see that for the areas 1 and 2 the best fit was VO (purple). Next, for the area 3 the best fit was V_2O_3 (green). Then, for all remaining areas 4–10 the best fit was VO_2 (orange).

This result indicates a change of stoichiometry based on the thickness of the layer (i.e., position in the line scan). VO occurs in the very thin part (left), V_2O_3 occurs in a little thicker part, and VO_2 prevails in bulk (on the right). This outcome is in agreement with the change of V valence shown in Figure 3.5, where the stoichiometry changes from VO to V_2O_3 to VO_2 with increasing distance from the sample surface.

In the paper, VO exists as a few-nanometers-thin layer on a surface of the sample. To this data we compare our area of the sample that is also a few nanometers thin. Since VO can possibly be present from both up and below of the sample, the prevalence of V_2O_3 in the slightly thicker area and VO_2 in bulk can be explained as their stoichiometry being in majority in these areas.

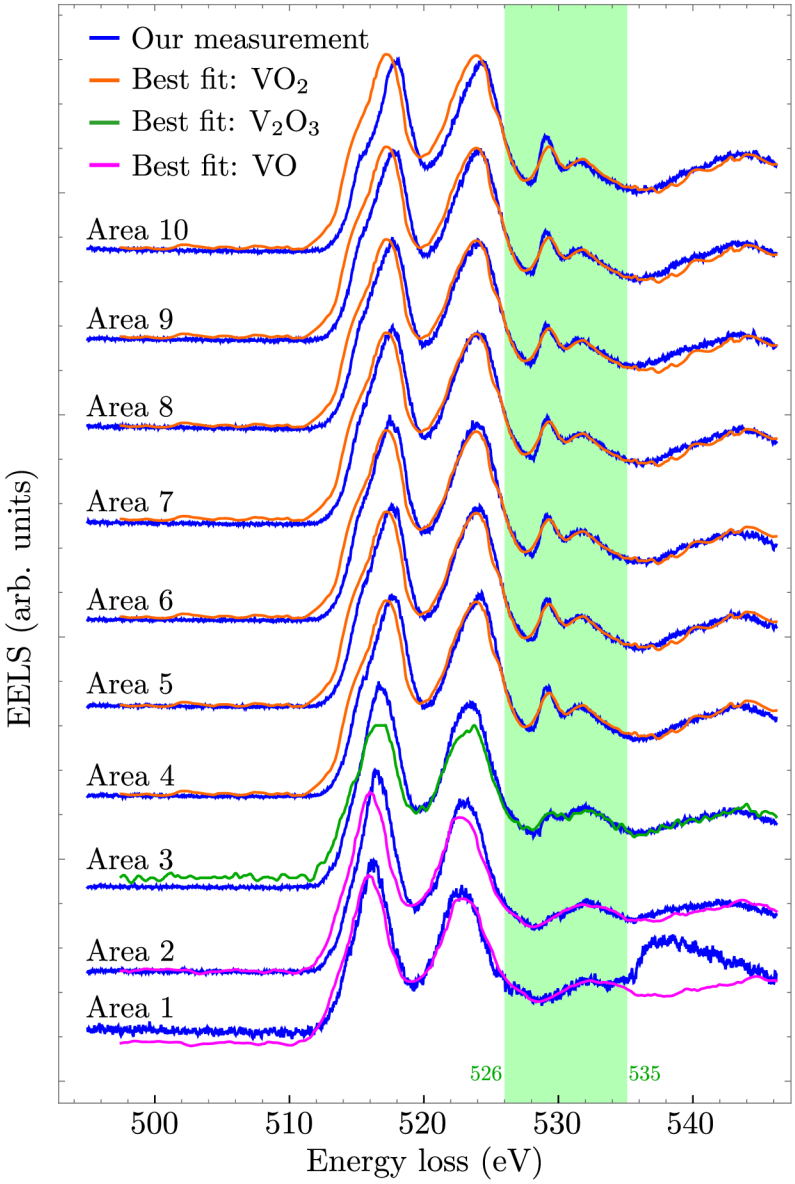

Figure 3.18: Measured core-loss EEL spectra of the 10 areas of the blue line scan at 25 °C (blue). Each spectrum of an area comprises 10 averaged EEL spectra. Spectra are fitted with the data extracted from Xiaoyan Li et al. [119]. The fit was done on the O-K edge in the range of energies 526–535 eV (highlighted green area). Areas 1 and 2 correspond to VO (purple), area 3 corresponds to V_2O_3 (green), and areas 4–5 correspond to VO_2 (orange).

Now, we will focus not only on the blue line scan at 25 °C, but also on the red line scan at 150 °C. After the averaging described previously, we obtained also 10 characteristic EEL spectra of 10 areas of the red line scan. We plotted the corresponding characteristic spectra at both temperatures in a 2D waterfall graph shown in Figure 3.19.

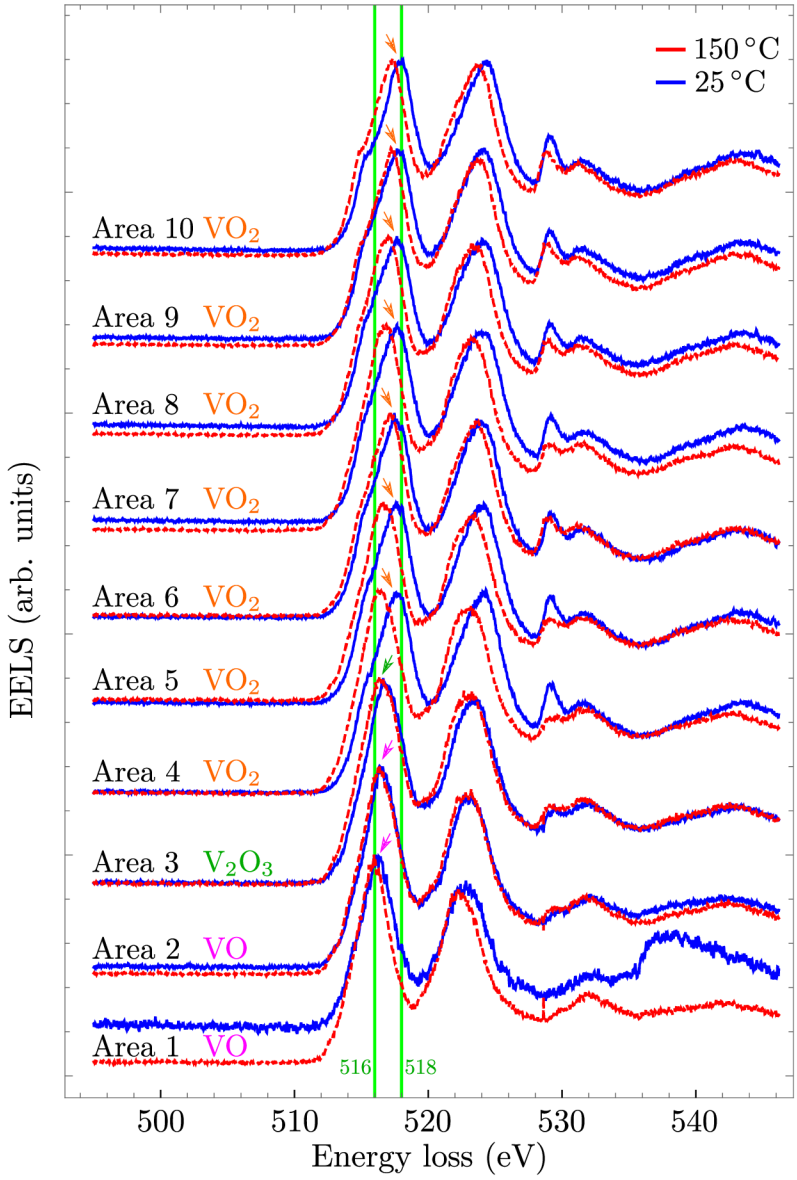

Figure 3.19: 2D waterfall graph with measured core-loss EEL spectra of the corresponding 10 areas of the blue line scan at 25 °C (blue) and red line scan at 150 °C (red). Each spectrum of an area comprises 10 averaged EEL spectra. Arrows point at the position of the left V-L_3 peak at 25 °C.

In the waterfall graph is observable second feature of the difference between the spectra of VO, V_2O_3, and VO_2: An energy shift of the vanadium peaks. This shift was also described in the Section 3.2.2, albeit only for room temperature (25 °C). Therefore, to confirm this occurrence, we focus only on the blue spectra at 25 °C and survey position of the left V-L_3 peak between two green grid lines at 516 eV and 518 eV.

Positions of both vanadium peaks for both temperatures are plotted in Figure 3.20. Vanadium V-L_3 peaks for 25 °C corresponding to VO (areas 1 and 2) are close to the grid line at 516 eV. The same can be said about the vanadium V-L_3 peak corresponding to V_2O_3 (area 3). However, an energy shift of $\approx$ 1 eV is noticeable for the vanadium V-L_3 peaks corresponding to VO_2 (areas 4–10). This outcome is in agreement with the observations of this phenomena in the literature, where for example energy shift of 1.2 eV

was reported going from V_2O_3 to VO_2 [124]. Meanwhile, energy shifts of the individual positions of vanadium peaks at 150 °C measured by EELS are not reported in the literature and are therefore open to further analysis that will not be part of this Thesis. However, measurements of VO_2 at different temperatures by X-ray absorption spectroscopy (XAS) have been reported and can be used to help resolve acquired EELS data [125, 126, 127].

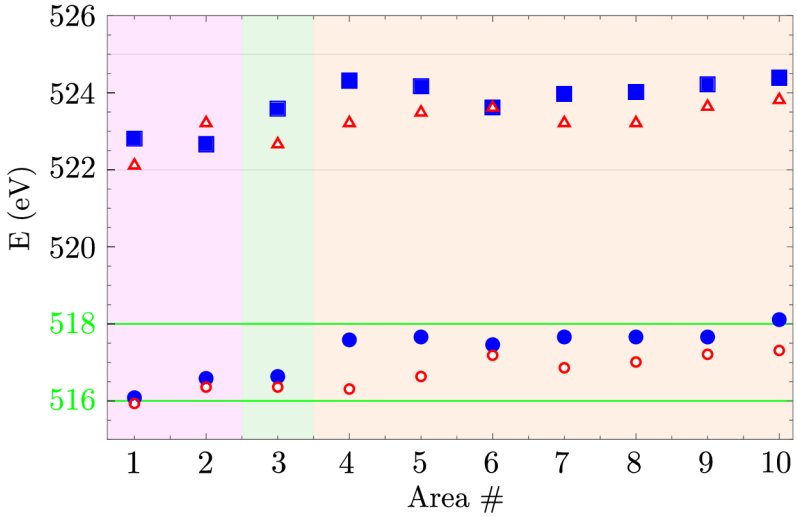

Figure 3.20: Positions of both vanadium peaks at 25 °C (blue marks) and 150 °C (red marks). A small shift (≈ 1 eV) of V-L_3 peaks (bottom) towards higher energies is apparent for areas # 4 to# 10 corresponding to peaks of VO_2.

EELS – Area ②

The acceleration voltage during the EELS measurements in this Area was decreased to 120 kV compared to 300 kV used in Area ①. Location of the Area ② on the sample is shown in Figure 3.21 **(a)** with the detail of the Area in Figure 3.21 **(b)**.

We performed several line scans from vacuum (left) to material (right), all of them in the same position in contrast to Area ①, where we shifted the line scans a few nanometers apart. The intensity profile of the line scan is plotted in Figure 3.21 **(c)**. First, we measured low-loss EELS at 25 °C, then core-loss EELS also at 25 °C, and finally low-loss EELS again but now at 150 °C. Since the line scan represents 100 EELS measurements, we again averaged them to acquire 10 EEL spectra representing each area, similarly to line scans in Area ①.

Core-loss EEL spectra corresponding to each area are plotted in a 2D waterfall graph in Figure 3.22. Here, EEL spectra of areas # 1 to # 3 correspond to the measurement of vacuum and EEL spectra of areas # 4 to # 10 correspond to material. As a consequence of understanding the behaviour of core-loss spectra in Area ①, we can proceed with the evaluation of correlation between the shifts of V-L_3 peaks and the intensity of O-K peaks in this Area:

- To obtain a higher certainty in determining core-loss peak energies, we used dual EELS during the measurements. We also increased the dispersion to 25 meV/px compared to 10 meV/px used previously. However, this resulted in artefacts in the EEL spectra marked by **(a)**.
- Higher O-K peaks marked by **(b)** indicate the presence of VO_2 (orange spectra) compared to lower intensity of these peaks in V_2O_3 (green spectra).

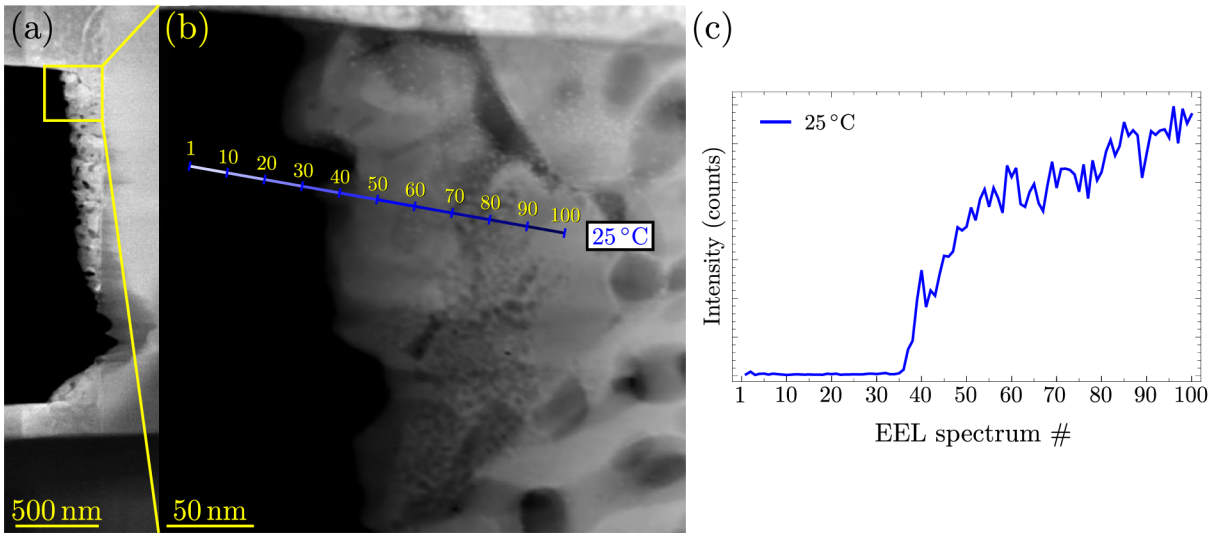

Figure 3.21: **(a)** Cropped ADF image of the lamella. **(b)** ADF image of the detail. Blue line corresponds to a line spectrum image at 25 °C. The line scan represents 100 EELS measurements. **(c)** Intensity profile of the line scan. The x axis represents the EELS measurement number from thinner (left) to thicker (right) part of the area.

- Energy shifts of V-L_3 peaks that are shown in Figure 3.23 are also consistent with the results of previous measurements in Area ①: VO_2 peaks are shifted $\approx$ 1 eV towards higher energies compared to V_2O_3 peaks. This is illustrated by two green vertical grid lines at 516 eV and 518 eV, where VO_2 peaks are close to 518 eV, whereas V_2O_3 peaks remain in the middle around 517 eV.

Apart from core-loss EELS measurements, we performed the measurements of low-loss EELS, that was described in the Section 3.2.1. Before measuring previously described core-loss EELS at 25 °C, we measured low-loss EELS also at 25 °C. Then, we heated the sample and measured low-loss EELS again but at 150 °C. Both low-loss EELS measurements were averaged like core-loss EELS before to obtain 10 EEL spectra characteristic for 10 parts of the line scan. These spectra for both temperatures were plotted in a 2D waterfall graph in Figure 3.24.

There are two basic causations substantially affecting the shape of these low-loss spectra:

1. Deducing from the previously encountered negative effects of electrons on the VO_2 layer during both EDXS measurements and HR imaging, we can assume the same is true for EELS measurements as well. This assumption will indeed turn out accurate later after the investigation of Area ③. We should therefore take into consideration the fact that the line scan at 150 °C was performed on the same place after two previous measurements, which can alter the value of information this measurement provides.
2. Although FWHM of the zero-loss peak (ZLP) was the same (0.11 eV) in both measurements, its shape was very different at each temperature. Altogether, an asymmetry of both sides of the ZLP is evident in both measurements – it is more noticeable for measurement at 25 °C (blue spectra). Similar change of symmetry of the ZLP during the increase of temperature to 150 °C was encountered also in other low-loss measurements performed in different areas. Since asymmetry of the ZLP was quite different at each temperature, comparison of both EEL spectra was not possible.

Due to the complications explained above, the analysis of all low-loss EEL spectra turned out problematic and any results drawn from the measured data were utterly inconclusive.

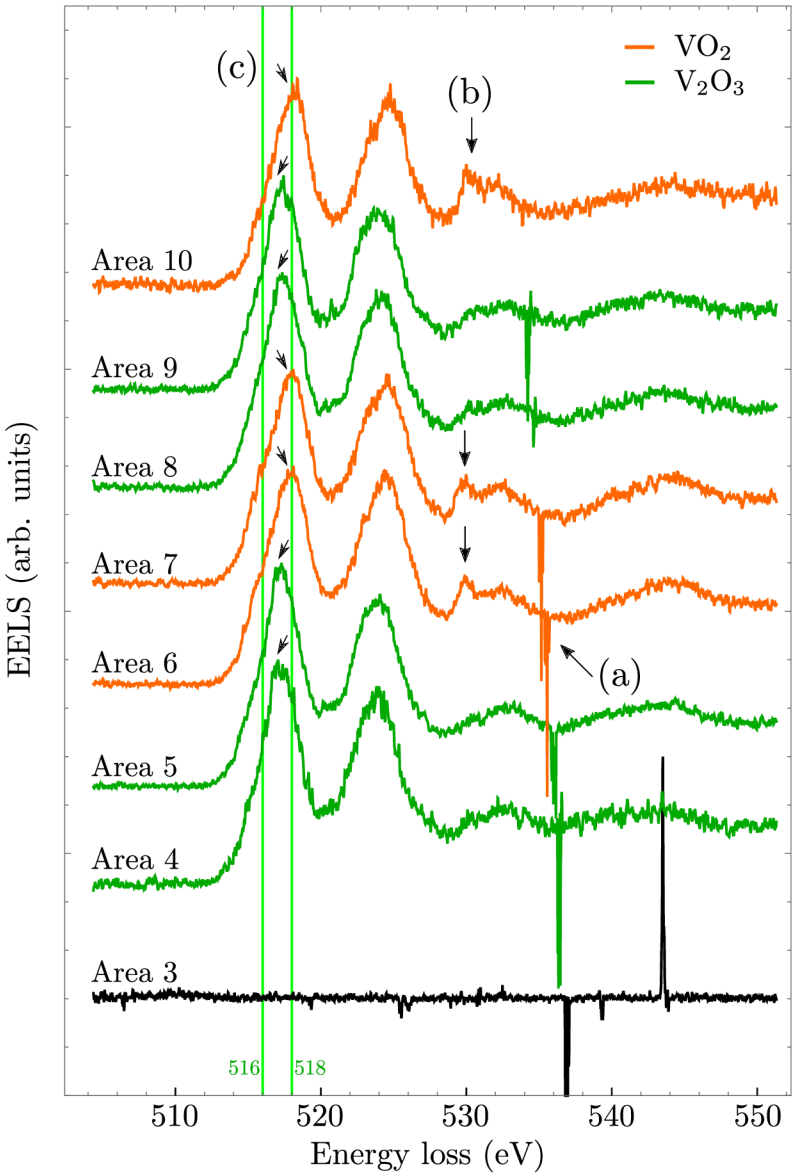

Figure 3.22: 2D waterfall graph with measured core-loss EEL spectra of the corresponding 8 areas of the line scan measured at 25 °C. Areas 1–3 correspond to measurements of vacuum and only area 3 (black spectrum) is included. Each spectrum of an area comprises 10 averaged EEL spectra. **(a)** Artefacts as a consequence of using dual EELS. **(b)** O-K peaks indicting presence of VO_2. **(c)** Arrows pointing at the position of the V-L_3 peaks of VO_2 (orange) and V_2O_3 (green). VO_2 peaks are shifted $\approx 1\,\text{eV}$ compared to V_2O_3 peaks.

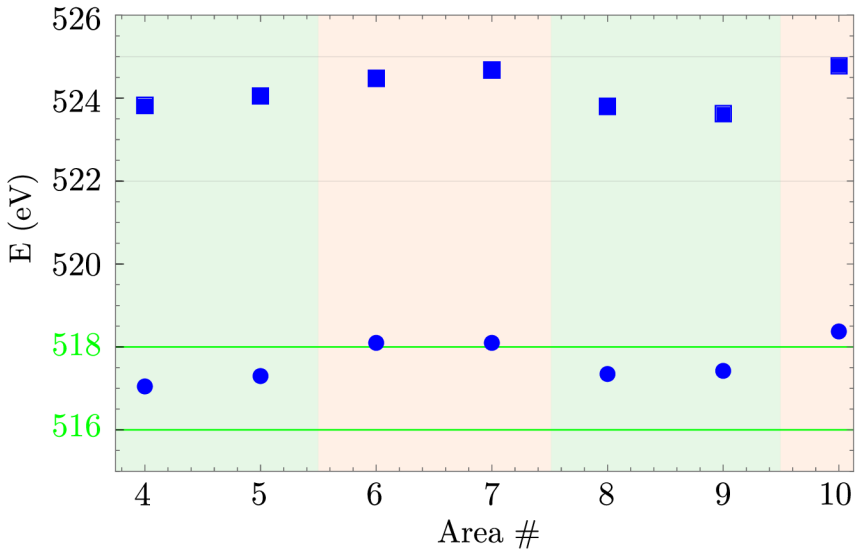

Figure 3.23: Positions of both vanadium peaks at 25 °C. A small shift (≈ 0.5 eV) of V-L_3 peaks (bottom) towards higher energies is apparent for areas # 6, # 7, and # 10 corresponding to peaks of VO_2. Areas 1–3 correspond to measurements of vacuum and peak positions are therefore not included.

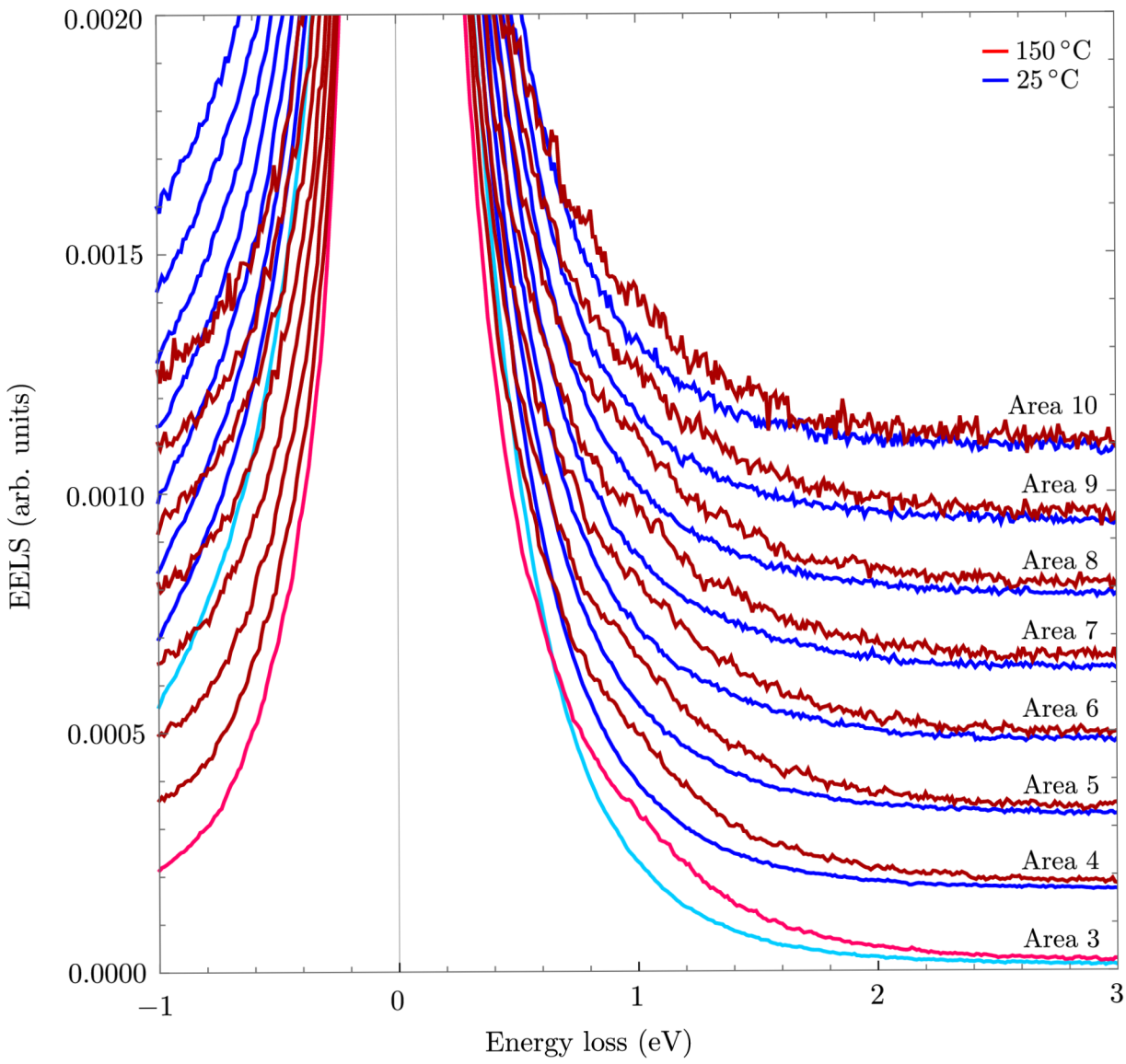

Figure 3.24: 2D waterfall graph with measured low-loss EEL spectra of the corresponding 8 areas of the line scan measured at 25 °C (blue) and 150 °C (red). Each spectrum of an area comprises 10 averaged EEL spectra. Areas 1–3 correspond to measurements of vacuum and only area 3 is included: light blue for 25 °C and magenta for 150 °C. Note the asymmetry for example of the light blue spectra on both sides of the ZLP.

EELS – Area ③

The acceleration voltage during the EELS measurements in this Area was again 120 kV and the dispersion was again increased to 25 meV/px like in Area ②. Location of the Area ③ on the sample is shown in Figure 3.25 **(a)** with the detail of the Area in Figure 3.25 **(b)**. In this Area, we performed a 2D scan instead of line scans (1D) like in the previous measurements. Two 2D EELS measurements were performed on the same place first at 25 °C and then at 150 °C.

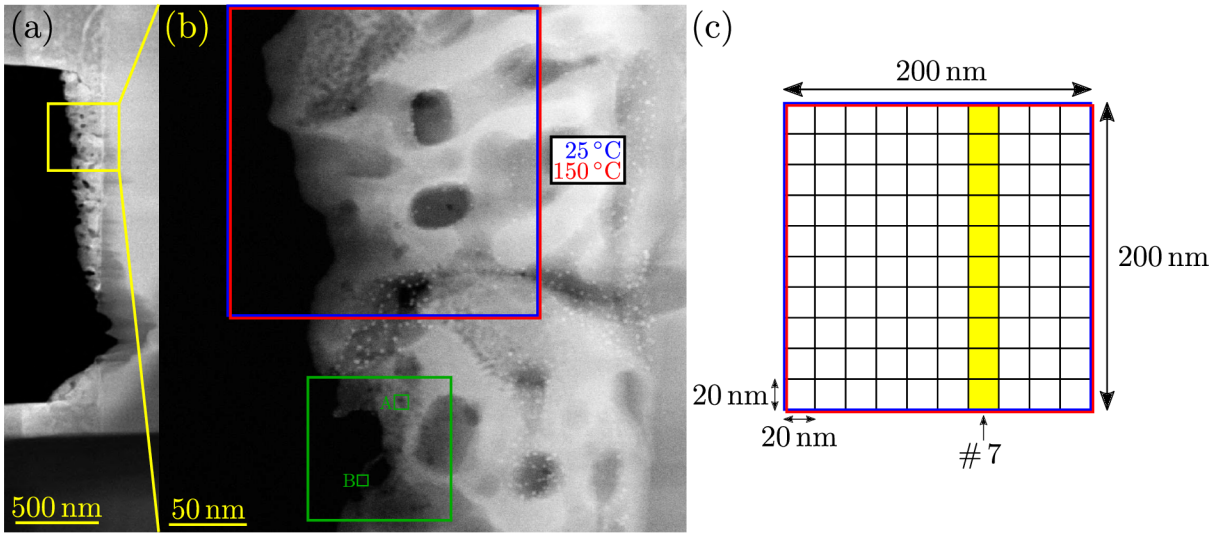

Figure 3.25: **(a)** Cropped ADF image of the lamella. **(b)** ADF image of the detail. Squares correspond to 2D spectrum images at 25 °C (blue) and 150 °C (red). In addition, green squares correspond to an HR imaging performed previously on "mountain" (A) and "beach" (B) areas. **(c)** Schematic illustration of the 2D scan that comprises 100 EELS measurements in a matrix of 10 × 10 pixels. Squares for both temperatures are 200 × 200 nm^2 and therefore the size of each pixel is 20 × 20 nm^2. The number of EEL spectra (here for example highlighted # 7) corresponds to a column of 10 pixels (i.e., 10 EELS measurements).

Schematic illustration of the 2D scan is shown in Figure 3.25 **(c)**. The scanned area was a square of 200 × 200 nm^2 consisting of a matrix of 10 × 10 pixels with each pixel the size of 20 × 20 nm^2. We averaged each column comprising 10 EEL spectra separately to obtain a characteristic EEL spectrum of every column (e.g., area # 7 corresponds to a column # 7 comprising 10 individual EELS measurements). To avoid drift during the measurement, we switched on drift correction after each row.

Core-loss EEL spectra corresponding to each area (each column) are plotted in a 2D waterfall graph in Figure 3.26. The spectra at both temperatures corresponding to the same area are plotted together, with the position of V-L_3 peaks shown in Figure 3.27. Complementary to what was observed in the earlier measurements, the V-L_3 peaks (for 25 °C) shift towards higher energies when the spectra correspond to VO_2. However, this shift is more subtle due to the scan of a bigger Area, where we average EEL spectra of vastly different areas with different surface inconsistencies (craters etc.). Furthermore, similarly to what was stated before (Area ①), the spectra at 150 °C are open to further analysis that will not be part of this Thesis.

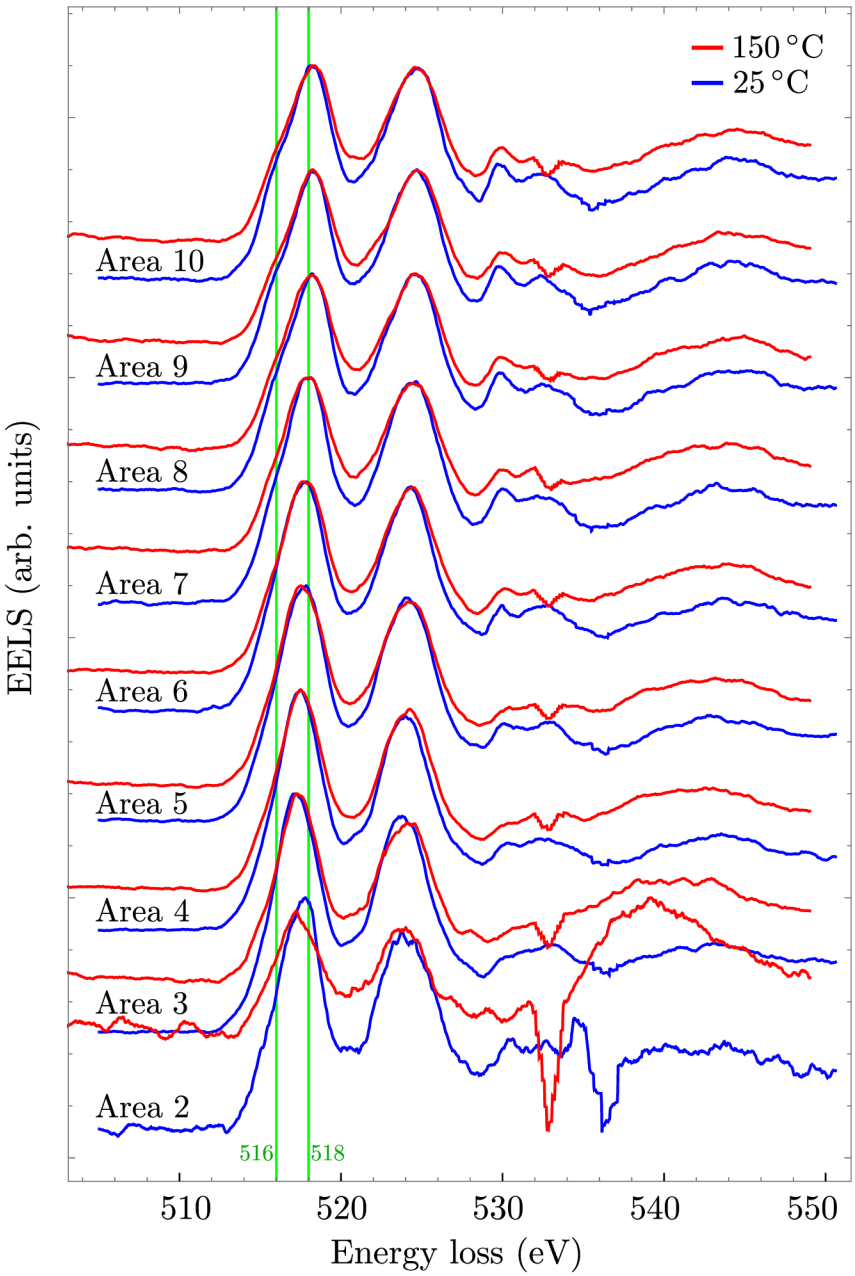

Figure 3.26: 2D waterfall graph with measured core-loss EEL spectra of the corresponding 9 areas (columns) of the 2D scan measured at 25 °C (blue) and 150 °C (red). Each spectrum of an area comprises 10 averaged EEL spectra. Area 1 corresponds to measurement of vacuum and is not included.

There is one noticeable difference between the spectra at different temperatures: The spectra at 150 °C have lower intensity. This could be again consequence of a measurement in the same spots, the system (microscope + spectrometer) instability, or an inherent feature of measuring at higher temperature. To support this statement, Figure 3.28 **(a)** shows the sample after the first measurement at 25 °C and Figure 3.28 **(b)** shows the same area after the second measurement at 150 °C. In the thinner (left) part of the image taken after the second measurement **(b)**, we can discern (despite the image being slightly out of focus) a grid $20 \times 20\,\mathrm{nm}^2$, which is exactly the size of one pixel of both measurements. Further measurements and analysis would be needed to clarify the cause of the damage of

the sample – whether it is because of multiple measurements in the same spot, or because of measurement at higher temperature. However, we can say that the sample damage can take part in the difference between both spectra at different temperatures.

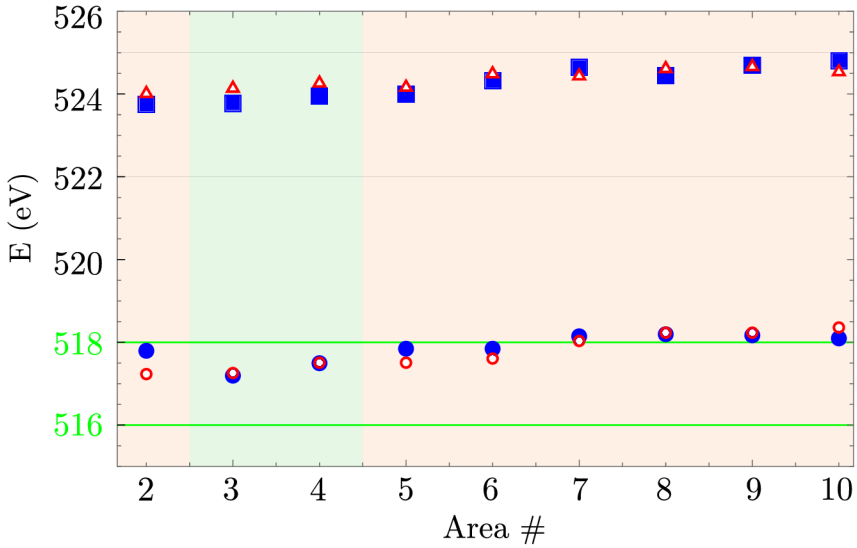

Figure 3.27: Positions of both vanadium peaks at 25 °C (blue marks) and 150 °C (red marks). A small shift ($\approx$ 0.5 eV) of V-L_3 peaks (bottom) towards higher energies is apparent for areas # 2 and # 5 to # 10 corresponding to peaks of VO_2. Area 1 corresponds to measurement of vacuum and the peak is therefore not included.

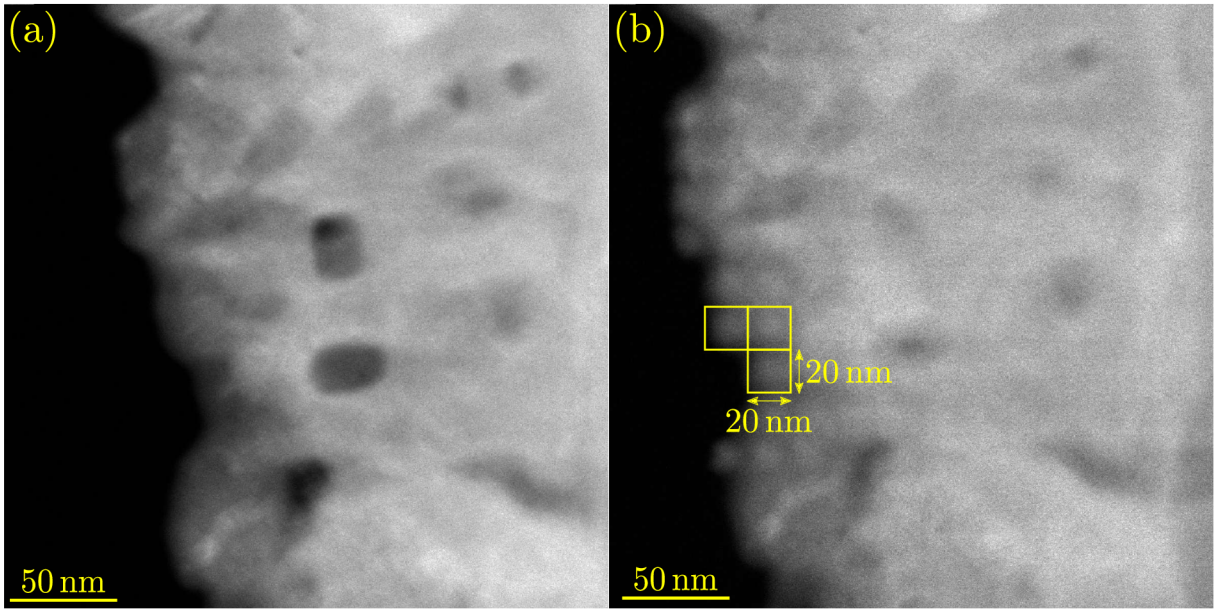

Figure 3.28: ADF images of the scanned Area taken **(a)** before and **(b)** after the second measurement at 150 °C. In the thinner area (left) of the sample in **(b)**, there is a noticeable grid of 20 × 20 nm^2, which is the same size as one pixel in both measurements.

Conclusion

This Thesis was focused on the fabrication of VO_2 samples and their subsequent characterization in a transmission electron microscope (TEM). Although the properties of VO_2 and its use for the fabrication of metasurfaces have been extensively studied in the literature, the optimization of the properties required for its fabrication remains challenging. The behaviour of VO_2 after the fabrication can be studied at the atomic level by TEM. Such characterization yields valuable insight into the inner workings of its structure in both dielectric and metallic phases.

The first Chapter introduces VO_2 as a tunable material that undergoes a metal–insulator transition (MIT) at $\approx 68\,^{\circ}\mathrm{C}$. The phase change from a dielectric at low temperatures to a metal at high temperatures results in a change of the crystallographic structure of the material. This is the reason for the unique electrical and optical properties of VO_2 that were described in this Chapter. Furthermore, different stoichiometries of V_xO_y like VO, V_2O_3, and V_2O_5 were introduced, and several other VO_2 polymorphs were mentioned along with their characteristics. On top of the theoretical background presented in this Chapter, ellipsometric measurements of the main sample used within this Thesis were shown where its desired switching property was demonstrated.

The second Chapter was devoted to the fabrication of VO_2 samples. Deposition of VO_2 in the correct stoichiometry is challenging and the optimization of parameters of each deposition technique plays a major role in this task. For that reason, in-depth description of the deposition of VO_2 thin films was investigated for three deposition techniques that differ in the nature of their deposition character. Pulsed laser deposition (PLD) turned out to be one of the most suitable techniques due to the congruent transfer of target material to the sample. Nonidentical evaporation temperatures and sputtering rates of the individual components of the target complicate the use of electron beam evaporation and ion beam sputtering, respectively, for the deposition of VO_2. However, after optimization, these techniques were reported to produce the desired compound VO_2 that can undergo phase change.

Focused ion beam (FIB) as a powerful tool for the fabrication of samples was introduced further in this chapter. Its utilization for the preparation of thin lamellae was thoroughly described along with detailed information on the whole process arising from the Author's vast experience with this method. The last part of this Chapter was dedicated to the description of fabrication of samples that were used for the subsequent characterization in TEM. Altogether, three types of samples were fabricated: VO_2 powder on a holley C grid, VO_2 lamella on a TEM Cu grid, and VO_2 lamella on a TEM heating chip. The description of these samples followed the chronological order of their fabrication, where with later samples increased both the fabrication difficulty and valuable information attainment. The fabrication of the last sample – lamella on a heating chip – turned out to be the most demanding, and after several attempts also the most stressful. However, its worth was later revealed during the characterization in TEM.

The third Chapter was dedicated to TEM. First, the basic working principles of the microscope were introduced, and more detailed information on the individual characterization techniques was presented. The rest of the Chapter was allocated for the characterization of all three fabricated samples. Energy-dispersive X-ray spectroscopy (EDXS) was used for the initial chemical composition analysis of the first and second samples: VO_2 powder on a holley C grid and VO_2 lamella on a TEM Cu grid. Extensive high-resolution

imaging of all three samples was performed mainly for the analysis of the crystallographic structure of these samples. Due to the lack of a theoretical model of the structure of VO_2, and the lack of more in-depth consideration of the acquired data, this analysis remains open to future interpretation.

The most coveted information was obtained using electron energy-loss spectroscopy (EELS) on the third sample – VO_2 lamella on a TEM heating chip. Throughout the measurements, significant interest in the core-loss part of the EEL spectra was present, while the measurement of the low-loss part of the EEL spectra was so far explained to be inconclusive. The obtained core-loss spectrum images were compared to the outcomes of the literature, which were discussed in the first part of the Chapter. Our results turned out to be in agreement with the findings of the scientific community and consistent throughout the measurements of different parts of the sample. Apart from the measurement at room temperature, heating of the VO_2 sample was possible due to the heating chip the lamella was placed on. However, both low-loss and mainly core-loss data of the heated VO_2 are open to future deciphering and evaluation.

Outlook

In summary, this Thesis represents an initial step towards the discovery of a direct link between the local optical response and the MIT close to the domain boundaries, atomic-scale defects or interfaces in VO_2 nanostructures. Therefore, as clearly seen in the previous summary, many unanswered phenomena remain to be explored. Thus, precisely conducted experiments are key to fundamental understanding of MIT in VO_2. In the last part of this text, we mention some of the suggestions for follow-up experimental and theoretical development.

Sample fabrication

Purchased VO_2 powder possesses the advantage of quick sample preparation and high purity. This, combined with the likelihood that its pieces – rods in particular – are monocrystals, opens up the possibility of the study of a crystallographic structure of VO_2 for comparison with simulated data.

Although the lamella on a heating chip provided most of the desired valuable insights, the process of its fabrication is rather inconvenient. Therefore, study of the MIT could be done on VO_2 thin films deposited directly on a heating chip.

EELS measurements

EELS measurements described in this Thesis provide solid foundation for the measurements in the future. Here is a short summary of some of the most notable outcomes:

A series of consistent EELS measurements is needed to determine whether measuring at the same spot actually results in a damaged area, and thus making subsequent measurements on the same spot essentially worthless.

Another question to be answered is whether a measurement at higher temperature damages the sample more than measurement at lower temperature. The implication from this would be that the high-temperature measurement would have to be done as the last one.

The correct interpretation of data obtained at higher temperature remains to be done, as was described in the main text. For this, the XAS measurements can provide valuable insight into what to expect from the EELS measurements.

Lastly, low-loss EELS was mentioned as being so far inconclusive. This can be changed with more diligent approach during both the measurement and the adjustment of the machine.

After what was stated above, one can be sure that many exciting revelations in the fundamental aspects of the metal–insulator transition of VO_2 await the brave souls who decide to continue on this journey.

Bibliography

1. KILDISHEV, A. V.; BOLTASSEVA, A.; SHALAEV, V. M. Planar Photonics with Metasurfaces. *Science*. 2013, **339**(6125), 1232009. Available from DOI: 10.1126/science.1232009.
2. GENEVET, P.; CAPASSO, F.; AIETA, F.; KHORASANINEJAD, M., et al. Recent advances in planar optics: from plasmonic to dielectric metasurfaces. *Optica*. 2017-01, **4**(1), 139–152. Available from DOI: 10.1364/OPTICA.4.000139.
3. SHALTOUT, A. M.; KILDISHEV, A. V.; SHALAEV, V. M. Evolution of photonic metasurfaces: from static to dynamic. *J. Opt. Soc. Am. B*. 2016-03, **33**(3), 501–510. Available from DOI: 10.1364/JOSAB.33.000501.
4. YANG, Z.; KO, C.; RAMANATHAN, S. Oxide Electronics Utilizing Ultrafast Metal-Insulator Transitions. *Annu. Rev. Mater. Res.* 2011-08, **41**, 337–67. Available from DOI: 10.1146/annurev-matsci-062910-100347.
5. WAN, C.; ZHANG, Z.; WOOLF, D.; HESSEL, C. M., et al. On the Optical Properties of Thin-Film Vanadium Dioxide from the Visible to the Far Infrared. *Annalen der Physik*. [N.d.], **531**(10), 1900188. Available from DOI: https://doi.org/10.1002/andp.201900188.
6. SHARMA, Y.; HOLT, M. V.; LAANAIT, N.; GAO, X., et al. Competing phases in epitaxial vanadium dioxide at nanoscale. *APL Materials*. 2019, **7**(8), 081127. Available from DOI: 10.1063/1.5115784.
7. CURRIE, M.; WHEELER, V. D.; DOWNEY, B.; NEPAL, N., et al. Asymmetric hysteresis in vanadium dioxide thin films. *Opt. Mater. Express*. 2019-09, **9**(9), 3717–3728. Available from DOI: 10.1364/OME.9.003717.
8. MORIN, F. J. Oxides Which Show a Metal-to-Insulator Transition at the Neel Temperature. *Phys. Rev. Lett.* 1959-07, **3**, 34–36. Available from DOI: 10.1103/PhysRevLett.3.34.
9. WAN, C.; ZHANG, Z.; WOOLF, D.; HESSEL, C. M., et al. On the Optical Properties of Thin-Film Vanadium Dioxide from the Visible to the Far Infrared. *Annalen der Physik*. 2019, **531**(10), 1900188. Available from DOI: https://doi.org/10.1002/andp.201900188.
10. NAG, J.; HAGLUND, R. F.; ANDREW PAYZANT, E.; MORE, K. L. Non-congruence of thermally driven structural and electronic transitions in VO2. *Journal of Applied Physics*. 2012, **112**(10), 103532. Available from DOI: 10.1063/1.4764040.
11. WU, B.; ZIMMERS, A.; AUBIN, H.; GHOSH, R., et al. Electric-field-driven phase transition in vanadium dioxide. *Phys. Rev. B*. 2011-12, **84**, 241410. Available from DOI: 10.1103/PhysRevB.84.241410.
12. LEI, D. Y.; APPAVOO, K.; LIGMAJER, F.; SONNEFRAUD, Y., et al. Optically-Triggered Nanoscale Memory Effect in a Hybrid Plasmonic-Phase Changing Nanostructure. *ACS Photonics*. 2015, **2**(9), 1306–1313. Available from DOI: 10.1021/acsphotonics.5b00249.

13. AETUKURI, N. B.; GRAY, A. X.; DROUARD, M.; COSSALE, M., et al. Control of the metal–insulator transition in vanadium dioxide by modifying orbital occupancy. *Nature Physics*. 2013-10, **9**(10), 661–666. ISSN 1745-2481. Available from DOI: 10.1038/nphys2733.

14. GOODENOUGH, J. B. Metallic oxides. *Progress in Solid State Chemistry*. 1971, **5**, 145–399. ISSN 0079-6786. Available from DOI: https://doi.org/10.1016/0079-6786(71)90018-5.

15. SHI, R.; SHEN, N.; WANG, J.; WANG, W., et al. Recent advances in fabrication strategies, phase transition modulation, and advanced applications of vanadium dioxide. *Applied Physics Reviews*. 2019, **6**(1), 011312. Available from DOI: 10.1063/1.5087864.

16. ZHANG, Y.; XIONG, W.; CHEN, W.; ZHENG, Y. Recent Progress on Vanadium Dioxide Nanostructures and Devices: Fabrication, Properties, Applications and Perspectives. *Nanomaterials*. 2021, **11**(2). ISSN 2079-4991. Available from DOI: 10.3390/nano11020338.

17. LI, W.; JI, S.; LI, Y.; HUANG, A., et al. Synthesis of VO2 nanoparticles by a hydrothermal-assisted homogeneous precipitation approach for thermochromic applications. *RSC Adv.* 2014, **4**, 13026–13033. Available from DOI: 10.1039/C3RA47666A.

18. CAO, C.; GAO, Y.; LUO, H. Pure Single-Crystal Rutile Vanadium Dioxide Powders: Synthesis, Mechanism and Phase-Transformation Property. *The Journal of Physical Chemistry C*. 2008, **112**(48), 18810–18814. Available from DOI: 10.1021/jp8073688.

19. OKA, Y.; SATO, S.; YAO, T.; YAMAMOTO, N. Crystal Structures and Transition Mechanism of VO2(A). *Journal of Solid State Chemistry*. 1998, **141**(2), 594–598. ISSN 0022-4596. Available from DOI: https://doi.org/10.1006/jssc.1998.8025.

20. POPURI, S. R.; MICLAU, M.; ARTEMENKO, A.; LABRUGERE, C., et al. Rapid Hydrothermal Synthesis of VO2 (B) and Its Conversion to Thermochromic VO2 (M1). *Inorganic Chemistry*. 2013, **52**(9), 4780–4785. Available from DOI: 10.1021/ic301201k. PMID: 23581429.

21. HAGRMAN, D.; ZUBIETA, J.; WARREN, C. J.; MEYER, L. M., et al. A New Polymorph of VO2Prepared by Soft Chemical Methods. *Journal of Solid State Chemistry*. 1998, **138**(1), 178–182. ISSN 0022-4596. Available from DOI: https://doi.org/10.1006/jssc.1997.7575.

22. LIU, L.; CAO, F.; YAO, T.; XU, Y., et al. New-phase VO2 micro/nanostructures: investigation of phase transformation and magnetic property. *New J. Chem.* 2012, **36**, 619–625. Available from DOI: 10.1039/C1NJ20798A.

23. WU, C.; HU, Z.; WANG, W.; ZHANG, M., et al. Synthetic paramontroseite VO2 with good aqueous lithium–ion battery performance. *Chem. Commun.* 2008, 3891–3893. Available from DOI: 10.1039/B806009F.

24. WEGKAMP, D.; STÄHLER, J. Ultrafast dynamics during the photoinduced phase transition in VO2. *Progress in Surface Science*. 2015, **90**(4), 464–502. ISSN 0079-6816. Available from DOI: https://doi.org/10.1016/j.progsurf.2015.10.001.

25. SHAO, Z.; CAO, X.; LUO, H.; JIN, P. Recent progress in the phase-transition mechanism and modulation of vanadium dioxide materials. *NPG Asia Materials*. 2018-07, **10**(7), 581–605. ISSN 1884-4057. Available from DOI: 10.1038/s41427-018-0061-2.

26. CAO, J.; FAN, W.; ZHENG, H.; WU, J. Thermoelectric Effect across the Metal—Insulator Domain Walls in VO2 Microbeams. *Nano Letters*. 2009, **9**(12), 4001–4006. Available from DOI: 10.1021/nl902167b. PMID: 19810748.

27. LEE, M.-J.; PARK, Y.; SUH, D.-S.; LEE, E.-H., et al. Two Series Oxide Resistors Applicable to High Speed and High Density Nonvolatile Memory. *Advanced Materials*. 2007, **19**(22), 3919–3923. Available from DOI: https://doi.org/10.1002/adma.200700251.

28. OH, D.-W.; KO, C.; RAMANATHAN, S.; CAHILL, D. G. Thermal conductivity and dynamic heat capacity across the metal-insulator transition in thin film VO2. *Applied Physics Letters*. 2010, **96**(15), 151906. Available from DOI: 10.1063/1.3394016.

29. BALU, R.; ASHRIT, P. V. Near-zero IR transmission in the metal-insulator transition of VO2 thin films. *Applied Physics Letters*. 2008, **92**(2), 021904. Available from DOI: 10.1063/1.2834367.

30. BARKER, A. S.; VERLEUR, H. W.; GUGGENHEIM, H. J. Infrared Optical Properties of Vanadium Dioxide Above and Below the Transition Temperature. *Phys. Rev. Lett.* 1966-12, **17**, 1286–1289. Available from DOI: 10.1103/PhysRevLett.17.1286.

31. HUANG, Z.; CHEN, S.; LV, C.; HUANG, Y., et al. Infrared characteristics of VO2 thin films for smart window and laser protection applications. *Applied Physics Letters*. 2012, **101**(19), 191905. Available from DOI: 10.1063/1.4766287.

32. CEITEC. *CEITEC Nano Research Infrastructure*. Available also from: https://nano.ceitec.cz/about-ceitec-nano/.

33. XIONG, W. M.; SHAO, J.; ZHANG, Y. Q.; CHEN, Y., et al. Morphology-controlled epitaxial vanadium dioxide low-dimensional structures: the delicate effects on the phase transition behaviors. *Phys. Chem. Chem. Phys.* 2018, **20**, 14339–14347. Available from DOI: 10.1039/C7CP08432C.

34. MARTENS, K.; AETUKURI, N.; JEONG, J.; SAMANT, M. G., et al. Improved metal-insulator-transition characteristics of ultrathin VO2 epitaxial films by optimized surface preparation of rutile TiO2 substrates. *Applied Physics Letters*. 2014, **104**(8), 081918. Available from DOI: 10.1063/1.4866037.

35. EARL, S. K.; JAMES, T. D.; DAVIS, T. J.; MCCALLUM, J. C., et al. Tunable optical antennas enabled by the phase transition in vanadium dioxide. *Opt. Express*. 2013-11, **21**(22), 27503–27508. Available from DOI: 10.1364/OE.21.027503.

36. MARVEL, R. E.; APPAVOO, K.; CHOI, B. K.; NAG, J., et al. Electron-beam deposition of vanadium dioxide thin films. *Applied Physics A*. 2013-06, **111**(3), 975–981. ISSN 1432-0630. Available from DOI: 10.1007/s00339-012-7324-5.

37. CHAIN, E. E. Effects of oxygen in ion-beam sputter deposition of vanadium oxide. *Journal of Vacuum Science & Technology A*. 1987, **5**(4), 1836–1839. Available from DOI: 10.1116/1.574510.

38. YI, X.; CHEN, C.; LIU, L.; WANG, Y., et al. A new fabrication method for vanadium dioxide thin films deposited by ion beam sputtering. *Infrared Physics Technology*. 2003, **44**(2), 137–141. ISSN 1350-4495. Available from DOI: https://doi.org/10.1016/S1350-4495(02)00187-1.

39. ZHANG, C.; KOUGHIA, C.; GÜNEŞ, O.; LUO, J., et al. Synthesis, structure and optical properties of high-quality VO2 thin films grown on silicon, quartz and sapphire substrates by high temperature magnetron sputtering: Properties through the transition temperature. *Journal of Alloys and Compounds*. 2020, **848**, 156323. ISSN 0925-8388. Available from DOI: https://doi.org/10.1016/j.jallcom.2020.156323.

40. BA, C.; BAH, S. T.; D'AUTEUIL, M.; ASHRIT, P. V., et al. Fabrication of High-Quality VO2 Thin Films by Ion-Assisted Dual ac Magnetron Sputtering. *ACS Applied Materials & Interfaces*. 2013, **5**(23), 12520–12525. Available from DOI: 10.1021/am403807u.

41. BLANQUART, T.; NIINISTÖ, J.; GAVAGNIN, M.; LONGO, V., et al. Atomic layer deposition and characterization of vanadium oxide thin films. *RSC Adv.* 2013, **3**, 1179–1185. Available from DOI: 10.1039/C2RA22820C.

42. AU - CURRIE, M.; AU - MASTRO, M. A.; AU - WHEELER, V. D. Atomic Layer Deposition of Vanadium Dioxide and a Temperature-dependent Optical Model. *JoVE*. 2018-05, (135), e57103. ISSN 1940-087X. Available from DOI: 10.3791/57103.

43. FAN, L. L.; CHEN, S.; WU, Y. F.; CHEN, F. H., et al. Growth and phase transition characteristics of pure M-phase VO2 epitaxial film prepared by oxide molecular beam epitaxy. *Applied Physics Letters*. 2013, **103**(13), 131914. Available from DOI: 10.1063/1.4823511.

44. PAIK, H.; MOYER, J. A.; SPILA, T.; TASHMAN, J. W., et al. Transport properties of ultra-thin VO2 films on (001) TiO2 grown by reactive molecular-beam epitaxy. *Applied Physics Letters*. 2015, **107**(16), 163101. Available from DOI: 10.1063/1.4932123.

45. YAKOVKINA, L. V.; MUTILIN, S. V.; PRINZ, V. Y.; SMIRNOVA, T. P., et al. MOCVD growth and characterization of vanadium dioxide films. *Journal of Materials Science*. 2017-04, **52**(7), 4061–4069. ISSN 1573-4803. Available from DOI: 10.1007/s10853-016-0669-y.

46. GUO, B.; WAN, D.; WANG, J.; ZHU, S., et al. Mo-Al co-doped VO2(B) thin films: CVD synthesis, thermal sensitive properties, synchrotron radiation photoelectron and absorption spectroscopy study. *Journal of Alloys and Compounds*. 2018, **745**, 247–255. ISSN 0925-8388. Available from DOI: https://doi.org/10.1016/j.jallcom.2018.02.195.

47. PARTLOW, D. P.; GURKOVICH, S. R.; RADFORD, K. C.; DENES, L. J. Switchable vanadium oxide films by a sol-gel process. *Journal of Applied Physics*. 1991, **70**, 443–452.

48. WU, Y. F.; FAN, L. L.; CHEN, S. M.; CHEN, S., et al. Spectroscopic analysis of phase constitution of high quality VO2 thin film prepared by facile sol-gel method. *AIP Advances*. 2013, **3**(4), 042132. Available from DOI: 10.1063/1.4802981.

49. KEPIČ, P. *Design and fabrication of tunable dielectric metasurfaces for visible and infrared wavelengths.* Brno University of Technology. Faculty of Mechanical Engineering, 2021.

50. SMITH, H. M.; TURNER, A. F. Vacuum Deposited Thin Films Using a Ruby Laser. *Appl. Opt.* 1965-01, **4**(1), 147–148. Available from DOI: 10.1364/AO.4.000147.

51. CHRISTEN, H. M.; ERES, G. Recent advances in pulsed-laser deposition of complex oxides. *Journal of Physics: Condensed Matter*. 2008-06, **20**(26), 264005. Available from DOI: 10.1088/0953-8984/20/26/264005.

52. CEITEC. *Pulsed laser deposition preparation chamber (UHV-PLD)* [online] [visited on 2022-03-19]. Available from: https://nano.ceitec.cz/ultra-high-vacuum-preparation-and-analytical-system-uhv-cluster/.

53. NAG, J.; JR, R. F. H. Synthesis of vanadium dioxide thin films and nanoparticles. *Journal of Physics: Condensed Matter*. 2008-06, **20**(26), 264016. Available from DOI: 10.1088/0953-8984/20/26/264016.

54. BOREK, M.; QIAN, F.; NAGABUSHNAM, V.; SINGH, R. K. Pulsed laser deposition of oriented VO2 thin films on R-cut sapphire substrates. *Applied Physics Letters*. 1993, **63**(24), 3288–3290. Available from DOI: 10.1063/1.110177.

55. KIM, D. H.; KWOK, H. S. Pulsed laser deposition of VO2 thin films. *Applied Physics Letters*. 1994, **65**(25), 3188–3190. Available from DOI: 10.1063/1.112476.

56. MAAZA, M.; MARITZ, J.; MCLACHLAN, D.; SWANEPOOL, R., et al. Direct production of thermochromic VO2 thin film coatings by pulsed laser ablation. *Optical Materials*. 2000-09, **15**, 41–45.

57. BHARDWAJ, D.; GOSWAMI, A.; UMARJI, A. M. Synthesis of phase pure vanadium dioxide (VO2) thin film by reactive pulsed laser deposition. *Journal of Applied Physics*. 2018, **124**(13), 135301. Available from DOI: 10.1063/1.5046455.

58. NARAYAN, J.; BHOSLE, V. M. Phase transition and critical issues in structure-property correlations of vanadium oxide. *Journal of Applied Physics*. 2006, **100**(10), 103524. Available from DOI: 10.1063/1.2384798.

59. NAG, J.; PAYZANT, E. A.; MORE, K. L.; HAGLUND, R. F. Enhanced performance of room-temperature-grown epitaxial thin films of vanadium dioxide. *Applied Physics Letters*. 2011, **98**(25), 251916. Available from DOI: 10.1063/1.3600333.

60. LIN, T.; ZHANG, Y.; ZHENG, D. The ultrathin VO2(M) film with ultrahigh visible transmittance synthesized on the quartz glass substrate by HiPIMS. *Vacuum*. 2018, **156**, 449–455. ISSN 0042-207X. Available from DOI: https://doi.org/10.1016/j.vacuum.2018.08.008.

61. MARTENS, K.; AETUKURI, N.; JEONG, J.; SAMANT, M. G., et al. Improved metal-insulator-transition characteristics of ultrathin VO2 epitaxial films by optimized surface preparation of rutile TiO2 substrates. *Applied Physics Letters*. 2014, **104**(8), 081918. Available from DOI: 10.1063/1.4866037.

62. NORTON, D. P. Pulsed Laser Deposition of Complex Materials: Progress Toward Applications. In: *Pulsed Laser Deposition of Thin Films*. John Wiley Sons, Ltd, 2006, chap. 1, pp. 1–31. ISBN 9780470052129. Available from DOI: https://doi.org/10.1002/9780470052129.ch1.

63. ASHFOLD, M.; CLAEYSSENS, F.; FUGE, G.; HENLEY, S. Pulser Laser Ablation and Deposition of Thin Films. *Chemical Society Reviews*. 2004-02, **33**, 23–31. Available from DOI: 10.1039/b207644f.

64. NOLL, R. Laser-Induced Breakdown Spectroscopy. In: *Laser-Induced Breakdown Spectroscopy: Fundamentals and Applications*. Berlin, Heidelberg: Springer Berlin Heidelberg, 2012, pp. 7–15. ISBN 978-3-642-20668-9. Available from DOI: 10.1007/978-3-642-20668-9_2.

65. KREBS, H.-U.; WEISHEIT, M.; FAUPEL, J.; SÜSKE, E., et al. Pulsed Laser Deposition (PLD) – A Versatile Thin Film Technique. In: *Advances in Solid State Physics*. Ed. by KRAMER, B. Berlin, Heidelberg: Springer Berlin Heidelberg, 2003, pp. 505–518.

66. SREE HARSHA, K. Principles of Vapor Deposition of Thin Films. In: Oxford: Elsevier, 2006, pp. 11–143. ISBN 978-0-08-044699-8. Available from DOI: https://doi.org/10.1016/B978-008044699-8/50002-4.

67. CAMPBELL, S. *Fabrication Engineering at the Micro- and Nanoscale*. Oxford University Press, 2013. Oxford series in electrical and computer engineering. ISBN 9780199861224.

68. REARDON, A. C. *Metallurgy for the Non-Metallurgist*. ASM International, 2011-10. ISBN 978-1-62708-261-7. Available from DOI: 10.31399/asm.tb.mnm2.9781627082617.

69. SNEAD, L. L.; HOELZER, D. T.; RIETH, M.; NEMITH, A. A. Structural Alloys for Nuclear Energy Applications. In: Boston: Elsevier, 2019. ISBN 978-0-12-397046-6. Available from DOI: https://doi.org/10.1016/B978-0-12-397046-6.00013-7.

70. LIŠKA, J.; LIGMAJER, F.; PINHO N., P. V.; KEJÍK, L., et al. Effect of deposition angle on fabrication of plasmonic gold nanocones and nanodiscs. *Microelectronic Engineering*. 2020, **228**, 111326. ISSN 0167-9317. Available from DOI: https://doi.org/10.1016/j.mee.2020.111326.

71. CEITEC. *Electron beam evaporator BESTEC* [online] [visited on 2022-03-19]. Available from: https://nano.ceitec.cz/electron-beam-evaporator-bestec-evaporator/.

72. ZHANG, J. X.; HOSHINO, K. Molecular Sensors and Nanodevices. In: Second Edition. Academic Press, 2019. ISBN 978-0-12-814862-4. Available from DOI: https://doi.org/10.1016/B978-0-12-814862-4.00002-8.

73. MATTOX, D. M. Handbook of Physical Vapor Deposition (PVD) Processing. In: Second Edition. Boston: William Andrew Publishing, 2010. ISBN 978-0-8155-2037-5. Available from DOI: https://doi.org/10.1016/B978-0-8155-2037-5.00001-0.

74. ROSSNAGEL, S. M. Thin film deposition with physical vapor deposition and related technologies. *Journal of Vacuum Science & Technology A*. 2003, **21**(5), S74–S87. Available from DOI: 10.1116/1.1600450.

75. SURYANARAYANAN, R. The co-evaporation technique—A potential tool for basic and applied research. *Thin Solid Films*. 1978, **50**, 349–355. ISSN 0040-6090. Available from DOI: https://doi.org/10.1016/0040-6090(78)90120-7.

76. BASHIR, A.; AWAN, T. I.; TEHSEEN, A.; TAHIR, M. B., et al. Chemistry of Nanomaterials. In: Elsevier, 2020. ISBN 978-0-12-818908-5. Available from DOI: https://doi.org/10.1016/B978-0-12-818908-5.00003-2.

77. WASA, K.; KANNO, I.; KOTERA, H. (eds.). Handbook of Sputtering Technology. In: Second Edition. Oxford: William Andrew Publishing, 2012. ISBN 978-1-4377-3483-6. Available from DOI: https://doi.org/10.1016/B978-1-4377-3483-6.00018-8.

78. PAVERA, M. *Automation and control of multilayers deposition by IBS/IBAD*. Brno University of Technology. Faculty of Mechanical Engineering, 2011.

79. CHAIN, E. E. Effects of oxygen in ion-beam sputter deposition of vanadium oxide. *Journal of Vacuum Science & Technology A*. 1987, **5**(4), 1836–1839. Available from DOI: 10.1116/1.574510.

80. INSTITUTE OF PHYSICAL ENGINEERING. *Kaufman* [online]. 2011 [visited on 2022-03-19]. Available from: http://physics.fme.vutbr.cz/ufi.php?Action=0&Id=1425.

81. KAUFMAN, H. R.; CUOMO, J. J.; HARPER, J. M. E. Technology and applications of broad-beam ion sources used in sputtering. Part I. Ion source technology. *Journal of Vacuum Science and Technology*. 1982, **21**(3), 725–736. Available from DOI: 10.1116/1.571819.

82. HIRVONEN, J. K. Ion Beam Assisted Thin Film Deposition: in: *Materials and Processes for Surface and Interface Engineering*. Ed. by PAULEAU, Y. Dordrecht: Springer Netherlands, 1995, pp. 307–346. ISBN 978-94-011-0077-9. Available from DOI: 10.1007/978-94-011-0077-9_9.

83. SMIDT, F. A. Use of ion beam assisted deposition to modify the microstructure and properties of thin films. *International Materials Reviews*. 1990, **35**(1), 61–128. Available from DOI: 10.1179/095066090790323975.

84. BUNDESMANN, C.; NEUMANN, H. Tutorial: The systematics of ion beam sputtering for deposition of thin films with tailored properties. *Journal of Applied Physics*. 2018, **124**(23), 231102. Available from DOI: 10.1063/1.5054046.

85. ANDERS, A. Physics of arcing, and implications to sputter deposition. *Thin Solid Films*. 2006, **502**(1), 22–28. ISSN 0040-6090. Available from DOI: https://doi.org/10.1016/j.tsf.2005.07.228. Selected Papers from the 5th International Conference on Coatings on Glass (ICCG5)- Advanced Coatings on Glass and Plastics for Large-Area or High-Volume Products.

86. SIGMUND, P. Sputtering of single and multiple component materials. *Journal of Vacuum Science and Technology*. 1980, **17**(1), 396–399. Available from DOI: 10.1116/1.570399.

87. MELNGAILIS, J. Focused ion beam technology and applications. *Journal of Vacuum Science & Technology B: Microelectronics Processing and Phenomena*. 1987, **5**(2), 469–495. Available from DOI: 10.1116/1.583937.

88. ORLOFF, J. High-resolution focused ion beams. *Review of Scientific Instruments*. 1993, **64**(5), 1105–1130. Available from DOI: 10.1063/1.1144104.

89. GIANNUZZI, L.; STEVIE, F. *Introduction to focused ion beams: instrumentation, theory, techniques and practice*. Springer Science & Business Media, 2004. Available from DOI: https://doi.org/10.1007/b101190.

90. KIM, C.-S.; AHN, S.-H.; JANG, D.-Y. Review: Developments in micro/nanoscale fabrication by focused ion beams. *Vacuum*. 2012, **86**(8), 1014–1035. ISSN 0042-207X. Available from DOI: https://doi.org/10.1016/j.vacuum.2011.11.004.

91. JUBLOT, M.; TEXIER, M. Sample preparation by focused ion beam micromachining for transmission electron microscopy imaging in front-view. *Micron*. 2014, **56**, 63–67. ISSN 0968-4328. Available from DOI: https://doi.org/10.1016/j.micron.2013.10.007.

92. LECHNER, L.; BISKUPEK, J.; KAISER, U. Improved Focused Ion Beam Target Preparation of (S)TEM Specimen—A Method for Obtaining Ultrathin Lamellae. *Microscopy and Microanalysis*. 2012, **18**(2), 379–384. Available from DOI: 10.1017/S1431927611012499.

93. CEITEC. *Focused Ion Beam/Scanning Electron Microscope TESCAN LYRA3 (LYRA)* [online] [visited on 2022-03-19]. Available from: https://nano.ceitec.cz/focused-ion-beam-scanning-electron-microscope-tescan-lyra3-lyra/.

94. CHEN, Y. Nanofabrication by electron beam lithography and its applications: A review. *Microelectronic Engineering*. 2015, **135**, 57–72. ISSN 0167-9317. Available from DOI: https://doi.org/10.1016/j.mee.2015.02.042.

95. HU, W.; SARVESWARAN, K.; LIEBERMAN, M.; BERNSTEIN, G. H. Sub-10 nm electron beam lithography using cold development of poly(methylmethacrylate). *Journal of Vacuum Science & Technology B: Microelectronics and Nanometer Structures Processing, Measurement, and Phenomena*. 2004, **22**(4), 1711–1716. Available from DOI: 10.1116/1.1763897.

96. KRPENSKÝ, J. *Interaction between SNOM tip and near-field*. Brno University of Technology. Faculty of Mechanical Engineering, 2020.

97. MAYER, J.; GIANNUZZI, L. A.; KAMINO, T.; MICHAEL, J. TEM Sample Preparation and FIB-Induced Damage. *MRS Bulletin*. 2007-05, **32**(5), 400–407. ISSN 1938-1425. Available from DOI: 10.1557/mrs2007.63.

98. GIANNUZZI, L. A.; GEURTS, R.; RINGNALDA, J. 2 keV Ga FIB Milling for Reducing Amorphous Damage in Silicon. *Microscopy and Microanalysis*. 2005, **11**(S02), 828–829. Available from DOI: 10.1017/S1431927605507797.

99. DICTIONARY.COM LLC. *Lamella definition & meaning*. Available also from: https://www.dictionary.com/browse/lamella.

100. AGAR SCIENTIFIC LTD. *Standard probe tips AGJ411*. Available also from: https://www.agarscientific.com/standard-probe-tips.

101. AGAR SCIENTIFIC LTD. *Omniprobe – 4 post lift-out grids*. Available also from: https://www.agarscientific.com/tem/grids-omniprobe/4-post-lift-out-grids.

102. MATECK GMBH. *Vanadium(IV) oxide powder*. Available also from: https://mateck.com/vanadium-iv-oxide-powder-4269.html.

103. AGAR SCIENTIFIC LTD. *Holey carbon films – Copper*. Available also from: https://www.agarscientific.com/holey-carbon-films.

104. CEITEC. *High resolution Scanning Electron Microscope FEI Verios 460L (VERIOS)* [online] [visited on 2022-04-15]. Available from: https://nano.ceitec.cz/high-resolution-scanning-electron-microscope-fei-verios-460l-verios/.

105. GILL, F. B.; PRUM, R. O.; ROBINSON, S. K. *Ornithology*. 4th ed. 2019.

106. PROTOCHIPS EMEA GMBH. *Fusion Select*. Available also from: https://www.protochips.com/products/fusion/.

107. CEITEC. *High Resolution (Scanning) Transmission Electron Microscope FEI Titan Themis 60-300 cubed (TITAN)* [online] [visited on 2022-03-19]. Available from: https://nano.ceitec.cz/high-resolution-scanning-transmission-electron-microscope-fei-titan-themis-60-300-cubed-titan/.

108. WILLIAMS, D. B.; CARTER, C. B. *Transmission Electron Microscopy*. Springer, 2009. ISBN 9780387765006.

109. HORÁK, M. *Electron microscopy and spectroscopy in plasmonics*. Brno University of Technology. CEITEC BUT, 2020.

110. EGERTON, R. F. *Electron energy-loss spectroscopy in the electron microscope*. Springer Science & Business Media, 2011.

111. LAZAR, S.; BOTTON, G.; ZANDBERGEN, H. Enhancement of resolution in core-loss and low-loss spectroscopy in a monochromated microscope. *Ultramicroscopy*. 2006, **106**(11), 1091–1103. ISSN 0304-3991. Available from DOI: https://doi.org/10.1016/j.ultramic.2006.04.024. Proceedings of the International Workshop on Enhanced Data Generated by Electrons.

112. HILLIER, J.; BAKER, R. F. Microanalysis by Means of Electrons. *Journal of Applied Physics*. 1944, **15**(9), 663–675. Available from DOI: 10.1063/1.1707491.

113. KHURSHEED, A.; KARUPPIAH, N.; OSTERBERG, M.; THONG, J. T. L. Add-on transmission attachments for the scanning electron microscope. *Review of Scientific Instruments*. 2003, **74**(1), 134–140. Available from DOI: 10.1063/1.1529301.

114. BRODUSCH, N.; DEMERS, H.; GELLÉ, A.; MOORES, A., et al. Electron energy-loss spectroscopy (EELS) with a cold-field emission scanning electron microscope at low accelerating voltage in transmission mode. *Ultramicroscopy*. 2019, **203**, 21–36. ISSN 0304-3991. Available from DOI: https://doi.org/10.1016/j.ultramic.2018.12.015.

115. GARCIA DE ABAJO, F. J. Optical excitations in electron microscopy. *Rev. Mod. Phys.* 2010-02, **82**, 209–275. Available from DOI: 10.1103/RevModPhys.82.209.

116. ČERENKOV, P. A. Visible Radiation Produced by Electrons Moving in a Medium with Velocities Exceeding that of Light. *Phys. Rev.* 1937-08, **52**, 378–379. Available from DOI: 10.1103/PhysRev.52.378.

117. KABÁT, J. *Modelling electron energy-loss spectra of vanadium dioxide nanostructures*. Brno University of Technology. Faculty of Mechanical Engineering, 2022.

118. HÉBERT, C.; WILLINGER, M.; SU, D. S.; PONGRATZ, P., et al. Oxygen K-edge in vanadium oxides: simulations and experiments. *The European Physical Journal B - Condensed Matter and Complex Systems*. 2002-08, **28**(4), 407–414. ISSN 1434-6036. Available from DOI: 10.1140/epjb/e2002-00244-4.

119. LI, X.; GLOTER, A.; GU, H.; LUO, J., et al. Discovery of nanoscale reduced surfaces and interfaces in VO2 thin films as a unique case of prewetting. *Scripta Materialia*. 2014, **78-79**, 41–44. ISSN 1359-6462. Available from DOI: https://doi.org/10.1016/j.scriptamat.2014.01.029.

120. UTKE, I.; HOFFMANN, P.; MELNGAILIS, J. Gas-assisted focused electron beam and ion beam processing and fabrication. *Journal of Vacuum Science & Technology B: Microelectronics and Nanometer Structures Processing, Measurement, and Phenomena*. 2008, **26**(4), 1197–1276. Available from DOI: 10.1116/1.2955728.

121. TAO, T.; RO, J.; MELNGAILIS, J.; XUE, Z., et al. Focused ion beam induced deposition of platinum. *Journal of Vacuum Science & Technology B: Microelectronics Processing and Phenomena*. 1990, **8**(6), 1826–1829. Available from DOI: 10.1116/1.585167.

122. PURETZ, J.; SWANSON, L. W. Focused ion beam deposition of Pt containing films. *Journal of Vacuum Science & Technology B: Microelectronics and Nanometer Structures Processing, Measurement, and Phenomena*. 1992, **10**(6), 2695–2698. Available from DOI: 10.1116/1.586028.

123. ŠAMOŘIL, T. *Application of the focused ion and electron beam in nanotechnologies*. Brno University of Technology. Faculty of Mechanical Engineering, 2015.

124. GLOTER, A.; SERIN, V.; TURQUAT, C.; CESARI, C., et al. Vanadium valency and hybridization in V-doped hafnia investigated by electron energy loss spectroscopy. *The European Physical Journal B - Condensed Matter and Complex Systems*. 2001-07, **22**(2), 179–186. ISSN 1434-6036. Available from DOI: 10.1007/PL00011142.

125. KIM, Y.; SONG, G. Y.; NANDI, R.; CHO, J. Y., et al. Phase identification of vanadium oxide thin films prepared by atomic layer deposition using X-ray absorption spectroscopy. *RSC Adv.* 2020, **10**, 26588–26593. Available from DOI: 10.1039/D0RA04384B.

126. KUMAR, S.; STRACHAN, J. P.; KILCOYNE, A. L. D.; TYLISZCZAK, T., et al. The phase transition in VO2 probed using x-ray, visible and infrared radiations. *Applied Physics Letters*. 2016, **108**(7), 073102. Available from DOI: 10.1063/1.4939746.

127. RUZMETOV, D.; SENANAYAKE, S. D.; RAMANATHAN, S. X-ray absorption spectroscopy of vanadium dioxide thin films across the phase-transition boundary. *Phys. Rev. B*. 2007-05, **75**, 195102. Available from DOI: 10.1103/PhysRevB.75.195102.

List of abbreviations

ADF	Annular dark field
EBL	Electron beam lithography
EDX	Energy-dispersive X-ray spectroscopy
EEL	Electron energy-loss
EELS	Electron energy-loss spectroscopy
FEBID	Focused electron beam induced deposition
FIB	Focused ion beam
FIBID	Focused ion beam induced deposition
GIS	Gas injection system
HAADF	High-angle annular dark field
HV	High vacuum
IBAD	Ion beam assisted deposition
IBSD	Ion beam sputter deposition
IR	Infrared
LMIS	Liquid metal ion source
MIT	Metal–insulator transition
PLD	Pulsed laser deposition
PVD	Physical vapour deposition
SEM	Scanning electron microscopy
STEM	Scanning transmission electron microscope/microscopy
TEM	Transmission electron microscope/microscopy
UHV	Ultra high vacuum
VO_2	Vanadium dioxide
WD	Working distance
ZLP	Zero-loss peak